UNIVERSITY OF CALIFORNIA,
IRVINE

Understanding the Structure and Stability of Post-Translationally Modified γS-Crystallin

DISSERTATION

submitted in partial satisfaction of the requirements
for the degree of

DOCTOR OF PHILOSOPHY

in Chemistry

by

Megan Rocha

Dissertation Committee:
Professor Rachel W. Martin, Chair
Professor Gregory A. Weiss
Assistant Professor Joseph P. Patterson

2024

DEDICATION

To my husband.

TABLE OF CONTENTS

LIST OF FIGURES

LIST OF TABLES

ACKNOWLEDGMENTS

I would like to thank Professor Rachel Martin, for supporting me and everyone of her students with respect. Your leadership style should be admired by all. It inspires the best out of your students.

I would also like to thank Dr. Dmitry Fishman, for his poetic love of science. You inspired me to truly understand the depths of my research. I remain in awe of spectroscopy.

Thank you to every member of the Martin lab, especially:

All of my undergrads - for your support and patience. Brenna - who was the greatest mentor, collaborator, and friend. Collin, Matthew, and Jae - for providing support, friendship, and endless laughs.

Thank you to the Gilmore Girls. Where I lead, you followed me. Any- anywhere, that I told you to. When I needed you to be with me, you followed me where I led.

Thank you to all of my atomic friends. I never a imagined I would have a life filled with so many lovely colors of friendship. From DND to karaoke - I live in technicolor laughs and songs. To Makena, Claire, Mackenzie and Sharon for standing next to me on all my biggest and smallest days. My giant love for you all is not captured in such small words.

Thank you to all of my family. It is the pride of my family that is the foundation of my strength. I love you mom.

Thank you to Julia for the purrs and cuddles. You are so cute I could cry.

Thank you to my husband, Robert Dorn. I am in awe for all you are.

Chapter 1 adapted with permission from: Megan A. Rocha, Marc A. Sprague-Piercy, Ashley O. Kwok, Kyle W. Roskamp, and Rachel W. Martin* "Chemical properties determine solubility and stability in $\beta\gamma$-crystallins of the eye lens" *ChemBioChem*, **2021**, 22, 1329-1346

Chapter 2 adapted with permission from: Brenna Norton-Baker†, Megan A. Rocha†, (†contributed equally) Jessica Granger-Jones, Dmitry Fishman, and Rachel W. Martin* "Human γS- crystallin resists unfolding despite extensive chemical modification from exposure to ionizing radiation" *J. Phys. Chem. B* **2022**, 126, 679–690.

This research was supported by NIH F31 5F31EY034393 and by NIH grants EY021514, 2R01EY021514.

VITA

Megan Rocha

EDUCATION

Doctor of Philosophy in Chemistry **2024**
University of California, Irvine *Irvine, CA*

Bachelor of Arts in Chemistry **2017**
Whitman College *Walla Walla, WA*

RESEARCH EXPERIENCE

Graduate Research Assistant **2019–2024**
University of California, Irvine *Irvine, CA*

Undergraduate Research Assistant **2015–2017**
Whitman College *Walla Walla, WA*

TEACHING EXPERIENCE

Teaching Assistant **2020–2019**
University of California, Irvine *Irvine, CA*

REFEREED JOURNAL PUBLICATIONS

1. *Macrocyclic oxindole peptide epoxyketones – a comparative study of macrocyclic inhibitors of the 20S proteasome.* Gotz, M.G., Godwin K., Price, R., Dorn, R., Merril-Steskal, G., Klemmer, W., Hansen, H., Produturi, G., **Rocha, M.**, Palmer, M., Molacek, L., Strater, Z., Groll, M. *ACS Medicine Chemistry Letters*, **2024**, 15(4), 533-539

2. *Biomimetic sequence-templating approach towards a multiscale modulation of chromogenic polymer properties.* Kuang, Y., Yao, Z., Lim, S., Ngo, C., **Rocha, M.A.**, Fishman, D. A., Ardona, H. M. *Macromolecules*, **2023**, 56(12), 4526-4540

3. *Deamidation of the human eye lens protein γS-crystallin accelerates oxidative aging.* Norton- Baker, B., Mehrabi, P., Kwok, A. O., Roskamp, K. W., **Rocha, M. A.**, Sprauge-Piercy, M., Stetten, D. V., Miller, R. J. D., Martin, R. W. *Structure*, **2022**, 30(5), 763-776

4. *Human γS-crystallin resists unfolding despite extensive chemical modification from exposure to ionizing radiation.* Norton-Baker, B.*, **Rocha M. A.***, Granger-Jones, J., Fishman, D., Martin R.W. *Journal of Physical Chemistry B.*, **2022**, 126(3), 679-690

5. *Chemical properties determine solubility and stability in $\beta\gamma$-crystallins of the eye lens.* **Rocha, M. A.**, Sprague-Piercy, M. A., Kwok, A. O., Roskamp, K.W., Martin, R. W. *ChemBioChem*, **2021**, 22(8), 1329-1346

6. *α-Crystallins in the vertebrate eye lens: Complex oligomers and molecular chaperones.* Sprague- Piercy M. A., **Rocha, M. A.**, Kwok, A. O., Martin R. W. *Annual Review of Physical Chemistry*, **2021**, 20(72), 143-163

REFEREED CONFERENCE PUBLICATIONS

1. "Cataract variants of human γS-crystallin" Experimental Nuclear Magnetic Resonance Conference (ENC), (Pacific Grove, Ca), Poster, April 2024

2. "Probing the dynamics of cataract-related human γS-crystallin deamidation variants" Experimental Nuclear Magnetic Resonance Conference (ENC), (Pacific Grove, Ca), Poster, April 2023

3. "Altered dynamics of human γS crystallin from deamidation" International Conference of the Lens, (Kona, HI), Invited oral presentation, December 2022

4. "Acute effects of ionizing radiation on human γS-crystallin" International Crystallin Biophysics Workshop (BPS), (Virtual), Oral Presentation, February 2022

5. "Acute effects of ionizing radiation on human γS-crystallin" Biophysical Society (BPS), (San Francisco, CA), Poster, February 2022

6. "Design and synthesis of a macrocyclic, non-covalent proteasome inhibitor" American Chemical Society (ACS), (Philidelphia, PA), Poster, August 2016

ABSTRACT OF THE DISSERTATION

Understanding the Structure and Stability of Post-Translationally Modified γS-Crystallin

By

Megan Rocha

Doctor of Philosophy in Chemistry

University of California, Irvine, 2024

Professor Rachel W. Martin, Chair

The human lens β- and γ-crystallins, are fantastically stable, soluble, and refractive. These properties allow them to form a transparent tissue specially designed to focus light. Over time, they accumulate post-translational modifications (PTMs) from damaging species, such as metal ions and ionizing radiation. These PTMs alter the biophysical properties of the lens proteins until their solubility fails and light-scattering aggregates form. These large particles form age-related cataract - the leading cause of blindness worldwide. Here, I show my investigation into the boundaries of human γS-crystallin (HγS) solubility after the accumulation of PTMs. I show that exposure to high doses of γ irradiation causes extensive oxidation, but HγS largely resists unfolding. Additionally, four HγS variants that mimic progressive deamidation and are prone to oxidation show no changes in the slow dynamics. However, the increased surface charge leads to unfavorable electrostatics. The work described in this thesis will help unravel the structural determinants of cataract.

Chapter 1

Introduction

The focusing power of the vertebrate eye is determined in part by the concentration and distribution of the extremely long-lived crystallin proteins making up the lens. In terrestrial organisms, the air/water interface at the cornea also plays a major role (1), whereas in fish, this functionality is entirely determined by the shape and composition of the lens.(2; 3; 4) Crystallins have evolved from diverse small, soluble proteins (5; 6) and comprise the majority of the lens tissue.(7; 8) The majority of crystallins in the vertebrate lens belong to two superfamilies, the chaperone α-crystallins and the structural and refractive $\beta\gamma$-crystallins. Unlike most proteins, which are subject to continuous turnover in the cell, crystallins are generally not replaced after their expression during early development. Crystallin aggregation leads to cataract, a leading cause of blindness and a WHO priority eye disease.(9) In addition to their biomedical relevance, the long-term solubility and stability of crystallin proteins also represent a fascinating physical chemistry problem. How do these small, globular proteins maintain their solubility and transparency for prolonged periods, even at concentrations upwards of 400 mg/mL? In terms of understanding the underlying phenomena, crystallin longevity is thus the flip side of protein deposition diseases. Understanding the factors that enable these proteins to resist aggregation in the crowded lens environment for many years

is critical to forming a complete picture of protein solubility and aggregation.

In this review, we summarize the major types of structural crystallins found in vertebrate lenses, their evolutionary origins, and important structural features. We also consider the many routes to cataract formation from a physical chemistry perspective. We describe some of the experimental techniques that are most commonly used for studies of crystallins. Hereditary cataract can be caused by mutations to any of the major crystallin proteins that change their folding stability or surface properties. Other mutations can create conditions under which crystallin solubility is compromised. Reduced crystallin solubility can also result from post-translational modifications (PTMs), which can take the form of deamidation, oxidation, interactions with metal cations, proteolysis, or derivatization with sugars. UV light irradiation, a common factor in age-related cataract, is one pathway to several types of crystallin damage. We discuss the role of protein-protein interactions in mediating aggregation. Finally, we describe how liquid-liquid phase separation (LLPS) can occur in lens proteins, even under conditions where they are fully folded.

1.1 $\beta\gamma$-crystallins evolved from a common origin and fulfill structural and refractive functions

$\beta\gamma$-crystallins are the primary structural and optical proteins of the lens; they maintain transparency, increase the refractive index, and protect the retina from UV light damage. In the lens fiber cells, these proteins exist as an amorphous, dense liquid where transparency is governed by the short-range spatial order, similar to a glass.(10) The key regulators of $\beta\gamma$-crystallin expression are the transcription factors c-MAF and Pax6.(11) Pax6 gene regulation is conserved amongst all crystallins, including vertebrate α-crystallins as well as unrelated taxon-specific crystallins (e.g., jellyfish J2- and J3-crystallins and scallop Ω-crystallins).

Recent evidence suggests that Pax6 regulation of these proteins may have arisen from pre-existing *cis*-sites that are affiliated with small heat shock proteins.(12)

The sequence and structural similarity of lens β and γ crystallins indicated that the two shared a common ancestor.(13; 14) The $\beta\gamma$-crystallins share a common fold characterized by two double Greek key motifs (Figure 1.1) and a per-monomer molecular mass of approximately 21 kDa. The overall symmetry of the $\beta\gamma$-crystallins suggests that the crystallins were formed from two gene duplication events, probably after their recruitment to serve a refractive function.(15) The first duplication event transitioned the single Greek key motif into a wedge-like domain containing two Greek keys, and the second event formed the dimer.(16; 8) The sequence similarity between motifs one and three and motifs two and four (Figure 1.1), but not in any other combination, are further evidence supporting these duplication events.

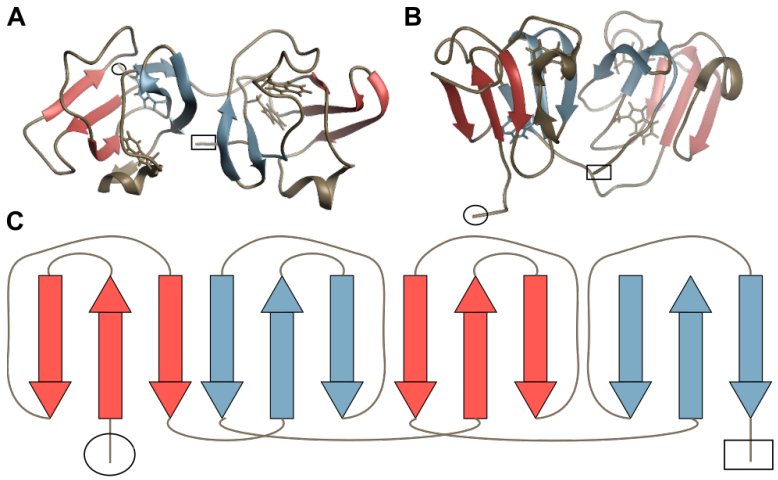

Figure 1.1: Visualization of conserved Greek-key in $\beta\gamma$-crystallins. HγS displayed to highlight the conserved structure among γ-crystallins. Protein structures are rendered using UCSF Chimera.(17) The N-terminus is circled and the C-terminus is boxed. Greek-key motifs are numbered from the N-terminus to the C-terminus. Conserved tryptophan side-chains are shown as sticks. (A) HγS (PDB ID: 2M3T) with individual Greek key motifs highlighted in red and blue. The left and right side are two wedge-like β-sandwich domains, where one Greek key (red) binds to the other (blue). From one Greek key (red), the chain passes over the protein to connect to the other Greek key motif (blue). The hydrophobic interdomain interface holds the two blue Greek key motifs together. (B) HγS rotated 90°. (C) Schematic of the Greek key motif. Each Greek key is formed by antiperiplanar β- sheets, which are continuously connected via linker sequences.

In γ-crystallins, each domain is encoded by a single exon, whereas in β-crystallins each domain is encoded by two exons separated by an intron. These alternative splicing patterns present the question of when the divergence of the β- and γ-crystallin families occurred: were γ-crystallins formed from the β-type gene encoding pattern through intron loss, or were β- and γ-crystallins formed from distinct duplication events? The presence of the βB2-crystallin outside of the lens is evidence for the former evolutionary progression.(18) The later evolutionary progression is supported by the existence of a two-domain crystallin-like protein from the sponge *Geodia* that lacks introns.(19) The relative likelihoods of these evolutionary progressions are considered in a review by Alessio (19), who concludes that the progression from the single Greek key motif to two-domain proteins were separate events for the β- and γ-crystallins. In this hypothesis, the initial fusion event formed dimers both with and without introns between the motif sequences. The dimers with introns then further combined to create the β-crystallins, whereas the latter formed γ-crystallins.

The structures of several $\beta\gamma$-crystallins are well characterized, providing a basis for comparison among paralogs (related proteins in the same organism) and orthologs (homologous proteins in different organisms). The structural building block of all of the $\beta\gamma$-crystallins can be seen in a relative of the vertebrate crystallins, the tunicate $\beta\gamma$-crystallin (PDB ID: 2BV2) (Figure 1.2A).(20) The structure of tunicate $\beta\gamma$-crystallin consists of a single domain with the familiar double Greek key motif (Figure 1.1). Along the path to modern vertebrate $\beta\gamma$-crystallins, a second double Greek key domain was added (Figure 1.2B), and the ability to bind divalent cations was lost, possibly as a result of selection for increased refractive index.(21) The single domain $\beta\gamma$-crystallin of the tunicate *Ciona intestinalis* is expressed in the light- and depth-sensing organs, but also in the palps.(20) This protein binds Ca^{2+} (20) and is greatly stabilized by doing so.(22) It also has a higher refractive index than would be predicted by amino acid sequence alone (23), giving it a unique position as a single-domain intermediate form with both Ca^{2+} binding and refractive function. Like the tunicate crystallin, other crystallins from phylum Chordata (24) and the more distantly related microbial

orthologs (25; 26; 27) have provided a wealth of background information about the evolution of $\beta\gamma$-crystallins.

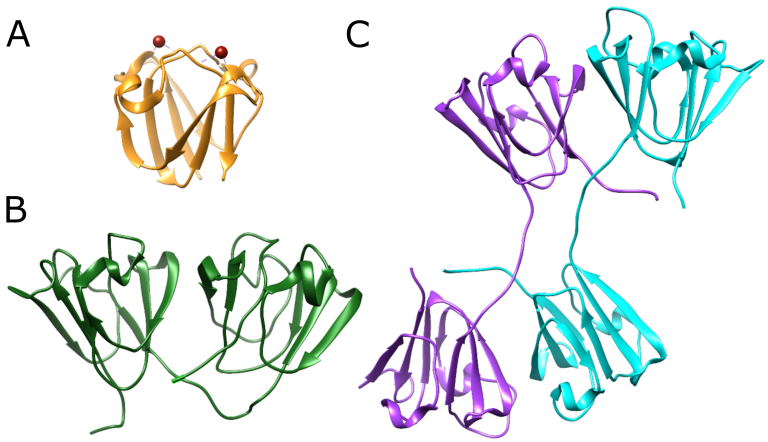

Figure 1.2: (A) Types of $\beta\gamma$-crystallins. Tunicate $\beta\gamma$-crystallin (PDB ID: 2BV2) (20) is monomeric and has a single domain. This protein can bind two calcium ions (shown in red). (B) HγS (PDB ID:2M3T) (28) in monomeric but has two double Greek key domains. (C) β-crystallins have the same domain organization, but are typically dimeric. Human βB2-crystallin can form domain-swapped dimers (PDB ID: 1YTQ).(29)

Characterization of $\beta\gamma$-crystallins' biophysical properties provides insight into the adaptation of the double-Greek key motif to its function in the eye lens. The advent of polydispersity in the eye lens from both a diverse set of $\beta\gamma$-crystallins and oligomeric domain-swapped β-crystallins appears to have increased the overall protein content that can be accommodated in the lens.(6) The linker sequence, the N- and C-terminal extensions, and the hydrophobic residues at interfaces between Greek key motifs, are all key structural features that promote domain association in $\beta\gamma$-crystallins. The extensive and sometimes contradictory data revealing the extent to which these structural features drive domain association in $\beta\gamma$-crystallins were reviewed and were used to generate a likely sequence for the evolutionary progression.(19; 8) Experiments with chimeric protein sequences show that the exchange of a β-type linker sequence or extensions for γ-type features in a β-crystallin can promote stabilization of a typically dimeric protein as a monomer. This suggests that amino acid substitutions in the interdomain linker sequence could be the key to divergence of β- and γ-crystallins. Similarly, hydrophobic residues at the β-crystallin interdomain interfaces tend

to promote dimerization more than in γ-crystallins, suggesting that substitutions in this region were critical for the divergence of β- and γ-crystallins.

1.2 The $\beta\gamma$-crystallins share a very stable fold

The structures of wild-type human γ-crystallins have been solved, as have many cataract-related variants and structural crystallins from other vertebrates, including mouse (30), chicken (31), and zebrafish.(32) NMR structures of HγB (33), HγC (PDB ID: 2NBR) (34), HγS (PDB ID: 2M3T) (28), and γD (PDB ID: 2KLJ) (35) have been reported, as well as a crystal structure of HγD (PDB ID: 1HK0).(36) β-crystallins are typically dimeric, sometimes with multiple possible configurations. For example, human βB2-crystallin has been observed in different states in solution, including a domain-swapped dimer in a crystal structure (PDB ID: 1YTQ) (29) (Figure 1.2C) and a face-en-face dimer, without domain swapping.(37) Studies of these molecules have mostly focused on two aspects: the molecular basis of their extraordinary stability and solubility, and how changes due to mutation or post-translational modification alter their biophysical properties. The γ-crystallins have shown to be more stable than β-crystallins in solution, suggesting that the inherent stability of the Greek key motif is not the only contributor to the extraordinary stability of these proteins; the interdomain interface also contributes to the overall stabilization.(38; 39) In general, the N-terminal domain is less stable than the C-terminal domain. The C-terminal domain is more conserved across the human lens paralogs, suggesting that it was strongly selected for via evolution, as it was necessary for stabilization. The N-terminal domain may therefore be more modular and able to adapt to new functions. There are several aromatic residues that increase stabilization through pi-stacking, notably in conserved tyrosine corners (40), and conserved tryptophans in the hydrophobic core, which will be discussed in Section 4.(41) A thorough account of these and other known factors that contribute to the stability of

$\beta\gamma$-crystallins were reviewed by Serebryany and King.(42)

HγS and HγD have different solubility thresholds, and different variants of these proteins exhibit a wide range of aggregation propensities.(43) The recent NMR structure of wild-type HγC shows that this protein is a typical well-folded, highly soluble γ-crystallin.(34) An NMR structure of zebrafish γM-crystallin (*Danio rerio*) (PDB ID: 2M3C) reveals different organization of hydrophobic packing in the N-terminal domain relative to human γ-crystallins, probably due to the absence of one of the generally strongly conserved Trp residues in the hydrophobic core.(32) Further experiments using solution NMR and femtosecond fluorescence spectroscopy of strategically placed Trp probes have shown that water molecules in the hydration shell of this protein exhibit slow dynamics (44), in contrast to the fast surface water dynamics shown for HγS.(45) This discrepancy may reflect the different environments occupied by these proteins, as the protein concentration in the fish lens exceeds 1000 mg/mL, more than double the concentration for the already crowded human lens.

1.3 Biophysical techniques for studying crystallins

Three-dimensional structures have been solved for many $\beta\gamma$-crystallin proteins using both X-ray crystallography and solution-state NMR, showing the similarities conferred by their characteristic fold as well as important differences in the details. X-ray crystallography is the traditional method of choice for solving biomolecular structures, as excellent tools are available for rapid data collection and structure determination once suitable crystals are formed. However, because of their high solubility, crystallins are often difficult to crystallize, and their solution structures and dynamics are of particular interest due their being in solution in the biologically relevant state. Therefore, many structural studies have been performed using solution-state NMR, as reviewed in (46) and discussed for several cataract-related variants in Section 5. In addition to providing ensembles of structures in solution,

this method enables the investigation of dynamics over a wide range of timescales and to detect rare conformational states.(47; 48; 49) For example, the solution NMR dynamics of HγD-W42R showed a partially unfolded state in exchange with the native-like structure, yielding insight into its increased susceptibility to proteolysis.(50) NMR can also be used to probe protein-ligand and protein-protein interactions, as has been demonstrated for γS-crystallin and its aggregation-prone variants binding to a fluorescent dye (51; 52) and to the molecular chaperone αB-crystallin.(28; 53)

Building on the strong foundation of information about the monomers, the most urgent set of problems facing this field is the detailed investigation of the insoluble aggregates found in cataract. HPLC and GPC analysis of cataract samples have shown that a cataract is made mostly of non-crosslinked crystallin proteins.(54) Amorphous-looking aggregates have been observed for HγD in the presence of copper and zinc ions (55) and for the HγD-P23T variant (56), whereas HγS and its G18V variant display a mixture of amorphous aggregates and amyloid fibrils, with the relative populations varying based on the aggregation conditions.(57; 58) Amyloid fibrils have also been observed in UV-induced cataracts in both porcine (59) and human lenses (60), raising the question of how prevalent each type of aggregate is, and under what conditions. A characteristic signature has been identified in the 2DIR spectrum that can detect amyloid secondary structure, even if the individual domains contain only 4-5 β-strands.(61) It has been reported that aggregates in cataract lenses can be disrupted by small molecules such as rosmarinic acid (62) or lanosterol and other cholesterol derivatives, (63; 64; 65) preventing and even reversing cataract formation. However, other researchers report that full transparency is not achieved by these compounds (66), and that lanosterol works in canine but not human lenses (67), underscoring the need for continued research on the mechanism of crystallin aggregation and how it can be prevented or reversed.

For large complexes or insoluble aggregates, such as the amorphous or amyloid aggregates formed in cataract, solid-state NMR with magic angle spinning (MAS) is a useful struc-

tural method.(68; 69; 70; 71) This technique can be used either on its own or synergistically with other methods including small-angle X-ray scattering (SAXS), or for larger complexes, electron microscopy. Solid-state NMR has been used to show native-like structure in aggregates of the P23T variant of HγD-crystallin (56), and to solve the structures of αB-crystallin complexes.(72) Solid-state NMR is a promising technique for future detailed studies of the aggregates found in cataract because it has provided some of the earliest detailed information available about the structural arrangement of amyloid fibrils (73), and it continues to be a workhorse technique for solving new fibril structures.(74) Solid-state NMR structures have been solved for fibrils formed for A$\beta_{(1-42)}$ (75; 76; 77), finding multiple polymorphs, including one that displays the same antibody reactivity as amyloid plaques from Alzheimer's brain samples.(78) Structural models generated from solid-state NMR and electron microscopy data have revealed structures of different polymorphs of the A$\beta_{(1-40)}$ peptide.(79; 80; 81) Although parallel, in-register β-sheets appear in both polymorphs, many other structural features differ, including the overall symmetry of the complex, the conformation of the inter-strand regions, and some of the intermolecular contacts. We anticipate that this methodology will prove similarly useful for elucidating the structures of crystallin aggregates. Cryo-electron microscopy can be used for aggregates or complexes involving α-crystallin oligomers and their client proteins, although it is not currently applicable to individual crystallin molecules due to the lower size limit of approximately 38 kDa for single particles.(82)

Fortunately, in many cases relevant biophysical questions can be answered even in the absence of a detailed structural model. Along the way to high-resolution structure determination, several relatively simple experiments can be used to test hypotheses about stability, solubility and protein-protein interactions. Circular dichroism (CD) spectroscopy provides a rapid means of assessing the protein's secondary structure. In CD, the absorbance of a beam composed of equal intensities of left and right circularly polarized light is measured after passing through the sample. Because proteins are highly chiral molecules, the protein

backbone absorbs different amounts of left-rotating or right-rotating light, depending on its secondary structure features.(83) The effective rotation of the plane of the beam is then recorded as a function of the frequency, providing an estimate of the relative amounts of α-helix, β-sheet, and random coil. Different variants of the same protein can be compared to each other, enabling detection of partial unfolding due to mutation or PTMs. The CD spectrum can also be monitored with increasing temperature or denaturant concentration to measure protein unfolding. If the secondary structure is already known or not needed, unfolding can alternatively be monitored using fluorescence spectroscopy experiments.

Built right into the $\beta\gamma$-crystallins is a set of very sensitive fluorescent probes that allow for characterization of disturbances to the protein structure, in the form of four highly conserved tryptophan residues. A common feature of vertebrate lens $\beta\gamma$-crystallins is an arrangement of two tryptophans in the hydrophobic core of each domain, which naturally acts as a FRET pair to protect the retina from UV light.(84) The fluorescence of these tryptophans is strongly affected by the surrounding chemical environment, making them excellent reporters of the overall fold of the protein. This method is most useful in comparative mode, investigating differences between variants or measuring unfolding during thermal or chemical denaturation. Gathering a large body of data about how crystallin stability is affected by temperature, denaturants, mutation, or modification is essential for understanding the specific mechanisms of protein folding and aggregation.

Light scattering is an accessible method for studying protein-protein interactions and, importantly, aggregation of $\beta\gamma$-crystallins. Scattering experiments are complementary to spectroscopic measurements: the latter elucidate different aspects of the internal structure of the molecule, based on electronic structure, vibrational modes, or the arrangements of nuclear or electron spins, while the former provide information about properties of the proteins as physical particles. Light scattering techniques for investigating protein solution properties can be split into two categories, Static Light Scattering (SLS) and Dynamic Light Scatter-

ing (DLS). SLS measures the intensity of light scattered from particles in a solution, which depends on the hydrodynamic radius and mass.(85) Because scattering also depends on the molecular orientation, the intensity of scattering is measured at a variety of angles in what is known as Multi-Angle Light Scattering (MALS). Particularly when combined with size exclusion chromatography to isolate individual species (86), MALS enables determination of the second virial coefficient or A2 (87; 88), which effectively reports on the favorability of protein-protein interactions. A2 is a measurement of the mean potential force between two particles in a solution.(89) In contrast, DLS measures fluctuations in scattering intensity at a single angle over time, which can be used to estimate particle size as well as the diffusion coefficient.(90) This makes DLS an excellent tool for investigating aggregation of particles over time, or as a function of changing conditions. DLS is often used to characterize the aggregation of crystallins as a function of temperature or pH, or upon addition of salts or other solution components.

Small-molecule fluorophores, such as Thioflavin T (ThT) and 8-anilino-1-naphthalenesulfonic acid (ANS), are useful probes for investigating crystallin structure and interactions. These fluorophores bind to the protein of interest, producing observable changes in their fluorescence spectra such as frequency shifts and changes in intensity (Figure 1.3). ThT fluoresces strongly when bound to amyloid fibrils (91; 92; 93), enabling detection of fibrils and monitoring the kinetics of their formation.(94; 95) ANS and bis-ANS are commonly used as a probe of exposed hydrophobic surface area, although the binding mode also involves electrostatic interactions between the negatively charged sulfate groups on the dye and positive charges on the target protein.(96; 97) For example, ANS fluorescence has been used to characterize the placement of hydrophobic patches on HγS to better understand the α-crystallin-client protein binding interface.(52) These small molecule probes can be used to quickly and inexpensively probe the aggregation state of a protein and detect partially unfolded intermediates.

The absorption spectra of transition metals overlap with the fluorescence emission spectra of

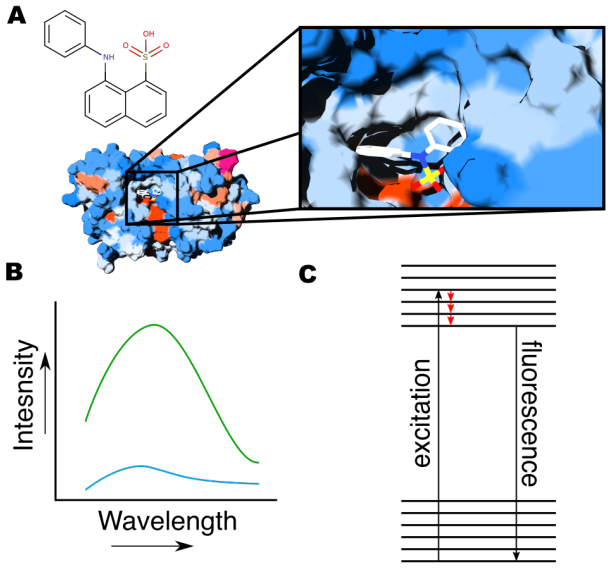

Figure 1.3: Schematic representation of ANS binding. ANS binding can be used to probe hydrophobic surface area. (A) ANS is a mostly hydrophobic small molecule with a negatively charged sulfate group. This allows the molecule to bind to exposed hydrophobic pockets on a protein, as shown in this docking simulation of a predicted structure for the G18A variant of γS-crystallin binding to ANS. The protein structure is color coded from blue (hydrophobic) to orange (hydrophilic). (B) When ANS binds to a protein, it will fluoresce more strongly; hydrophobic surface exposure correlates with intensity, as shown in this simulation of a γS-G18A (green) compared to γS-WT (blue) suggesting that the hydrophobic core of the protein is more exposed in the variant. (C) This florescence in the bound state is caused by the absorption of a photon, causing electronic excitation; when the electron relaxes back to the ground state, energy is released as a lower-energy photon.

protein functional groups, thereby providing a donor (fluorophore)/ acceptor (metal) pair. Non-fluorescent transition metals quench donor emission over a distance range between 10 and 20 Å , on account of a small Förster distance (R_o) that is on the scale of the biomarcomolecule's length. The short R_o coupled with an inherent inverse-sixth-power distance dependence makes tmFRET a powerful tool for studying intramolecular interactions.(98) A schematic illustrating tmFRET is shown in (Figure 1.4). The wide range of absorption spectra between transition metals and transition metal chelator complexes allows for donor/acceptor-pair tuning.(98) Furthermore, transition metals are advantageous acceptors, as they can be used in either native or synthetic metal-binding sites, can be reversibly bound through chelation, and are less restricted by orientation as they have several absorp-

tion dipoles.(98) For proteins without native metal binding sites, di-histidine binding sites can be introduced through mutagenesis, or chelators such as EDTA can be attached with short linkers.(99)

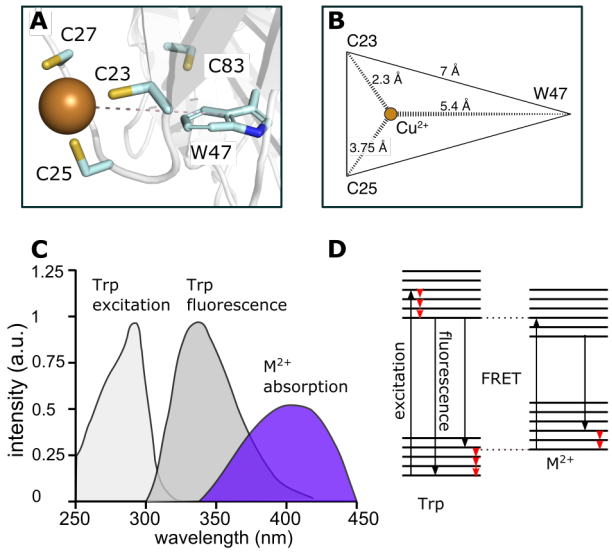

Figure 1.4: Transition metal Förster resonance energy transfer (tmFRET) and an example of a crystallin protein where it is useful. (A) A model of one of the Cu^{2+}-binding sites of HγS, showing the Cys residues that coordinate the metal ion FRET donor, and the nearby Trp 47, which acts as a FRET acceptor. (B) Schematic depiction of the interactions in (A), with key distances labeled. Both (A) and (B) are based on data from.(58) (C) Drawing showing the approximate positions of relevant spectral peaks. Trp in a protein has a strong absorption peak centered at around 280 nm, and fluorescence at around 350 nm (although this can vary considerably depending on the local environment.) Transition metals such as Cu^{2+} often have a relatively broad absorbance peak at around 400 nm, allowing for substantial overlap with the Trp fluorescence, and hence FRET. (D) Jablonski diagram indicating the various energy transfer mechanisms, including excitation, fluorescence, FRET, and vibrational relaxation (small red arrows.)

1.4 Cataract-related mutations in structural crystallins often cause increased aggregation propensity

So far, there are over 30 reported mutations associated with hereditary cataract, many of which are summarized in a review by Vendra et al.(100) To give a few examples, structures

have been solved for cataract-related variants of HγD-crystallin, including R58H (36), P23T (101; 102), γD-R76S (103), γD-V75D (104), and a variety of deamidation variants.(105) For HγS, structures have been solved for γS-G18V (28), γS-G57W (106; 107), and the deamidation variants N14D and N76D.(108) Themes have emerged from biophysical and structural characterization of $\beta\gamma$-crystallin variants, including relatively subtle structural differences from wild-type, increased hydrophobic surface exposure, higher susceptibility of the N-terminal domain to unfolding, and the formation of multiple unfolding intermediates.

The solution-state NMR structures of the G18V (28) and G57W (107) variants of HγS (HγS-G18V and HγS-G57W, respectively) are both similar to that of the wild-type protein (HγS-WT) without major structural rearrangement. However, for both proteins, biophysical experiments had previously showed that these variants are less stable and more aggregation prone.(109; 110; 106) Solid-state NMR spectra of HγD-P23T aggregated under physiological conditions are consistent with the local structure of the protein being nearly identical to HγS-WT.(56) These are described as amorphous-looking; however, their solid state NMR peak dispersion and linewidths are consistent with a high degree of structural homogeneity.(56)

Although they are not misfolded, HγS-G18V (52), HγS-G57W (107), and γD-P23T (56) all have increased hydrophobic surface area compared to γS-WT, as well as subtle but widespread perturbations to the N-terminal domain (NTD), where each mutation is located, whereas the C-terminal domain (CTD) remains unchanged. Despite their minimal structural perturbations, cataract-related variants of γS-crystallin behave differently in the crowded solution of the eye lens, as evidenced by differing interactions with surface water (45) and with small molecules in the lens.(111)

The isolated domains of HγS and HγD are each very stable, although in both cases the NTD is less stable than the CTD.(38) The many observations of crystallin aggregation mediated by partial unfolding of the NTD, while largely leaving the CTD unchanged, furthers the hypothesis that the NTD is stabilized by the interdomain interface.(39; 112; 113; 38)

A particularly dramatic example of this effect occurs in HγD-V75D, where denaturation experiments in urea revealed that it is possible to unfold the entire NTD while the CTD retained a native structure.(104) The residues of the NTD occupy more conformations than those found in the CTD (114), and the NTD shows a higher degree of flexibility in the HγD-G57W variant over WT.(115) In a cataract-related variant of mouse γS-crystallin, a single mutation, F9S in the first β-strand destabilizes the first Greek key motif, promoting unfolding of the NTD under even mild heat stress.(116) The HγS-Y67N, was recently discovered in a Chinese family with autosomal dominant nuclear congenital cataracts.(117) In this protein, structural destabilization leading to reduced thermal and chemical stability relative to HγS-WT(118) takes the form of disrupting one of the tyrosine corners that are essential for stabilizing Greek key motifs.(107)

Another example of this unfolding mechanism was found in the zebrafish γM7 crystallin, which has a CTD that is highly similar to that of HγS and, in contrast, an N-terminus with key sequence differences, especially between residues 67-72. Specifically, this protein lacks one of the strongly conserved tryptophan residues found in other vertebrate γ-crystallins, leading to a restructuring of the loop between β8 and β7. This amplifies hydrophobic packing, presumably to compensate for the loss of the bulky Trp in the hydrophobic core while maintaining the Greek key motif. These structural differences likely reflect the evolutionary constraints of the fish crystallins to perform in a more densely packed eye lens that is under less UV stress compared to its land counterparts.(32)

Destabilization is strongly associated with aggregation, although the correlation is not always straightforward. (110; 42) Complete unfolding is often prevented by intramolecular hydrophobic contacts, salt bridges, disulfide bonds, or by the chaperone activity of α-crystallin. This can give rise to an accumulation of partially unfolded intermediates, which may be more physiological relevant than completely denatured proteins, given the preserving nature of the eye lens (119), though there is some evidence of fully denatured proteins in cataractous lenses

as well.(120)

Similar aggregation-prone variants are also observed in β-crystallins. Compared to their WT counterparts, the mutants HβB2-W59C (121), HβB2-W151C (121), HβB2-S175G/H181Q (122), and HβB2-R188H (123) all have increased hydrophobic exposure, decreased stability, decreased solubility and an increased propensity to aggregate. The dependence of the NTD stability on that of the CTD is highlighted in the comparison of stability and solubility between the HβB2-W59C and HβB2-W151C variants.(121) Both of these tryptophan residues are conserved in all human lens $\beta\gamma$-crystallins, although these studies indicate that mutating them is not equivalent in terms of structural disruption. Every form of characterization used indicates that the W151C mutant is far more perturbed relative to WT than W59C. Both mutations of HβB2-S175G/H181Q are in the fourth Greek key motif. Hydrogen/deuterium exchange mass spectrometry experiments revealed significant conformational changes in the loop region that transverses the CTD and connects the two Greek keys (122), suggesting that this loop region is critical for stabilization. In HβB2, R188 forms an ion pair with E75 in the intradomain interface between the Greek keys.(29) HβB2-R188H disrupts this pairing and, therefore, the equilibrium among different oligomeric states: this variant exists mostly as a tetramer, rather than the native dimer.(123) The reduced solubility and stability can therefore be associated with the loss of stabilization from homodimer formation. HβB2-V187E aggregated rapidly upon expression in bacteria, and was found almost solely in inclusion bodies.(123) Molecular dynamics simulations suggested the mutation completely disrupted folding of the domain. Across all crystallins, a hydrophobic residue is conserved in this position, supporting the idea that this position is a critical part of the hydrophobic core. In contrast, the CTD was only slightly loosened by the HβB2-V187M mutation, a conversion to another hydrophobic residue.(123)

At neutral pH, HβB1-R233H does not greatly alter the degree of hydrophobic exposure or solubility compared to WT HβB1. The mutation slightly alters the structure and increased

aggregation propensity at high temperatures. However, this aggregation did not correlate to decreased stability; in fact, HβB1-R233H had an increased stability compared to WT. Rather, the increased aggregation propensity may be due to the increased hydrophobic character of the C-terminal extension.(124) Increased hydrophobicity of the C-terminal extension was also considered as the cause of aggregation for HβB1-X253R, a cataract-associated variant with a 26-amino acid C-terminal extension. The mutation had only minor effects on stability and structure, but a large increase in the aggregation propensity.(125)

Heterooligomerization has been shown to increase the solubility of β-crystallins (126; 127; 128) and coexpression has been used as a tool to stabilize and solubilize these proteins.(129) In general, acidic β-crystallins are less stable than basic β-crystallins. (130; 131) Although HβB1-R233H increased the stability of the protein in isolation, the βA3/βB1 heterodimer was destabilized. The formation of the heterodimer was unaffected, suggesting that R233 plays a role in heterodimer stabilization.(124) Xi *et. al.* argue that these trends in stability imply that R233 destabilizes βB1 and plays a functional role in beneficial heterodimer formation rather than contributing to the inherent stability. This could be extended to the C-terminal extension, generally, as the X253R mutation also weakened the dimerization of βA3/βB1. Therefore, mutations in this region could cause cataract by disturbing heteroligomerization *in vivo*.(125) The HβA4-G64W variant is destabilized and improperly folded. This mutation caused an increase in aggregation that was not ameliorated by coexpression with HβB1. Therefore, HβA4-G64W is likely unable to bind to HβB1, suggesting a role for G64 in heterodimerization.(132) HβB2-R188H was unable to stabilize HβA3 like WT, suggesting this mutation also affects the heterodimer formation. In contrast to the monomeric γ-crystallins, β-crystallin functionality is not a simple function of individual protein solubility and stability: these proteins must be considered in the context of the chemical milieu of the lens.

1.5 Age-related cataract often results from post-translational modification

Although studying the aggregation mechanism of cataract-associated variants of the γ-crystallins is very instructive from the standpoint of protein biophysics and sequence-structure-function relationships, most instances of cataract disease are not congenital but result from post-translational modifications (PTMs) accumulated during aging. (133) These PTMs include deamidation, glycation, acetylation, and products of oxidative damage (134), all of which can dramatically effect protein stability and intermolecular interactions. Here we discuss the chemical mechanisms underpinning the formation of these PTMs, as well as their implications for protein solubility.

1.5.1 Deamidation

Deamidation is a spontaneous process where the amide group on an asparagine or glutamine side chain is replaced with a carboxylic acid (Figure 1.5). The mechanism proceeds via a cyclic intermediate, which leads to a mixture of the D and L versions of both aspartate and isoaspartate.(135) These deamidation events play a functional role in some tissues (136; 137), but in structural lens proteins they are primarily a deleterious effect of aging and exposure to UV radiation.(138; 139) In irradiated rat lenses, proteomic analysis revealed many different PTMs; however deamidation of Asp and Glu residues were among the most common.(140) The degree to which deamidation at any particular site contributes to the formation of cataract is an open question, as the solubility impact appears to depends on both which isomer is formed and where in the protein it is located.(141; 142; 143) Many detailed investigations of specific deamidation-mimicking variants have been performed, some examples of which are discussed below.

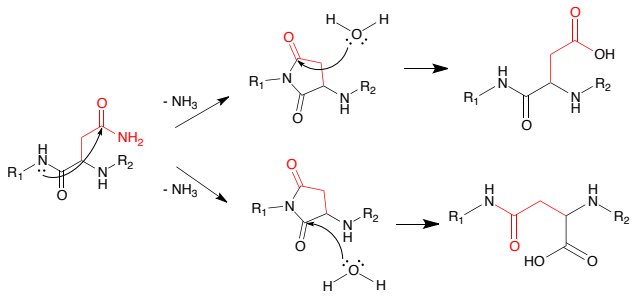

Figure 1.5: Deamidation of asparagine and glutamine residues yield their acidic counterparts, altering the biophysical properties of the protein. Backbone amide attack of asparagine or glutamine residues result in succinimide or glutarimide intermediates, respectively. Hydrolysis results in either conversion of the starting amide to an acidic residue (top) or breaking of backbone amide bonds to form iso-aspartic acid (γ) or iso-glutamic acid (bottom), respectively.

In human βB1, deamidation leads to destabilization and a less compact dimer structure, whereas truncation of either the N- or C-terminal extensions does not impact stability with respect to urea denaturation.(144; 145) βB2- (146) and βA3-crystallins (147) are similarly destabilized by single or double deamidation, although their overall structures remain largely native-like. Deamidations also impact the dynamics of β-crystallins in the context of homo- and heterodimers: enhanced flexibility, especially for βB2, may promote the formation of larger oligomers that could lead to cataract.(148)

Deamidation also causes destabilization and altered intermolecular interactions in γ-crystallins. Although the structures of the N76D and N143D variants of HγS are similar to HγS-WT, these variants exhibit increased attractive forces to other proteins.23456789(149) The deamidation-mimicking N76D and N14D variants of HγS exhibit increased aggregation propensity and are more susceptible to oxidative damage.(108) This investigation also showed that both the N- and CTDs of these variants are more flexible and expose more of the hydrophobic core, leading to two possible drivers of aggregation. One is that the increase in flexibility drives aggregation directly via the presence of aggregation-prone unfolding intermediates, and the other is that deamidation events make the protein more susceptible to other PTMs, further impacting solubility. HγS-N76D has an increased propensity for dimer formation

and decreased resistance to denaturants relative to HγS-WT, although it is resistant to thermal aggregation.(150) A triple mutant mimicking the effects of multiple deamidations ($H\gamma$S-N14D/N76D/N143D) is more destabilized and aggregation-prone than any of the single mutants, and resists solubilization by αA-crystallin.(151) On the other hand, a thorough study of HγD where all 7 of its Asn residues were individually mutated to Asp revealed no major changes in stability, solubility, or aggregation propensity. The structures of all these variants, as measured by both x-ray crystallography and solution NMR were also largely unchanged, providing compelling evidence that deamidation of individual residues in HγD does not initiate aggregation leading to cataract.(105) An interesting topic for future investigation is whether deamidation variants of HγD are more susceptible to oxidation and other deleterious modification, as observed for HγS by Forsythe et al.(108), which would provide a mechanism for their involvement in cataractogenesis even if the impact of the deamidations themselves on protein structure is minimal.

1.5.2 Oxidation

Another important set of modifications that are relevant to crystallin aggregation are those brought about by oxidative damage. Although the lens contains a reservoir of glutathione (152), it is depleted with age (153; 154), and thus oxidative damage is one of the most abundant types of post-translational modifications in the lens nucleus.(155) Oxidative damage can truncate the protein through backbone cleavage(156) or sidechain modification. In particular, the sidechains of Met, Trp, and Cys are prone to oxidation-driven modifications that accumulate over time and are found in high rates in cataractous lenses.(157; 158) Cysteine oxidation and the formation of disulfide bonds can perturb native structure or form intermolecular disulfide bridges that decrease solubility and lead to larger aggregates.(159) Tryptophan oxidation has been shown to destabilize the protein (160), and would also disrupt the UV-filtering capability of the two highly conserved tryptophan pairs (161; 84), which

effectively absorb potentially damaging radiation and redistributes the energy via thermal motion.(162)

Despite the various protective features in the lens, frequent exposure to UV radiation can cause free radical formation that leads to oxidation products. Cations of redox-active metals such as iron (163) and copper are also implicated in crystallin oxidation. It is difficult to predict and isolate all the potential products; however, oxidative damage has been localized to specific side chains such as methionine, cysteine, and tryptophan in proteins of mouse lenses.(158) The chemical and biophysical properties of bovine γ-crystallins are altered after treatment with a strong oxidizing agent, with increased hydrophobic exposure and more disulfide-based protein cross-linking.(164) A more detailed discussion of disulfide cross-linking in the crystallins can be found in section 7.2. In addition to their baseline increase in aggregation propensity, many cataract-related crystallin variants also have increased susceptibility to oxidative damage. Six cataract-related variants of HγD- and HγC were found to be more aggregation-prone than WT after treatment with UV light or hydrogen peroxide.(165) Aggregates with different morphologies have been reported upon oxidation. UV-B irradiated mixtures of α, β, and γ-crystallins result in amyloid fibril based aggregates (166), while amorphous-looking aggregates have been formed from UV-irradiated HγS.(57) Small-molecule antioxidants that can prevent or mitigate oxidative damage are of great interest, as they may some prophylactic value for cataract prevention. Compounds such as (-)-epigallocatenchingallate (167; 168; 169), herperetin (170) and green tea flavonols (171) have been shown to prevent oxidative damage to crystallins in vitro. These compounds could serve as an important starting point for finding effective preventative measures for age related cataract.

1.5.3 Proteolysis

Truncation of crystallins is another form of age-related damage observed in aged lenses; however, proteolysis has a complex role in the development and maintenance of the healthy lens. Enzymatic digestion by proteases in the eye lens has a beneficial function during lens development and even into adulthood.(172) The ubiquitin-proteasome pathway is functional in lens fiber cells (173), although activity of both the ubiquitination machinery and and proteasomes are reduced with age, probably due to depletion of the necessary enzymes.(174) While it is active, this cellular disposal system can remove crystallins that are damaged by oxidation or repeated exposure to UV light, but as the lens ages and the diffusion barrier between the nucleus and the outer part of the lens becomes more pronounced (175), damaged proteins are accumulated rather than removed by proteolysis.(176) The ubiquitin-dependent proteolytic pathway is critical for the degradation of oxidatively modified proteins (172), which otherwise aggregate and bind to membranes (177; 178), contributing to the hindrance of diffusion in aged lenses. At least one congenital cataract mutation where the lack of solubility is due to increased sensitivity to these natural housekeeping proteases. The S129R variant of human βB1-crystallin has enhanced sensitivity to proteolysis, and is associated with an autosomal dominant congenital cataract-microcornea syndrome.(179)

Non-enzymatic cleavage of crystallins is also an important process in the lens, as the long-lived crystallin proteins are susceptible to various forms of damage that render them aggregation-prone, especially in the absence of a functional ubiquitin-proteasome system, as in the aging lens. This type of modification is often concomitant with both oxidative damage and deamidation. At neutral to mildly basic pH, spontaneous deamidation of Asp and Gln residues often occurs via formation of a succinimide intermediate (180), but if formation of this intermediate is prevented by the local tertiary structure, the amide nitrogen of the backbone may act as the nucleophile instead of the sidechain NH_2, leading to backbone cleavage either as a competing pathway, or after deamidation has occurred (Figure 1.5).(181; 182) As

expected from the dependence on three-dimensional structure, these modifications are not randomly distributed but instead depend on the neighboring residues.(183; 184) The side chains of nearby residues may also be involved in the chemistry, with serine being particularly likely to participate in truncation (185) or racemization, albeit via distinct chemical mechanisms.(186) In some cases, backbone cleavage can also lead to interprotein cross-link, further compromising solubility.(187; 188)

1.5.4 Tryptophan derivatives in the lens

Tryptophan metabolites produced from the kynurenine pathway in the anterior cortical epithelial cells (Figure 1.6) are capable of mitigating the damage of frequent ultraviolet radiation exposure in the eye lens. These small molecules absorb some of the radiation that passes through the cornea, particularly in the 300-400nm wavelength range, and dissipate the energy as vibrational motion.(189; 133) These UV-filtering metabolites are depleted in aged lenses (190), making the lens proteins more susceptible to UV-induced damage.(191) Although kynurenine and its derivatives play a photoprotective role on their own, their chemical reactivity can also promote oxidative damage and aggregation and are under investigation as an accelerant of brunescent cataracts. Oxidized tryptophan metabolites can form covalent linkages to crystallins or GSH, a major route of 3OHKyn depletion.(191)

The covalent linkage of tryptophan metabolites to nucleophilic residues, especially lysine and histidine, destabilizes the protein, leading to cataractogenisis.(194; 195) A possible source of oxidation could be through hydrogen peroxide produced from the interactions 3-hydroxykynurenine (3OHKyn) and 3-hydroxyanthranilic acid (3OHAA) with Cu^{2+}.(196) The 3OHKyn and 3OHAA precursors (Figure 1.6) lack the *o*-aminophenol group and do not promote metal ion-mediated hydrogen peroxide, emphasizing the necessity of the hydroxyl group for redox activity, possibly due to resonance stabilization of the radical species.(196)

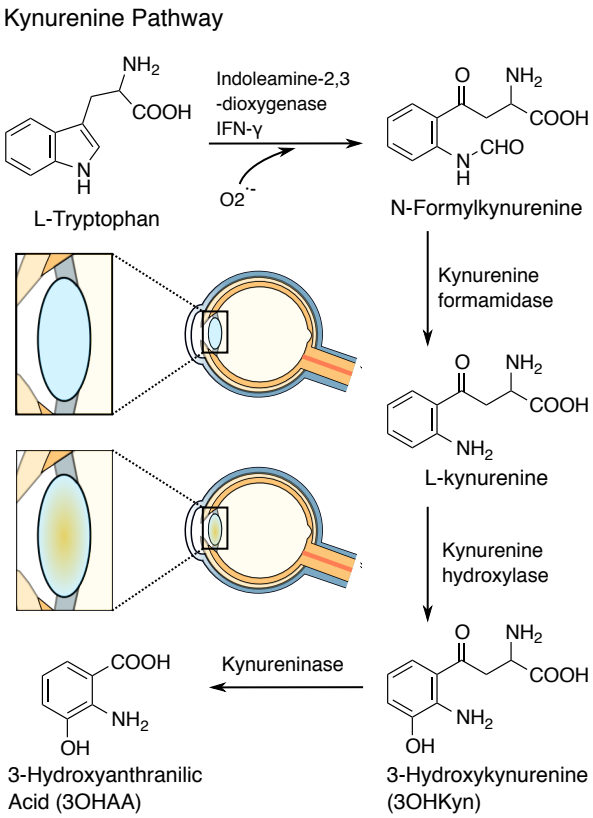

production.(192; 193)

Figure 1.6: The formation of tryptophan metabolites through the kynurenine pathway. Enzymes are indicated adjacent to each arrow. At the beginning and the end of the pathway are drawings illustrating the healthy lens and the development of brunescent cataracts as a result of tryptophan metabolite.

Cross-linked crystallins are found extensively in cataractous lenses.(197; 190) Tryptophan metabolites are known to form covalent linkages on crystallins and are readily oxidized into reactive species. Indeed, incubations of α-crystallin with 3OHKyn or 3OHAA produce crosslinks that are greatly amplified in the presence of Cu^{2+}, even without UV exposure. Similarly, incubations of 3OHKyn and 3OHAA with bovine lens protein (BLP) in the dark produced no appreciable amount of higher molecular weight species until Cu^{2+} or, to a lesser extent, Fe^{2+} was co-incubated.(189) Cu^{2+} was rapidly converted to Cu^{1+} with accompanying oxidation of the *o*-aminophenol group. One proposed mechanism of cross-linking requires two equivalents of metal ion per 3OHAA or 3OHKyn to perform one-electron transfers that form quinonimine species that are susceptible to Michael additions.(189)These investigations

highlight the complexity of crystallin aggregation in the eye lens and support the assertion that elevated levels of metal ions found in the eye are causative agents of cataract.

1.6 Metal ion-induced interactions

The ubiquitous $\beta\gamma$-crystallins of the vertebrate lens are believed to have evolved from ancestral Ca^{2+}-binding proteins, and orthologs that bind divalent cations are found in a variety of organisms, including many that lack eyes. The pathway for crystallin evolution is generally assumed to be selection for stability and solubility, often followed by loss of the original activity, in this case metal binding, along the way to gaining its new optical function.(6; 21) This process is illustrated by the *Neurospora crassa* abundant perithecial protein (APP), an early crystallin ortholog that is highly aggregation-resistant at high protein concentrations and lacks functional calcium ion binding sites.(198) Unlike related proteins, human $\beta\gamma$-crystallins lack the ability to bind Ca^{2+}.(199)

Increased divalent cation concentration in the eye lens, which can be caused by aging (163), smoking (200; 201), or diabetes (202; 203), is associated with lens opacification and cataract formation. Each crystallin protein has idiosyncratic interactions with each metal ion, even among crystallins in the same family and for ions of the same charge and similar size. Here we discuss several mechanisms by which metal ions can induce aggregation. Though these mechanisms are considered separately, even *in vitro* synergistic interactions between different mechanisms is likely to be important, and *in vivo* additional factors such as cellular density (204), protein diversity, point mutations, and post translational modifications will also affect metal ion-crystallin interactions.

Metal ions in the eye lens can destabilize crystallins through coordination of residues that are forced to adopt distorted conformations to make contact with the ion. As with hereditary

point mutations, this structural perturbation can lead to aggregation. For example, tryptophan fluorescence and CD experiments show that human HγD is significantly destabilized and often aggregates in the presence of Cu^{2+} and Zn^{2+}.(55) Separately from or in addition to their destabilizing effects, coordination of metal ions can also lead to intermolecular metal ion-bridged aggregates: these are often detected by testing whether metal chelators such as EDTA or DTT diminish or reverse aggregation.

Copper and zinc ions, which have distinct bioinorganic properties, interact very differently with human γ-crystallins. Zinc has been found in higher concentrations (205) in cataractous eye lenses, whereas copper is less abundant but has a higher propensity for inducing aggregation. HγD does not appear to interact with Mn^{2+}, Ca^{2+}, Fe^{2+}, or Ni^{2+}.(55) Copper (II)-induced aggregation of HγD exhibits biphasic behavior with respect to concentration: partial unfolding dominated at low Cu^{2+} concentration, whereas ion-mediated disulfide bonding becomes more important at high ($>$ 4 equivalents) Cu^{2+} concentration. A deeper investigation into copper mediated disulfide bond formation indicated Cys111 as a highly likely position for cross-linking formation (159) In contrast to Cu^{2+}-induced aggregation, no biphasic behavior was observed for Zn^{2+}-induced aggregation of HγD. No disulfide bonds were formed, and there was little evidence of HγD destabilization in the presence of Zn^{2+}, consistent with this ion's lack of redox activity.(206) These observations suggest the formation of intermolecular cation-bridged species. Further corroboration of this mechanism came when the elimination of His22 of HγD eliminated aggregation. Conversely, the introduction of a histidine at the homologous positions in HγC and HγS promoted Zn^{2+}-induced aggregation of these proteins that did not occur with either wild-type protein.(206)

Cu^{2+} and Zn^{2+} also play contrasting roles in the aggregation of HγS. As with HγD, both Zn^{2+} and Cu^{2+} strongly promote aggregation, whereas a variety of other metal ions induce it weakly or not at all.(207) Zn^{2+}-induced aggregation was markedly reduced when all solvent-exposed Cys residues were replaced by Ser, and addition of EDTA abolished all

aggregation in both the variant and WT protein, consistent with Cys-mediated bridging. Surprisingly, removal of the solvent-exposed cysteine residues accelerated and increased the extent of Cu^{2+}-induced aggregation.(207) Two distinct binding events were observed using tmFRET and ITC experiments: one at the site of the cysteine loop and the other at a different location, possibly involving normally buried residues that become accessible due to partial unfolding.(58) The Cu^{2+}-induced aggregates could be partially resolubilized using EDTA, and further resolubilized by DTT, which alone produced stable monomers, indicating different aggregation pathways.(58) The presence of oxidized cysteine and methionine residues found through mass spectrometric analysis of trypsin digests suggested that Cu^{2+} was being reduced to Cu^{+}, which would allow for the possibility that Cu^{+} is forming metal ion-bridged aggregates that can only be broken by DTT and not EDTA.(207; 58) As was the case for HγD, HγS aggregation studies suggest that zinc ion-induced aggregation is primarily promoted by bridging, whereas copper ion-induced aggregation proceeds though a complex mixture of oxidation, destabilization, and metal bridging mechanisms.

HγS and HγC are also susceptible to mercury ion-induced aggregation through destabilization and intermolecular disulfide bonding. Increasing equivalents of Hg^{2+} ions steadily decreased thermal stability and increased aggregation and unfolding.(208) Investigations of the N- and C-terminal domains separately found that only the NTD was susceptible to intermolecular disulfide bonds. HγC aggregation in the presence of mercury ions exhibits biphasic behavior. At $Hg^{2+} < 3$ equivalents, aggregation increased and thermal stability decreased with increasing Hg^{2+} to protein ratios. After 3 equivalents, thermal stability began to increase and aggregation decreased, although there was still an increase relative to the protein in the absence of mercury. Studies of the individual N- and C-terminal domains found that each domain followed the pattern seen at low equivalents, suggesting that the biphasic behavior requires both domains to be present. There is evidence of intermolecular disulfide bonds, suggesting that both destabilization and oxidative mechanisms are necessary for aggregation.(208) For this process and for Cu^{2+}-induced aggregation of HγS, more

detailed investigation, for example NMR chemical shift perturbation, would be necessary to determine the origin of the biphasic behavior.

1.7 Protein-protein interactions

Altered protein-protein interactions are an important driver of crystallin aggregation, leading to varied aggregation pathways. MD simulations of the R85D variant of HγD suggest that the biggest difference between R85D and wild-type is an increase in hydrogen bonds, leading to a more rigid protein that is better able to form stable intermolecular contacts, leading to aggregation.(209) MD simulations of the W42R variant of $H\gamma$S suggest that the critical structural change is a loss of hydrophobic interactions holding the two domains together.(210) Computational models of a variety of HγD variants suggested that increases in attractive forces between proteins leads to an increase in aggregation propensity.(211) Simulating HγD under acidic conditions shows that the CTD forms a novel β-sheet.(212) The increased aggregation propensity of HγS-G75V could be related to an increase in the exposure of the hydrophobic core.(213) To provide a more accurate model of charge states influencing the potential energy landscape, a screened electrostatic model was used to define the charge state of HγD, accounting for the effects of neighboring residues on local pKa values of potentially charged side-chains.(214) All of this is confounded by the fact that aggregates are formed by many different mechanisms, often producing a mixed population of aggregates. For example, UV-irradiated samples of HγS-G18V formed amorphous-looking aggregates, while those aggregated under low pH conditions were more fibrillar in nature, although both types are often present in the same sample.(57) HγD also forms both native-like and amyloid aggregates (215; 56), with both having been observed in samples from cataractous lenses.(60; 216; 122)

1.7.1 Condensation/ domain swapping

Domain swapping occurs when two or more identical protein chains or monomers swap elements of their structure to form dimers or open-ended chains.(217) Although this type of exchange or swapping is often found in disease-related aggregates, it can also be used to control and modulate protein function.(218) For example, domain swapping is observed in the native structure of β-crystallins, which comprise highly similar Greek key domains connected by a short inter-domain linker region.(37) Although γ-crystallins are monomeric, β-crystallins are dimers or multimers and exist as a wide range of homo- and hetero-oligomers.(37) βB2-crystallin exists as a domain-swapped dimer in the crystal structure.(37)

In γ-crystallins, domain swapping does not occur in the native state. When it does occur, it can make either closed dimers, which are soluble, or long polymeric chains, which can lead to aggregation. This process often involves partially unfolded states that swap portions of β-sheets to form extended oligomers. For example, HγD can partially unfold in either the NTD (219) or the CTD (220), allowing mixed β-sheets containing strands from both monomers. In oxidation-mimicking point variants where tryptophan is replaced by glutamic acid (HγD-W42E, W68E, W130E and W156E), aggregation occurs via domain-swapped polymerization.(221) In HγD-W42E and W42Q, an intramolecular disulfide bond traps the protein in a partially unfolded conformation that exposes β-strand edges, facilitating this kind of aggregation.(222) Surprisingly, mixing this variant with the wild-type protein exacerbates its aggregation (160), which has important implications for how oxidation damage can promote cataract, as oxidized proteins in vivo are in contact with a large reservoir of undamaged ones.

1.7.2 Disulfide bonds

Intra- and intermolecular disulfide bonds are common PTMs, particularly in aged and cataractous lenses where protective antioxidants are depleted.(155) Intramolecular disulfide bonds may perform an oxidoreductase function, serving as a buffering system through a disulfide exchange mechanism, especially as a last resort mechanism after eye lens antioxidants have been depleted.(223) Key to this theory was the observation that aggregation of the W42Q variant was initiated by WT HγD in a prion-like model.(160) The proximal cause of aggregation is the transfer of a disulfide bond from an oxidized WT HγD to the variant. The transferred disulfide bond acts as a thermodynamic sink, trapping the protein in a conformation that favors aggregation.(223) Using this exchange model as a buffering system would require the formation of thermodynamically equivalent disulfide bonds. Furthermore, oxidized WT HγD, which contains only one disulfide bond between Cys108 and Cys110, is capable of oxidizing the Cys32-Cys41 disulfide bond (Figure 1.7), leading to aggregation.(223) Other investigators have found independently that Cu^{2+} can oxidize the intramolecular Cys108-Cys110 disulfide bond on HγD (Figure 1.7).(159) In protein disulfide isomerases (PDIs), a family of enzymes that catalyze the oxidation, reduction, and isomerization of disulfides, intra- and intermolecular disulfide exchange is rapid and reversible.(224) PDIs have a *CXXC* motif; however, the functional sequence can be further minimized, as viable PDI mimics were prepared with a *CXC* motif.(225) Other examples of redox-functionalized disulfide bonds in *CXC* motifs are found in thiol oxidase Erv2p (226) and Hsp33.(227) This is relevant to crystallin disulfide exchange because HγD contains a similar CSC motif, which is believed to form a strained disulfide bond that is susceptible to reductive cleavage.

In summary, $\beta\gamma$-crystallin aggregation can result from mutations or a number of environmental factors. A schematic illustrating the currently known types of $\beta\gamma$-crystallin aggregation is shown in Figure 1.8.

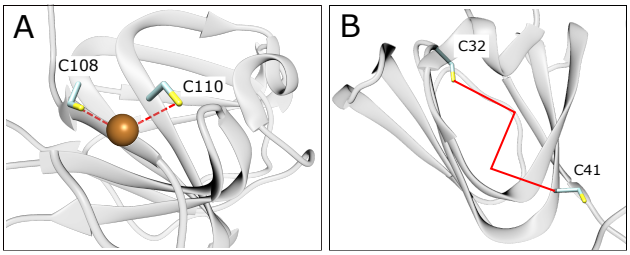

Figure 1.7: Disulfide bond schematic view(A) Cu^{2+} oxidization of the intramolecular Cys108-Cys110 disulfide bond on HγD (PDB: 1HK0). (B) Oxidization of the Cys32-Cys41 disulfide bond leading to aggregation of HγD (PDB: 1HK0).

1.7.3 LLPS

Liquid-liquid phase separation (LLPS) occurs when a protein solution spontaneously separates into dense liquid droplets dispersed in a dilute solution.(228; 229) LLPS can be triggered by changes in temperature, pH, salt concentration, or interactions with other macromolecules.(228) This type of phase separation is a functional mechanism for cells to organize and maintain different cellular compartments (230), producing membraneless organelles to segregate particular chemical components without lipid bilayers.(230; 231) The dark side of LLPS is protein aggregation: aggregation of misfolded proteins in neurodegenerative diseases often starts with the formation of dense liquid droplets.(230)

Some structural crystallins and their mixtures are susceptible to formation of LLPS, often in response to lowered temperature, a phenomenon called cold cataract, which is schematically depicted in Figure 1.9. This phenomenon has been known in the eye lens since at least the early 1980s, when light scattering experiments were first used to characterize the size of the droplets in different vertebrate lenses.(232; 233; 234) Bovine γB-crystallin undergoes LLPS near 0 °C, but this transition can be suppressed by the addition of an appropriate concentration of α-crystallin.(235) Cold cataract resistance in fish is of particular interest, because deep-sea fish are adapted to withstand low temperature and high pressure, a challenging environment for the lens proteins. The Antarctic toothfish, *Dissostichus mawsoni*, has at least 13 expressed γ-crystallin paralogs.(236) Although the whole lens of *D. mawsoni* resists

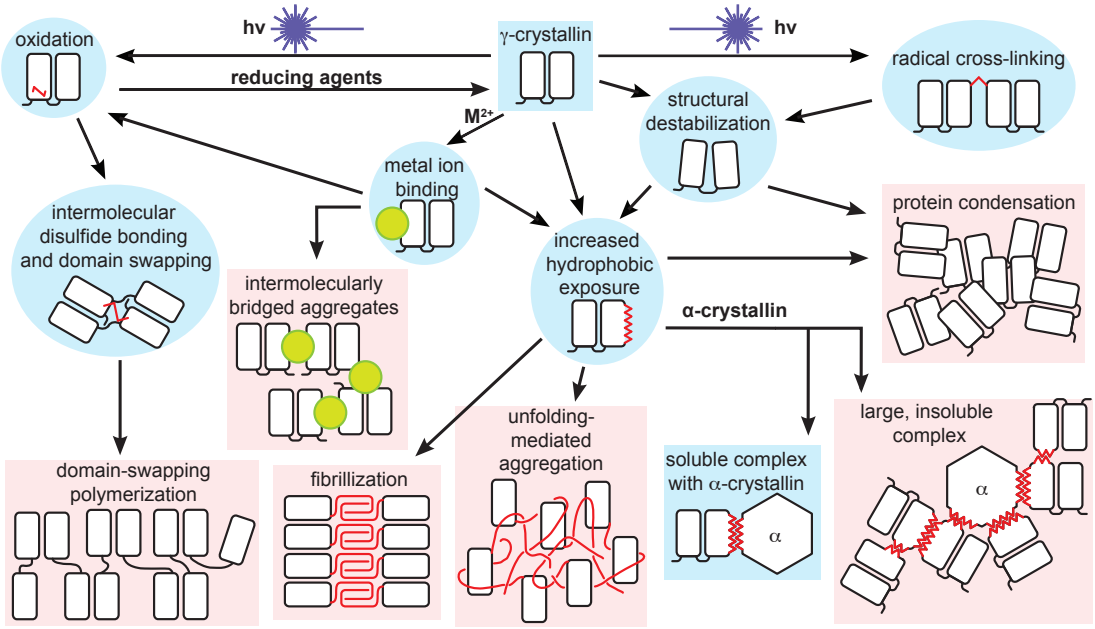

Figure 1.8: Schematic representation of several possible aggregation pathways for γ-crystallins. Rectangular shapes indicate stable states, whereas rounded shapes denote transient species. Species shown on blue backgrounds are in solution; pink backgrounds indicate insoluble aggregates. Red lines indicate modifications to the protein structure. This schematic is not a comprehensive representation of all potential HγS- aggregation pathways, but instead illustrates currently known mechanisms.

cold cataract down to at least -12 °C, below which it freezes solid (237), the individual γ-crystallins vary greatly in cold-cataract resistance despite their high sequence identity.(238) Wild-type toothfish γM8b phase separates at -4.8 °C, but mutating only three Arg residues on the surface to Lys makes it more resistant to cold cataract than any of the wild-type proteins tested, with an onset temperature of -13.7 °C, illustrating the importance of specific protein-protein interactions. Conversely, mutating three Lys residues to Arg raises the onset temperature of LLPS by an equivalent amount, to 3.5 °C (238), demonstrating that LLPS can be controlled by making subtle changes to protein surface properties, even in well-folded proteins. The importance of specific surface interactions were hinted at in early studies, for example the finding that phase separation induces major changes to the Raman spectrum of tyrosine in lens proteins.(239) Recently, high pressure was found to drive phase-separated solutions of human and rat γD-crystallin back into homogenous solution, hinting at a mech-

anism for deep sea fish to avoid cold cataract. Addition of trimethylamine-N-oxide (TMAO), which is found in the tissues of organisms living at high pressure (240), induced LLPS under the same conditions (241), suggesting that this piezolyte may assist in the formation of functional membraneless organelles in deep ocean environments.

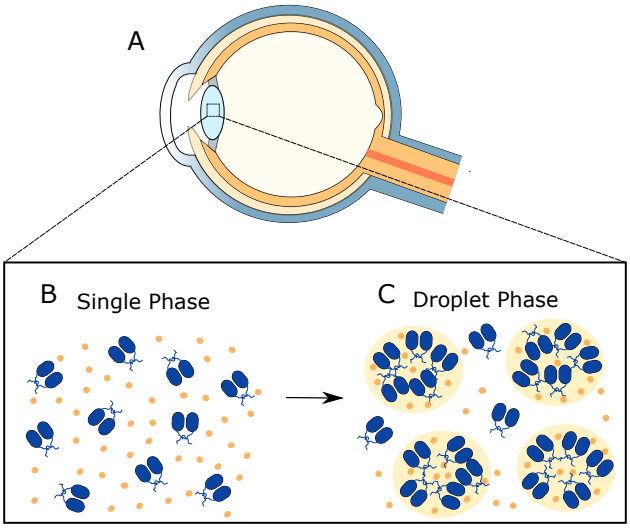

Figure 1.9: Schematic view of liquid-liquid phase separation (LLPS). (A) Drawing of the human eye, showing the position of the lens. (B) A γ-crystallin protein in a homogeneous phase. (C) In LLPS, the solution partitions into protein-rich and protein-poor phases, forming droplets and producing reversible opacification.

1.8 Conclusion and outlook

All of the $\beta\gamma$-crystallins share very similar three-dimensional structures, but they differ in details such as surface properties and the lengths of the extensions at the termini. Even in cataract-related variants, the basic structural unit comprising two double Greek-key domains is maintained, and unfolding is often minor and transient or happens only under stress conditions. However, because of the unforgiving constraints on lens protein solubility, even subtle structural changes can have a large impact on their solution properties. Small differences in hydrophobic exposure and salt-bridging interactions, which can be observed using CD, intrinsic fluorescence, dye binding, and light scattering experiments, appear to be main

drivers of $\beta\gamma$-crystallin aggregation, along with alterations in the surface hydration layer. These observations are in contrast to the large-scale misfolding and structural rearrangement often observed in other protein deposition diseases. The altered protein dynamics resulting from these small changes can be observed in NMR experiments (242), informing our understanding of solvent accessibility and expansion of the $\beta\gamma$-crystallin interactome to include new disulfide bonds, metal-protein interactions, and protein-small molecule interactions, potentially allowing for future design of therapeutics that target vulnerable conformational states.

For the next phase of crystallin research, it is critical to move beyond the solution-phase behavior of monomers and dimers toward high-resolution structures of crystallin aggregates and a detailed understanding of their formation kinetics. One potential complication for studying $\beta\gamma$-crystallin aggregation is the difficulty in distinguishing native protein, amorphous aggregates, and amyloid fibrils, all of which have primarily β-sheet secondary structure. Sorting out and classifying the different species involved will require a mixture of physical chemistry and structural biology techniques. Fortunately, the intense interest in amyloid fibrils over the last two decades has yielded a useful suite of experimental modalities for distinguishing different β-sheet structures. In particular, solid-state NMR continues to provide many of the high-resolution structures available for amyloid fibrils.(74) Optical spectroscopy provides another route to distinguishing aggregates and oligomers with similar secondary structures, as variations in β-sheet structure correlate with infrared (IR) spectroscopic observables.(243) 2D IR spectroscopy has been used to observe the divergence of different fibril polymorphs in human islet amyloid polypeptide (hIAPP) from a common intermediate in solution (244), and to monitor the transformation of Aβ oligomers to fibrils.(245) A recently developed topological classification for amyloid fibril structures (246; 247) could also be extended to provide a more systematic description of β-sheet oligomers and non-amyloid aggregates.

For proteins that are supposed to be chemically inert, crystallins undergo rich and varied

chemistry that always seems to surprise the investigator. In this review we have discussed PTMs that arise from interaction with products of the kynurenine pathway, metal ion interactions, oxidations and deamidations that have been uncovered in lenses with age-related cataract. Recent evidence suggests that disulfide bond formation between solvent exposed cysteines in γ-crystallins may serve as a buffering system, through disulfide exchange, to prevent harmful oxidations.(58; 223; 248) Formation of these dimers appears to be a last resort buffer, since high concentrations of these dimers eventually promote the formation of larger aggregates. The mechanisms by which aggregates are formed in the eye lens, whether they be amorphous-looking aggregates, amyloid fibrils, or a combination of the two, is still largely unknown. Understanding these phenomena requires details of protein-protein interactions that happen during normal homeostasis and after perturbation. Here we reviewed protein-protein interactions via domain-swapping and condensation, disulfide bond formation, and LLPS. Identification of site-specific interactions via NMR and X-ray crystallography in known cataract-causing variants and PTMs represent an important basis for developing an overall understanding. The vertebrate lens proteins serve as a counterpoint to the emphasis on amyloid fibril formation as the mechanism underlying protein deposition diseases: understanding protein solubility also requires studying highly soluble proteins, the flip side of aggregation. In addition to the direct impact on cataract, understanding how these extraordinary proteins maintain their solubility will enable the design of highly soluble proteins and provide more general insight into hydration of complex molecules with a variety of functional groups.

Chapter 2

Human γS-crystallin resists unfolding despite extensive chemical modification from exposure to ionizing radiation

2.1 Introduction

Protein stability and aggregation resistance are intimately connected with solvent interactions. Hydrophobic hydration in general is more complicated than the traditional "oil and water" picture suggests, as the balance between attractive and repulsive interactions depends on molecular size and geometry as well as solute polarity (249).Vibrational spectroscopy has established that at low to moderate temperatures, water assumes a structure with more tetrahedral order and fewer weak hydrogen bonds around hydrophobic solutes than the bulk solution (250), although dangling O-H bonds are also observed near solvated hydrocarbons

(251). Exposed hydrophobic functional groups can also form highly flexible π-hydrogen bonds, where the donor is a water and the acceptor is the π-system of the aromatic amino acid side chain (252). Microscopic interactions between water and the heterogeneous functional groups of protein surfaces impact many protein properties beyond solubility, including diffusion of water near the protein surface (253; 45; 254), the compressibility (255) and even the refractive index increment (23).

Water is not just a passive solvent within cells, but is a key participant in many biochemical reactions (256). Water facilitates electron transfer in enzymes, mediating tunneling between adjacent molecules (257) or stabilizing radical intermediates in the active site (258) via hydrogen bonding. In the type of radiation damage investigated here, water acts as a transmission medium for oxidative damage: direct damage of proteins by γ rays is a minor effect, with most of the deleterious modifications coming from reactions with reactive oxygen species (ROS) derived from water, primarily hydroxyl radical, although hydrogen peroxide is also significant (259). Inside the cell, OH radical is particularly damaging, as it is highly reactive and cannot be neutralized enzymatically, unlike H_2O_2 (260). Although DNA damage is often emphasized in studies of radiation toxicity, proteins are oxidized by hydroxyl radical before DNA or lipids (261). The resulting protein hydroperoxide species can last for several hours and have the capacity to damage other molecules and deplete the cellular supply of antioxidants (262). Assessing the impact of radiation damage is important for understanding the mechanisms of radiation tolerance in extremophiles (263; 264), the cellular damage caused by radiation therapy for cancer (265), and the potential for cataract formation as a consequence of ionizing radiation absorbed by the eye.

Exposure to ionizing radiation has been shown to cause cataract in humans and model organisms (266). Populations susceptible to radiation cataract include radiological technicians (267), astronauts (268) and others who have accidental, occupational, or war-related exposure to ionizing radiation.(269; 270; 271) The upper dose limits of γ irradiation to the lens

suggested to prevent the onset of cataract are as low as 0.05 Gy over 5 years.(272; 273) These findings raise the question of whether radiation-induced cataract is a direct consequence of protein modification and aggregation or whether more complicated cellular damage is involved. The majority of the lens protein content comprises α- β- and γ- crystallins.(204) β- and γ- crystallins are structural proteins, whereas α-crystallins act as molecular chaperones. Studies on α- crystallins have shown that γ irradiation forms oxidation products, generates extensive cross-linking, damages the overall fold, and reduces chaperone activity. A previous investigation showed that rat lenses dosed with 5 Gy of γ radiation formed site-specific oxidations on γ- crystallins, particularly on cysteines, tryptophans, and methionines.(158; 274) Antioxidants such as vitamin E(275; 276) and melatonin(277) have delayed the onset of radiation-induced cataract in model organisms, further supporting an important mechanistic role for ROS.

Here we investigate resistance to unfolding of human γS-crystallin (HγS), a major structural protein of the eye lens, upon exposure to γ radiation. Structural crystallins such as HγS are extremely stable and soluble, in keeping with their biological role. The vertebrate eye lens is primarily composed of enucleated lens fiber cells that undergo degradation of internal organelles during early development, in part due to lipase activity (278) and the ubiquitin-proteasome system (279). The loss of most cellular components leaves behind a highly concentrated (> 400 mg/mL) solution of proteins, mostly crystallins (204). Crystallin solubility persists despite damage caused by aging, exposure to ultraviolet (UV) radiation, modification by reactive oxygen species (ROS), and other deleterious chemical reactions (155; 280). Glutathione and other antioxidants provide some protection from ROS (152), however many post-translational modifications (PTMs) have been observed in aged lenses, including deamidation and oxidation (139; 281).

The aggregation resistance of the proteins themselves is partly due to fluorescence quenching mechanisms that quickly relax excited states via thermal motion before photochemistry can

occur.(161; 282; 84) This wealth of information about aggregation resistance in structural crystallins leads to questions about the response of these highly soluble proteins to radiation damage, which has been shown to cause cataract: are structural crystallins such as HγS resistant to aggregation upon exposure to ionizing radiation? If they are, is it a result of increased resistance to oxidative damage or because the proteins are able to tolerate a high level of chemical modification while remaining soluble? Our results indicate that HγS is unusually robust to unfolding even when treated with high levels of γ radiation and that this resistance is due to its high tolerance for modification rather than resistance to oxidative damage. We also investigate the identity of the PTMs caused by irradiation of HγS and discuss future directions for investigation.

2.2 Materials and methods

2.2.1 Protein expression and purification

Human γS-crystallin (HγS) was produced using a construct containing an N-terminal 6× His tag and a TEV cleavage sequence (ENLFQG), which leaves a glycine in place of the initiator methionine. This gene was cloned into a pET28a(+) vector (Novagen, Darmstadt, Germany) and overexpressed in Rosetta (DE3) *E. coli* cells using Studier's autoinduction protocol (283). Cell pellets were collected via centrifugation at 4,000 rpm for 30 minutes, resuspended, lysed, and respun at 14,000 rpm for 60 minutes. The protein was purified via nickel affinity chromatography, digestion with TEV protease (produced in-house), a second round of nickel affinity chromatography (to remove the cleaved His tag), and finally, size exclusion chromatography (SEC) on a GE Superdex 75 10/300 (GE Healthcare, Pittsburgh, PA). All samples were dialyzed into H_2O, lyophilized for storage at -80 °C, and resuspended in H_2O unless otherwise stated.

2.2.2 γ irradiation

Protein solutions at 5 mg/mL in water (100 μL) in glass vials were irradiated with a ^{137}Cs source (^{137}Cs Irradiator Mark-I, Model 68, JL Shepherd & Associates, San Fernando, California, USA). Sample concentration was determined from the absorbance at 280 nm using an extinction coefficient of 42,860 M^{-1} cm^{-1}. Post-exposure concentrations were calculated from the final volume after sample dilution or concentration using 5 mg/mL as the known starting concentration. A metal sample holder was used to maintain consistent sample distance from the source. The dose rate has been previously calibrated with Fricke dosimetry(284; 285). Fricke dosimetry was used to confirm the expected dose for our sample position, volume, and vials(286). Solutions of 0.4 M sulfuric acid, 6 mM ammonium ferrous sulfate and 1 mM potassium chloride were well-agitated for aeration and irradiated for 5 and 10 minutes. The absorbance at 304 nm was measured and the dose was calculated using a G-value of 15.5 mol/100 eV, extinction coefficient of 2022 M^{-1} cm^{-1}, a density of 1.024 g mL^{-1} and a path length of 1 cm(287). The calculated dose rate at our sample position was 1.54 kGy/hr, matching the expected dose rate. Unless otherwise noted, all data were collected within 12 h of removal from the γ irradiation source.

2.2.3 Ultraviolet (UV) irradiation

For both UVA and UVB exposure, protein solutions were 6 mg/mL in 10 mM HEPES, 50 mM NaCl, pH 7. Sample volume was 2.5 mL in a 1 cm $\times$ 1 cm quartz cuvette. Samples were continuously stirred and temperature controlled at 22 °C using a Quantum Northwest Luma 40/Eclipse with a Peltier element and recirculator (Quantum Northwest Inc., Liberty Lake, WA, USA). For UVA exposure, a 10 Hz Nd:YAG laser (Continuum Surelite II; Surelite, San Jose, CA, USA) was coupled to a Surelite Separation Package (SSP) 2A (Surelite) to change the pump laser wavelength (1064 nm) to 355 nm via third harmonic generation. The laser

flux was 29 mJ/cm^2 at 10 Hz. Samples were exposed for 180 min. For UVB exposure, a 70 mW light emitting diode (LEUVA66H70HF00, Seoul, Korea) at 5 mm distance (120 degree view angle) was used, yielding a mean power density of 58 mW/cm^2. Samples were exposed for 90 min.

2.2.4 SDS-PAGE

20 μL of protein was mixed with 20 μL of loading dye (62.5 mM Tris-HCl, 2% sodium dodecyl sulfate (SDS), 25% glycerol, 0.01% bromophenyl blue, pH 6.8). For reduced samples, 1 μL β-mercaptoethanol was added and samples were heated at 70 °C for 90 seconds. Samples were run on a 15% polyacrylamide gel at 180 V for 60 minutes and stained using Coomassie blue dye.

2.2.5 Ellman's assay

To evaluate the amount of solvent-exposed thiols in solution, the non-irradiated and irradiated protein solutions were diluted to 0.5 mg/mL in 100 mM Tris pH 8.0. 5,5′-dithiobis(2-nitrobenzoic acid) (DTNB) was added to reach a final concentration of 0.1 mM. The solutions were incubated at room temperature for 30 minutes before collection of spectra on a Jasco V-730 spectrophotometer (JASCO, Easton, MD). A molar extinction coefficient for thiobis(2-nitrobenzoic acid) (TNB) of 14150 M^{-1} cm^{-1} was used to calculate the concentration of sulfhydryl groups(288; 289).

2.2.6 Circular dichroism (CD)

Circular dichroism (CD) spectra were collected using a J-810 spectropolarimeter (JASCO, Easton, MD). Spectral bandwidth was set to 2 nm. All samples were diluted to 0.1 mg/mL.

2.2.7 Intrinsic fluorescence

Fluorescence spectra were measured using an Agilent Cary Eclipse fluorescence spectrophotometer with excitation at 295 nm. All samples were diluted to 0.1 mg/mL.

2.2.8 Raman

Raman studies were perform using a Raman microscope system based on a Renishaw InVia microscope. The sample was excited with a 532 nm laser (¡3 mW) and spectra were collected using grating of 2400 gr/mm and under 20 s exposure time. Sample concentration was 100 mg/mL. 4 μL of sample was deposited on a glass slide and a spacer and glass coverslip was added to prevent dehydration.

2.2.9 Fourier-transform infrared spectroscopy (FTIR)

FTIR spectra of lyophilized protein samples were measured using a Jasco FT/IR-4700 (JASCO, Easton, MD) equipped with .in attenuated total reflection geometry fashion using ATR PRO ONE over the 400-4000 cm^{-1} range with 2 cm^{-1} resolution.

2.2.10 Proteolytic digestion

For samples exposed to γ-irradiation for 1 hour, digestion was performed on an aliquot of the water-soluble portion of the irradiated samples, as no significant pellet was observed upon centrifugation. For samples exposed to γ-irradiation for 5 hours as well as for the UV irradiated samples, the samples were centrifuged at 13,000 x g for 15 min and the water-insoluble fractions resolubilized in 8 M urea, 1 M ammonium bicarbonate pH 8.0. For trypsin digestion, the protein samples were denatured in 8 M urea, 1 M ammonium bicarbonate pH 8.0 for 1 h at 37 °C. The buffer was diluted or buffer exchanged to 1.6 M urea and trypsin was added in a 1:20 ratio. The digest was carried out overnight at 37 °C. Immediately prior to analysis, DTT was added to 10 mM and the sample was heated at 80 °C for 3 minutes. For pepsin digestion, the sample was exchanged into approximately 1% formic acid (pH 1.6) and pepsin was added in a 1:20 ratio. Samples were incubated at 37 °C for 2 hours.

2.2.11 Liquid chromatography - mass spectrometry (LC-MS)

Mass spectra were collected on a Waters Xevo XS-QTof using either a phenyl column for intact protein mass spectra or a C4 column for peptide digests. Buffer A was 0.1% formic acid in water. Buffer B was 100% acetonitrile. For the protein intact mass spectra, the flow rate was 0.2 mL/min with a gradient of 0% to 97% B over 1.5 min then 97% B for 0.5 min. For the peptide digest mass spectra, the flow rate was 0.3 mL/min with a gradient of 3% to 27% B over 24.0 min, a gradient of 27% to 90% B over 3.0 min, then 90% B for 0.5 min. Intact mass spectra were analyzed using MassLynx with MaxEnt1 used to deconvolute the spectra. Peptide digests were analyzed with BioPharmaLynx.

2.3 Results and discussion

HγS was irradiated in a ^{137}Cs γ source at 5 mg/mL in glass vials (Figure A.1). The samples are positioned equidistant in a ring around the sample source and the dose rate at this distance has been previously calibrated (285). We confirmed our samples were receiving the expected dose using Fricke dosimetry (Figure A.1) .

2.3.1 HγS resists unfolding after high doses of γ irradiation

We used circular dichroism (CD) spectroscopy and intrinsic tryptophan fluorescence to assess the extent of unfolding in irradiated HγS. We aimed to determine whether HγS undergoes structural changes after irradiation that may be linked to radiation-induced cataract. Both the CD and fluorescence measurements indicate that HγS is remarkably resistant to unfolding upon even prolonged γ irradiation.

The CD spectra of proteins exhibit characteristic bands that report on secondary structure (290). Here we compare the CD spectra of non-irradiated HγS to irradiated samples to detect partial or complete unfolding. In previous studies of HγS, even small changes in secondary structure due to mutation or partial unfolding were observable, i.e. as frequency shifts and shoulders on the major peaks. (110; 291) For γ irradiated HγS, the CD spectra of all samples up to 10.8 kGy show a strong negative peak at 218 nm, which is characteristic of the primarily β-sheet structure of this protein (Figure 2.1A). At 33.9 kGy there is a loss of negative intensity at this position and broadening of the negative band toward 204 nm, where there is a new peak minimum. Similar shifting and broadening of the CD minimum at 218 nm was previously observed for γ-crystallins denatured with guanidine hydrochloride. (292) The same trend was observed for HγS that was aggregated through incubation with copper and resolubilized, (58) as well as for UV-C irradiated, aggregated, and resolubilized

HγD (293). In a previous study of human αA- and αB- crystallin, molecular chaperone proteins that are also abundant in the lens, CD was used to monitor secondary structure as these proteins were subjected to increasing doses of γ irradiation. The secondary structures of αA- and αB- crystallin were disrupted at a dose of 3.0 kGy and 1.0 kGy of irradiation, respectively. (294) In contrast, here we show that the solubility and secondary structure of HγS is preserved up to at least 10.8 kGy.

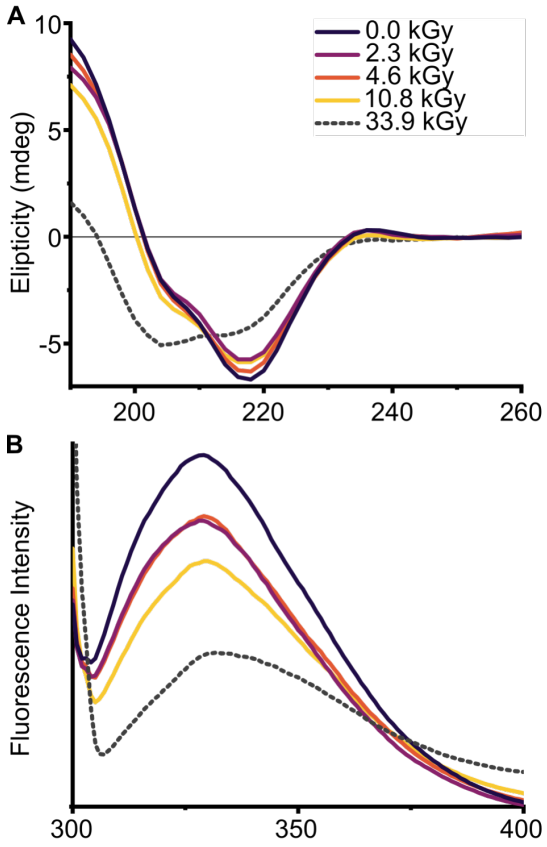

Figure 2.1: The structure of HγS was monitored using circular dichroism (CD) and intrinsic tryptophan fluorescence spectroscopy. (A) CD and (B) fluorescence spectra of HγS irradiated from 0 kGy (black), 2.3 kGy (purple) 4.6 kGy (orange), 10.8 kGy (yellow), 33.9 kGy (grey, dashed). HγS resists significant secondary structural rearrangement past 10.8 kGy.

For γ-crystallins in particular, intrinsic tryptophan fluorescence provides a nuanced view of the protein's folding state. Here we corroborated the CD results with fluorescence spectra collected over the same time course. The most obvious change in these spectra is the decrease

in fluorescence intensity as irradiation increases. The arrangement of the buried tryptophans in the core of HγS has a powerful quenching effect on fluorescence; therefore, full denaturation typically increases the fluorescence signal. (84) However, other effects can alter tryptophan fluorescence intensity in the absence of full unfolding, such as transient contact with solvent molecules as a result of secondary structure destabilization(295) or modifications that alter the chemical structure of tryptophan such as conversion of tryptophan to kynurenine or other oxidation products(296).

The position of the emission maximum is more straightforward to interpret: previous work has shown shown that the fluorescence emission maximum of β- and γ-crystallins shifts from approximately 325 nm to 340 nm when the protein is fully denatured. (131; 39) Displacement of the typically buried tryptophans through denaturation exposes the residues to the more polar solvent, causing a redshift in fluorescence emission maxima upon excitation at 295 nm. (297) Partial unfolding or increased molecular motions increase the solvent accessibility of the tryptophans, leading to shifts in the spectra of a few nm.(291) The fluorescence maximum of HγS remains at 329 nm, consistent with a fully folded protein, through 10.8 kGy of irradiation (Figure 2.1B). After 33.9 kGy, the peak shifts from 329 to 332 nm. The CD spectra and fluorescence data both indicate that the structure of HγS is unperturbed past 10.8 kGy of γ irradiation.

2.3.2 HumanγS accumulates mass modifications after γ irradiation

The production of hydroxyl radicals via γ irradiation would serve as a platform for understanding PTMs produced not only from exposure to this for of detrimental irradiation, but other common damage species that are found in the aged lens. γ irradiation damages proteins largely through the formation of ROS which in turn attack the protein rather than

direct modifications. UVA (298) or UVB (299) parts of the solar spectrum are also known to produce ROS in biological systems. Damage to biomolecules can also be caused by Fenton chemistry, where hydrogen peroxide induces redox cycling of certain metal ions (canonically, Fe^{2+} to Fe^{3+}, but also Cu^{+} to Cu^{2+}), forming hydroxyl radical and other highly reactive species (300; 301; 302; 303).

The best-characterized PTM of structural crystallins is deamidation (138; 280), which lowers stability and alters dynamics, potentially generating aggregation-prone transient conformations (108; 151). Oxidation is another common PTM, particularly in aged lenses that have reduced antioxidant levels. Residues that are particularly vulnerable to oxidation include cysteine, methionine, histidine, and tryptophan (155; 304).

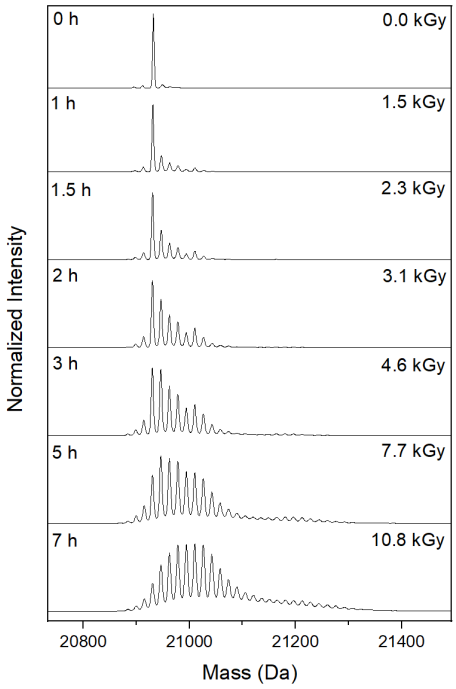

Figure 2.2: Deconvoluted intact mass spectra HγS samples irradiated with doses (0, 1.5, 2.3, 3.1, 4.6, 7.7, and 10.8 kGy) of γ radiation. HγS accumulates successive +16 Da and -16/-17 Da modifications over the course of irradiation.

Despite its remarkable resistance to unfolding, HγS accumulates many mass modifications

from γ irradiation. Intact mass spectra were obtained to determine if any modifications to the protein mass occurred during irradiation (Figure 2.2). HγS has an expected intact mass of 20932 Da, which appeared in the purified protein spectrum shown in Figure 2.2 (top). During irradiation, a number of mass modifications accumulated that led to both increases and losses in mass. Mass increases appear to be mostly due to oxidations, with successive increases of +16 Da, consistent with multiple oxidations on the same protein molecule.

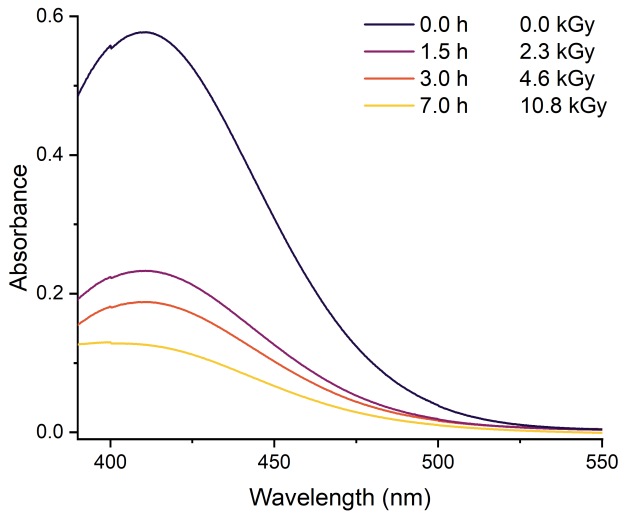

Figure 2.3: Absorbance spectra of non-irradiated and irradiated samples after reaction with Ellman's reagent, DTNB. The absorbance at 412 nm was used to calculate the concentration of free thiols.

The sulfur-containing amino acids cysteine and methionine are known to be particularly susceptible ROS and to form various oxidation states including sulfenic, sulfinic and sulfonic acids and methionine sulphoxide for methionine, respectively (305; 306). Disulfide bonds are also likely to form under oxidizing conditions.(305) To detect the presence of free thiols in non-irradiated and irradiated samples, we performed Ellman's assay. Ellman's assay utilizes the reaction of cysteine side chains with 5,5'-dithiobis-(2-nitrobenzoic acid) (DTNB) to quantify the free thiols in solution(288; 289). This assay was performed under nondenaturing conditions to assess the amounts of solvent-exposed thiols in solution. Figure 2.3 shows the non-irradiated sample, which has a free thiol content of 41 μM. This corresponds to 3.4

solvent-exposed thiols per protein molecule, consistent with structural analysis of the NMR and crystal structures of HγS that indicate 3 out of the 7 cysteines are highly solvent-exposed: C23, C25, and C27(28; 248). With increasing γ irradiation dose, the solvent-exposed thiol concentration decreased to 16, 13 and 9 μM after 1.5, 3.0, and 7.0 h, respectively. These concentrations correspond to 1.4, 1.1 and 0.7 solvent-exposed thiols per protein molecule for the 1.5, 3.0, and 7.0 h irradiated samples, respectively.

In general, protein oxidation via ROS has been extensively reviewed.(307) The side chains of lysine, histidine, tyrosine, tryptophan, and phenylalanine are likely targets for addition reactions: lysine residues oxidize to aminoadipic semialdehydes (308); histidine oxidizes to asparagine, aspartic acid, and oxo-histidine (309; 308); tryptophan converts to 2-,4-,5-,6-, and 7-hydroxy-tryptophan, formylkynurenine, 3- hydroxykynurenine, and kynurenine (310); tyrosine forms 3,4-dihydroxyphenylalanine or dityrosine crosslinks (310); and the oxidation products of phenylalanine are 2-,3-, and 4-hydroxyphenylalanine and 3,4- dihydroxyphenylalanine (310). Oxidation patterns induced by hydroxyl radicals are well-characterized and predictable, leading to their use in oxidative-based footprinting methods (311). This technique exposes proteins to hydroxyl radicals that oxidize amino acid side chains at a rate determined by solvent exposure. Side chains that are buried or involved in protein-protein interactions can be identified by their resistance to oxidation (312). This type of footprinting is particularly useful when fast, laser-induced hydroxyl radical production is combined with modern mass spectrometry detection methods (313), a strategy that has been used to characterize protein-peptide (314) and antibody-epitope binding (315), among others. We expected to observe similar patterns of protein oxidation as γ irradiation produces hydroxyl radicals.

In addition to the expected oxidations, the intact mass spectra of the γ irradiated protein also indicate the presence of other modifications. We noted a spike at the 5$\times$ oxidation state (+80); we hypothesize that an additional mass change may add +80 Da that overlaps with

the 5× oxidation state. Another possibility suggested by other known PTMs is O-sulfation on serine, threonine, or tyrosine residues, although the source of SO_3 is unknown in that case(316; 317). We also observed mass losses in the irradiated samples. The resolution of the intact mass spectra makes it difficult to determine within 1 Da the exact mass of this shift; however, it appears to fall between -16 to -17 Da. There appears to be a succession of mass losses, with an apparent 1× mass loss at -16/-17 and 2× mass loss at -33/34. The loss of 17 Da may correspond to the formation of succinimide via a sidechain nucleophilic attack on the protein backbone. Succinimide formation is readily achieved by aspartic acid which can then racemize to D-aspartic acid, (183) a common PTM in aged lenses (141). Succinimide formation has been shown to increase in UVC irradiated α-crystallins(318). The amount of β-linked aspartic acid, which is also formed through a succinimide intermediate, has been shown to increase in γ irradiated α-crystallins.(319). However, other modifications may overlap as well. For example, dehydroalanine formation from cysteine generates a -34 Da mass loss from the conversion of the thiol group to an olefin and has been detected as a product of protein-ROS interaction using MS/MS. (320)

In this study, we focused on the short-term mass changes and structural stability of HγS by analyzing all samples within hours of removal from the γ-irradiation source. However, intact mass spectra collected from later time points (immediately after irradiation compared to 4 hours after irradiation and 1 week after irradiation) show an increase in the amount of modified protein (Figure A.2). We hypothesize that γ radiation generated ROS continue to react with the protein after removal from the energy source, consistent with previous reports that these interm ediates last hours to days. (321; 307)

2.3.3 Oxidative damage was identified on Lys, Met, Trp, Leu, and Cys

To identify the modifications, samples irradiated for 1 h/1.5 kGy were digested and analyzed with liquid chromatography tandem mass spectrometry (LC-MS/MS). This type of data-independent acquisition (DIA) allows for a less biased approach as all peptides are included in the analysis. Protein digestion was performed by proteolysis with both trypsin and pepsin on the 1.5 kGy dose samples. Trypsin digestion was performed under denaturing conditions, with the protein first incubated in 8 M urea for 1 h then diluted to 1.6 M urea for an overnight incubation with trypsin. A pepsin digest was added to increase coverage (322). Both the trypsin and pepsin digests from 1.5 kGy samples mostly lacked distinct, identifiable peptides in the irradiated sample. This result was unexpected based on the modifications observed in the intact mass spectra of the irradiated samples. One modification was identified from the pepsin digest of the 1.5 kGy irradiated sample, the peptide GSKTGTKIF showing a -1 Da loss (Table 2.1). The b and y ion plots show that the location of the mass shift is in the first three residues (Figure A.3). Of the three residues, lysine is the mostly likely target of oxidation. Aminoadipic semialdehyde derivatives of lysine resides are known oxidation products of lysine that yield a -1 Da loss (323). This modification has been reported in crystallins in aged human eye lens, where its concentration increased with age and in the presence of diabetes, both conditions which increase cataract susceptibility (324). The semialdehyde has been reported to further oxidize to the carboxylic acid derivative, 2-aminoadipic acid (324).

The lack of unique peptides in the 1.5 kGy irradiated sample digest suggested that the modifications to HγS as a result of γ irradiation were so heterogeneous that each modified peptide has a very low individual signal, making identification of any particular species by mass spectrometry difficult. We therefore looked to increase the signal for the modified peptides by analyzing samples with longer irradiation times, 5 hours with a dose of 7.7 kGy. Addition-

ally, we analyzed the precipitated fraction (which was not evident in the 1.5 kGy samples) in order to observe an increased fraction of modified peptides. The water-insoluble fraction was resolubilized in denaturing buffer and subsequently digested with trypsin. Enriching the sample for modified proteins aided in identifying the sites of oxidation from radiation exposure. It should be noted that accurately measuring concentration post-exposure using UV absorption is challenging, as the UV absorption profile can change significantly due to the oxidation of the aromatic amino acids. Therefore, a direct comparison of ion count of the modified peptides between samples is not feasible as the total sample concentration may vary. In order to give an approximation of the relative amount of modified peptides between samples, we estimated the percent abundance as the ion count of the modified peptide over the total ion count of all the modified and unmodified forms of the peptide.

(Table 2.1) summarizes the sites of oxidation identified in 7.7 kGy irradiated HγS. We found evidence of oxidation on all methionine residues and one of the four tryptophan residues. We also identified oxidation of one cysteine, C25, consistent with the high solvent exposure of this residue. The b and y ion plots supporting the identified oxidation sites are shown in the Supplementary Information. The methionine residues and W163 each show a single oxidation, with b and/or y ions demonstrating the specific position of the +16 mass addition (Figure A.4–A.9). We also found evidence of oxidation of leucine, with +16 mass addition to L142 (Figure A.10). L133 may also be oxidized, however the b and y ions were not definitive to that position, as the +16 may also added to V132 (Figure A.11). Both leucine and valine have previously been reported to form hydroperoxides and hydroxides in the presence of hydroxyl radicals and oxygen.(306) γ irradiation on a leucine-containing small peptide resulted in the formation of 4-hydroxyleucine with a +16 mass addition as a major product.(325). In contrast to the single oxidations identified for the other residues, C25 was identified as a doubly oxidized species, forming the sulfinic acid derivative. The b and y ions definitively identified C25 as doubly oxidized, rather than a single oxidation of C25 and a neighboring cysteine (Figure A.12). Oxidation of methionine, tryptophan, and cysteine

residues is consistent with the oxidation sites found in γE and γF in rat lenses exposed to γ irradiation.(158)

For comparison, we additionally irradiated HγS with ultraviolet (UV) radiation to determine whether similar products formed. UV radiation has been shown to directly photo-oxidize proteins via absorption by the major chromophoric side chains (Trp, Tyr, Phe, His, and Cys), which in turn may generate ROS and subsequently oxidize other side chains (326; 327). UV irradiation of bovine α-crystallin (328; 318) and human γD (HγD) crystallin (293; 329) showed oxidation of methionine, tryptophan, and cysteine residues. UVA and UVB irradiation of HγS-crystallin has previously been shown to lead to rapid formation of light-scattering, amorphous aggregates *in vitro*(58). We performed trypsin digests on the insoluble fractions after UVA and UVB irradiation. The UV-irradiated samples show a similar pattern of oxidized amino acids, with methionines, tryptophans, and cysteines identified as oxidized products (Table 2.1). UV irradiated samples additionally showed that C23 and C27 formed sulfinic acid derivatives with +32 mass shifts (Figure A.13 and A.14). Previous studies on UV irradiated HγD report the formation of double and triple oxidized cysteines, rather than the single oxidation product (329).

2.3.4 Vibrational spectroscopy reveals chemical signatures of oxidation

To investigate the post-translational modifications (PTMs) caused by γ irradiation, both Infrared (IR) and Raman spectroscopy were utilized, as these techniques are well-suited for probing the vibrational signatures and chemical structures of molecules. Samples were lyophilized prior to analysis to minimize interference from water signals that dominate the mid-IR range.

Several notable changes were observed in the irradiated samples (Figure 2.4. After prolonged

Residue Number	Peptide	Modification	Nonirradiated	γ-rays		UV	
				1.5 kGy	7.7 kGy	UVA	UVB
1-10	GS**K**TGTKITF	$K3^{-1}$	nd	detected[a,b]	-	-	-
42-72	VEGGTWAVYERPNFAGY**M**YILPQGEYPEYQR	$M59^{+16}$	nd	nd	16%	8%	14%
73-79	W**M**GLNDR	$M74^{+16}$	nd	nd	3%	2%	3%
102-125	GDFSGQ**M**YETTEDCPSI**M**EQFH**M**R	$M108^{+16}$	nd	nd	5%	7%	10%
		$M119^{+16}$	nd	nd	8%	11%	11%
		$M124^{+16}$	nd	nd	2%	6%	9%
132-146	**VL**EGVWIFYE**L**PNYR	$V132^{+16}$ or $L133^{+16}$	nd	nd	1%[b]	nd	nd
		$L142^{+16}$	nd	nd	< 1%	nd	nd
159-174	KPID**W**GAASPAVQSFR	$W163^{+16}$	nd	nd	< 1%	< 1%	< 1%
20-36	RYD**C**D**C**D**C**ADFHTYLSR	$C23^{+32}$	nd	nd	nd	2%	3%
		$C25^{+32}$	nd	nd	1%	4%	8%
		$C27^{+32}$	nd	nd	nd	< 1%	1%

nd = not detected

[a]percentage not reported as unmodified peptide not detected

[b]assignment of oxidation to specific residue not definitive

Table 2.1: Oxidation sites identified in γ and UV irradiated HγS. Peptides from pepsin and trypsin digests were separated and identified via LC-MS/MS. The percent abundance is calculated from the ion count of the modified peptide over the total ion count of all modified and unmodified forms of the peptide. No data is available on the presence of the $K3^{-1}$ modification of GSKTGTKIF as pepsin digests were not performed for the 7.7 kGy γ irradiated or UV irradiated samples. The unmodified form of GSKTGTKIF was not detected; therefore, percent abundance is not reported.

irradiation, a new peak emerged at 2835 cm^{-1}, which was tentatively assigned to the C–H stretch mode of aldehydes (330). This observation is consistent with mass spectrometry data that identified an aldehyde derivative of lysine, suggesting γ irradiation-induced peptide modifications.

Additional new peaks were detected at 1373 and 1258 cm^{-1}, corresponding to the stretching modes of sulfur-oxygen double bonds, typically found within the 1372–1335 cm^{-1} range (330). These spectral changes are in agreement with mass spectrometry results that identified oxidized cysteine and methionine residues (Table 2.1). Furthermore, the peak at 1258 cm^{-1} may be attributed to the C–O stretch of carbonyl groups (330), which are commonly associated with oxidative stress in proteins (331; 332).

Raman spectroscopy was also performed on a custom-modified Raman microscopy system

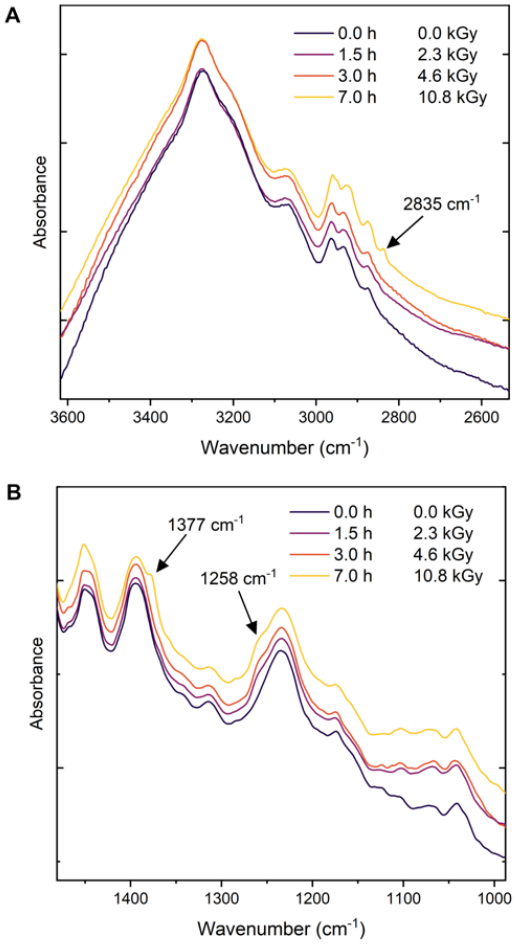

Figure 2.4: IR spectra for samples irradiated from 0.0 to 10.8 kGy from (A) 3655 to 2520 cm^{-1} and (B) 1480 to 990 cm^{-1}. Traces are offset for clarity. Unique peaks that appear after irradiation are indicated with an arrow.

(333). Sample preparation and analysis were optimized on the commercially available protein, hen egg white lysozyme. To perform Raman spectroscopy on proteins on this system, high concentration of proteins need to be used since signatures of post translations modifications have low intensity in the molecular fingerprint region. Therefore, we collected intact mass spectra of lysozyme samples irradiated at both 5 mg/mL and 100 mg/mL to a dose of 1.5 kGy. The lower protein concentration saw a much higher percentage of damage (Figure A.14). This is consistent with damage from ROS derived from water rather than direct irradiation of the protein causing most of the damage. We therefore chose to irradiate the HγS sample at 5 mg/mL then concentrate to 100 mg/mL for Raman data collection to maintain

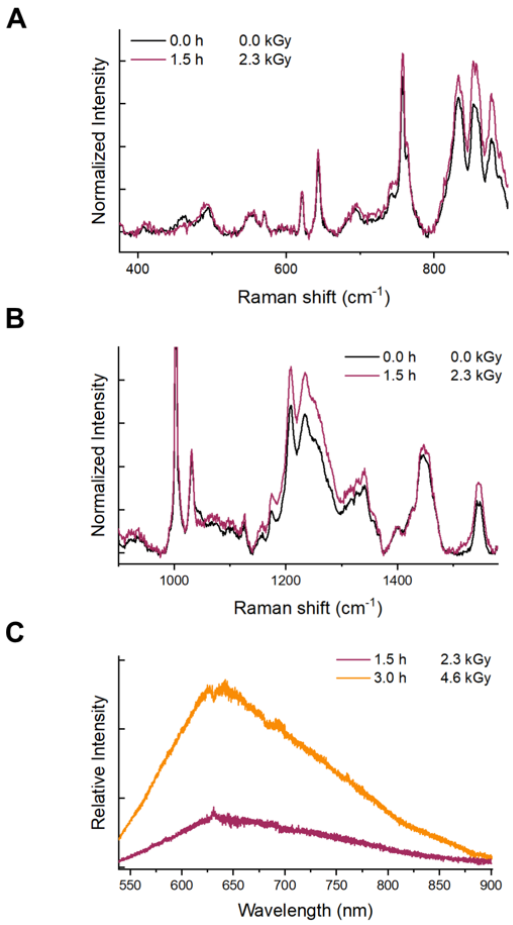

Figure 2.5: Raman spectra of non-irradiated and irradiated HγS from (A) 375 to 900 cm^{-1} and (B) 900 to 1580 cm^{-1}. No significant spectral changes are observed from 1 h/1.5 kGy dose. (C) Fluorescence spectra of irradiated HγS with an excitation wavelength of 532 nm.

sample consistency between techniques. To clearly observe the associated lines and changes, high concentration samples deposited on glass slides were used.(334)

The HγS samples were irradiated at 5 mg/mL then concentrated with centrifugal concentrators immediately after irradiation to reach 100 mg/mL for spectra measurement. The spectra of non-irradiated sample and the sample irradiated for 1.5 h/2.3 kGy is shown in Figure 2.5. Protein peroxides believed to be formed from γ irradiation and can be visualized by Raman spectra (335; 336). No spectral changes were noted and collection of longer irradiation time was precluded since a fluorescent signal dominated the spectra of samples with longer irradiation times. Fluorescence spectra made with excitation wavelengths of 532

nm showed a strong emission profile from 550 to 900 nm (Figure 2.5). To our knowledge, no amino acid derivative with this excitation-emission profile has not been reported. We aim to identify the unknown fluorescent product via further mass spectrometry analysis.

2.3.5 γ irradiation causes non-disulfide covalent cross-linking

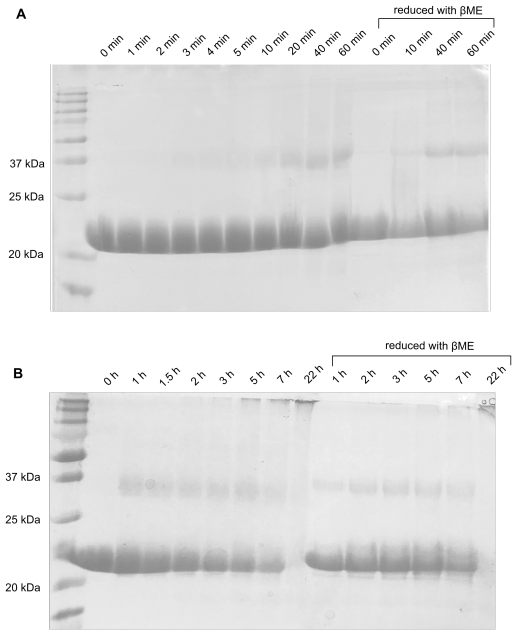

Figure 2.6: SDS-PAGE analysis of non-irradiated and irradiated HγS. (A) Short γ irradiation exposures from 0 to 60 min, up to 1.5 kGy. A dimer of HγS forms that resists reduction with βME. (B) Longer γ irradiation exposures from 0 to 22 h, up to 33.9 kGy. Aggregation appears to increase with longer irradiation times with no remaining monomer or dimer visible at 22 h.

In addition to the side-chain modifications noted in the previous section, γ irradiation appears to lead to chemical cross-linking between protein molecules. Figure 2.6 shows an SDS-PAGE of non-irradiated HγS as well as up to 1 h of irradiation or 1.5 kGy. The gels were intentionally overloaded to increase the visibility of the dimer band. During the course of irradiation, a dimer forms corresponding to approximately 40 kDa. The dimer mass is also seen in the intact mass spectra (Figure A.15). HγS is known to form disulfide-bonded dimers, usually between the solvent exposed C25s in two HγS molecules. However, the

dimers formed after γ irradiation resisted reduction with β-mercaptoethanol (βME), suggesting that these dimers were formed via an alternative cross-linking mechanism. Several crosslinks have been identified in aged and cataractous lenses.(337) Asp/Asn-Lys (338), dityrosine (339), Glu/Gln-Lys (340) have all been identified in human lenses. Dityrosine cross-linking proceeds through a radical mechanism (341) that could be promoted by irradiation and interaction with hydroxyl radical.

Longer irradiation times led to protein aggregation; however, fragmentation was not noted in either the SDS-PAGE analysis or the intact mass spectra. Figure 2.6 shows the SDS-PAGE of the non-irradiated protein and the irradiated protein from 1 h to 22 h. The bands for both the monomer and dimer decrease in intensity over the course of irradiation, while the band at the loading well grows more intense, suggesting that full-length protein is aggregating and no longer able to travel down the gel. By 22 h, no bands are visible in the expected mass ranges for either monomer or dimer. Neither the dimer bands nor the aggregation bands in the loading well are disrupted by reduction with βME, confirming that disulfide bonding is not the main mechanism of crosslink formation.

2.4 Conclusion

Long-lived proteins such as lens crystallins, which have evolved to maintain a stable structure for decades, are particularly vulnerable to the accumulation of detrimental modifications because they are not replenished during the human lifetime. Exposure to ionizing radiation would be expected to cause rapid protein aggregation via the large number of diverse PTMs. Remarkably, despite acquiring many modifications from exposure to γ radiation, HγS-crystallin appears to be resistant to denaturation up to very high doses. Our results clearly confirm the high tolerance for chemical modification of the γ-crystallins, highlighting their evolutionary adaptation as resilient proteins. The present study was mainly focused

on the short-term structural stability of irradiated HγS. However, because cataracts often manifest many years after damage occurs, future studies should also focus on long-term structural stability.

2.5 Author Contributions

M.A.R and B.N.B. contributed equally to protein expression, purification, γ irradiation, SDS-PAGE, circular dichroism, intrinsic fluorescence, Rama Spectroscopy, FTIR, digestion and LC-MS/MS. B.N.B performed the Ellman's assay and the ultraviolet irradiation.

Chapter 3

Investigating the dynamics and stability of HγS crystallin deamidation variants

3.1 Introduction

In order for the human eye to form sharp images the lens cells must be refractive and transparent so that light is properly focused on the retina. Transparency is partially achieved by the degradation of most cellular machinery during embryonic development. However, it is not only the paucity of cellular components that allows the lens to be transparent, it is the impressive solubility of the proteins that remain. These proteins are collectively called crystallins and they exist at concentrations near 400 mg/mL in the human lens. Humans have three types of crystallins - α-, β-, and γ-crystallins. α-crystallins are holdase chaperones that help maintain the solubility of the structural proteins - β- and γ-crystallins. The combination of the inherent refractivity and the high density of the structural crystallins

succeed in forming a highly refractive lens. The solubility of these proteins must be sustained for decades because they are not recycled When crystallin solubility fails the result is cataract - the leading cause of blindness worldwide (342).

In the young lens, elevated levels of antioxidants provide some protection from oxidative damage due to ultraviolet light and chemical stressors. Over time these safety barriers are depleted (343; 344). With age, crystallins accumulate post-translational modifications (PTMs) such as deamidation, oxidation, truncation, and alkylation (345; 280). Concurrently, potentially damaging species, such as metal ions (163), accumulate and α-crystallin chaperone activity declines (346). The most prevalent theory of age-related cataract is these modifications accumulate until a critical point where the crystallins can no longer remain soluble. Deamidation, the conversion of asparagine or glutamine to aspartic or glutamic acid, respectively, is the most common PTM found in the aged lens, raising the question of whether deamidation is a major driver of age-related cataract (347).

Deamidation of both glutamine and asparagine is a stochastic process. Asparagine deamidation is thought to proceed most often through an imide intermediate, which is prone to racemization, followed by hydrolysis to aspartic or iso-aspartic acid (348). Glutamine deamidation can occur through an analogous imide intermediate (180), but evidence suggests direct hydrolysis of the amide is a competitive mechanism (349). Investigations into these mechanisms has been motivated by deamidation's link to cataract and other disease states (350; 351; 352), development of biopharmaceuticals which are prone to destabilzation via deamidation (353), and for its utility as a molecular clock (354).

Cataractous lenses present a difficult subject for identifying site-specific deamidation because aged lenses have abundant and diverse PTMs, with aparagine deamidation alone providing a direct transition into four products (355; 356). Despite the difficulties, several investigations have confirmed the presence of increased deamidation in aged lenses and sites which appear increasingly deamidated in cataractous lenses (357; 358; 359; 347). The abundance of

deamidation at each Asn and Gln of human γS-crystallin (HγS) was quantified in lenses with age-related nuclear cataract (360). Here, and in a previous investigation(361), we used these results to guide the construction of site specific variants that include 3-, 5-, 7-, and 9-sites of deamidation on HγS. The sites of mutagenesis of the 3-site variant were identified as the most abundantly deamidated (360). To mimic progressive deamidation, in each new variant the previous sites of mutagenesis were retained and two sites added based on both their quantified deamidation abundance in cataractous lenses and their solvent exposure (360).

The biophysical changes to β- and γ-crystallins caused by deamidation have been investigated by several groups, with variants formed through site-specific mutations of Asn to Asp or Gln to Glu. Deamidation increases the total negative charge of the protein, which may alter surface properties that are important for mediating protein-protein interactions (362) or intramolecular interactions that stabilize protein folds. The newly-formed carboxylic acid has been shown to propagate PTMs through isomerization and truncation after nucleophilic attack of the backbone amide(135). Deamidation of β- and γ-crystallins has been shown to increase aggregation propensity, decrease stability, and alter protein dynamics(151; 108; 363; 364). In β-crystallins, deamidation has been shown to alter the oligomeric tendencies of these proteins (365). However, some authors argue the addition of single or multiple sites of deamidation show no consequential alteration to the stability or aggregation propensity of these proteins (105; 366).

This work builds on a previous investigation where Norton-Baker et al. produced crystal structures of the 3-, 5-, 7-, and 9-site variants that reveal the overall fold was minimally changed, but the propensity to oxidize and aggregate increased with increasing deamidation (361). Here, we investigate the structural determinants of these altered biophysical properties. Specifically, we show that the overall 'slow' dynamics of each variant remains the same, suggesting this unlikely the cause of these changes. However, their resistance to chemical unfolding is altered, suggesting the protein is destabilized by the altered electrostatics at the

surface of the protein.

3.2 Experimental Section

3.2.1 Protein expression and purification

A detailed account of HγS and each deamidation variant construct development and implementation was reported in Norton-Baker et al. (361). Briefly, the construct, which includes a N-terminal His tag 6× and TEV cleavage sequence(ENLFQG), was cloned into a pET28a(+) vector (Novagene, Darmstadt, Germany). Transformed Rosetta (DE3) *E. coli* are induced using Studier's autoinduction protocol (283). Cultures are pelleted at 4,000 rpm for 30 m, resuspended in 10 mM HEPES, 200 mM NaCl, 10 mM β-mercaptoethanol buffer. Cells were lysed and clarified at 14,000 rpm for 45 m. The protein was isolated using nickel affinity chromatography (Cytiva HisTrap HP) and the His tag was removed using tobacco etch virus (TEV) protease (produced in-house). TEV was removed using a second round of nickel affinity chromatography. The protein was further purified using size exclusion chromatography (SEC) HiLoad 16/600 Superdex 75 pg (Cytiva).

3.2.2 Global hydrogen deuterium exchange

Samples were dialyzed into water, flash frozen, and lyophilized immediately after SEC. They were then resuspended in 10 mM HEPES, 200 mM NaCl, 0.05% azide, and 1 mM TCEP a day before use. Protein samples and the HDX buffer (20 mM $NaPO_4$, 2.5 mM TCEP, 1 mM EDTA, 150 mM NaCl, D_2O pD 7.2) were allowed to equilibrate to 25 °C for 1 h. Then, the 2 mg/mL protein samples were diluted 10-fold with HDX buffer (10 mM NaPi [pD 7.4], 1mM EDTA, 2.5 mM TCEP, and 150 mM NaCl in D2O) at 25 °C. After 10 s, 1 m, 10 m,

100 m, and 24 h, 50 μL of sample was removed, combined with 50 μL of quenching buffer (200 mM $NaPO_4$, 1 mM TCEP, pH 2.3), and flash frozen. Samples were stored at -80 ° or on dry ice. A phenyl column was placed in ice and allowed to equilibrate for 4 h. The 50 μL aliquots were thawed on ice for 5 min, mixed with 40 μL of pre-chilled water, and run on a Waters Xevo XS-QTof. Solvent A was 0.1% formic acid and solvent B was acetonitrile. A gradient of 0% to 97% B over 1.5 min then 97% B for 0.5 min and was run at 0.2 ml/min. Mass shift in deuterated samples was calculated by subtracting the weighted average from a single protonated charge state. The MassLynx MaxEnt1 software was used to deconvolute the spectra.

3.2.3 Chemical denaturation

Fifteen guanidinium chloride (GdnHCl) solutions ranging from 0.1–5.4 M were prepared from a stock of 6 M GdnHCl, 20 mM HEPES, 150 mM NaCl, pH 7.0. The concentrations of the resulting solutions were verified with refractive index measurements collected on an Abbe refractometer (C10 VEEGEE) (367). Protein samples in 20 mM HEPES pH 7.0, 150 mM NaCl, 0.05 % NaN_3 were prepared to 1 mg/mL. The protein samples were diluted 10-fold in the gdnHCl solutions and stored overnight. Samples were plated on Fluorotrac, 96-well, F-Bottom (Chimney Well) plates and excited with 280 nm light with a bandwidth of 5 nm. Fluorescence spectra from 310–390 nm with 2 nm steps and 5 nm bandwith were collected on a Spark fluorescence plate reader (Tecan, Switzerland). The same protocol was used for a series of urea solutions ranging from 0.1–8 M. The solutions were prepared fresh from 6 M Urea, 20 mM HEPES, 150 mM NaCl, pH 7.

3.2.4 Chemical denaturation unfolding analysis

The unfolding of HγSWT and the deamidation variants as a function of GdnHCl were modeled as a two-state equilibrium between the native state (N) and the unfolded state (U) (368; 369). Therefore, the fraction of the folded (f_N) and the fraction unfolded (f_U) are equal to 1. The fraction of the unfolded signal was calculated as:

$$f_u = \frac{S_{min} - S}{S_{min} - S_{max}}$$

where S_{min} and S_{max} is the minimum and maxiumum value of the 360/320 nm signal intensity, respectively. The midpoint of the unfolding curves were calculated using a Boltzmann function equation in Prism (GraphPad).

3.2.5 NMR sample preparation

The aforementioned Rosetta (DE3) cells were grown at 37 °C in 500 mL cultures until OD 1.2 then pelleted at 3,500 rpm, 20 °C. The supernatant was decanted and the pellet resuspended in minimal media containing glucose and ^{15}N ammonium chloride. After shaking for 1 h at 37 °C, the cells were induced with IPTG and allowed to grow for 48 h at 16 °C. The same purification scheme was used was for the natural abundance samples. Samples were prepared to 10 mg/mL in 10 mM HEPES, 50 mM NaCl, 1 mM DTT, 10% D_2O, 0.05% NaN_3, and 1 mM 2–2 dimethylsilapentane-5-sulfonic acid (DSS) for ^{1}H chemical shift referencing.

3.2.6 NMR spectroscopy

^{1}H-^{15}N NMR spectra were collected at 298 K on a Bruker Avance 600 MHz spectrometer equipped with a cryoprobe. NMR spectra were processed using Topspin. Chemical shift

perturbations were calculated by first referencing each spectrum to DSS at 0 ppm. Chemical shift assignment was performed by referencing to previous data collected by our group (BMRB: 17576) (110). Referencing allowed for unambiguous assignment of 85 % of the spectra. ^{1}H-^{15}N HSQC-TOCSY collected on an Avance Neo MHz High-Resolution NMR Console equipped with a ^{1}H(^{13}C/^{15}N) 5mm Tri-axis PFG Triple Resonance probe were used to assign all but five resonances. Assignments of HγS3, HγS5, HγS7, HγS9 were assigned by referencing to HγSWT, allowing for 99, 96, 96, and 88% of residues.

The chemical shift differences were calculated using:

$$\Delta\delta_{avg} = \sqrt{\frac{(\Delta\delta_N/5)^2 + (\Delta\delta_H)^2}{2}}$$

A significant difference in chemical shift was determined to be two× the root mean square (RMS) of the calculated CSP from HγS3 as compared to HγSWT.

3.3 Results and discussion

3.3.1 Chemical shift perturbations

To evaluate the subtle changes in structure that occur in each deamidation variant (Figure 3.1), we used ^{1}H-^{15}N HSQCs, which serve as a 'fingerprint' of the chemical environment of each backbone residue. Each backbone amide will have a peak on the ^{1}H-^{15}N HSQC that is designated by its ^{1}H and ^{15}N chemical shift. Therefore, chemical shift perturbations (CSPs) can be used an indication of structural rearrangement (Figure 3.2).

All of the deamidation variants show only minimal perturbation, with changes isolated to areas surrounding the mutation sites. These results are similar to those observed for other deamidation variants of HγS and its homolog human γD-crystallin, which show few to no

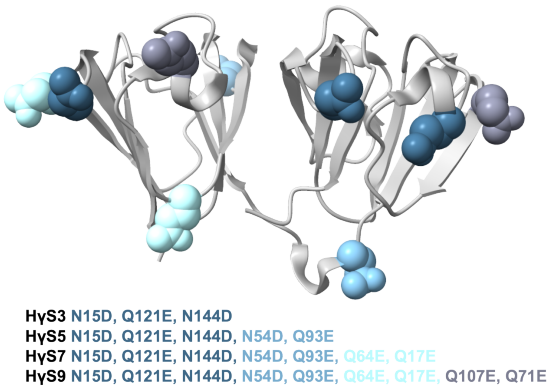

Figure 3.1: Ribbon representation of HγSWT with the sites of mutagenesis highlighted with space filling models.

CSPs > 0.5 ppm. Almost no significant change was seen in HγS3, except for Y70, which disappears from the HγS3 spectrum, suggesting the residue has shifted to an intermediate exchange regime in the deamidation variant. In HγS5, only residues that are sequentially close to the site of the mutations (R52, F55, G91, G92) were perturbed, except D29, which is on the adjacent β-sheet across the 'top' of HγS (Figure 3.3A). Similarly, mutation site D54N in HγS7 sits near the base of the first β-sheet nearby the charged residue E43 and perturbs it and a series of residues across the bottom of the first sheet (G5, K7, G44, and G45) (Figure 3.3B). The average chemical shift perturbation of HγS9 is greater than two times that of HγS3, which is likely an underestimation because 16 residues were perturbed so much it precluded their identification in HγS9.

It has been established that the main site for HγS intermolecular disulfide bonding is at residue C25 (361; 248). This residue is the central residue in a 'CXCXC' motif, which is designated the 'cysteine loop;. These results show that the cysteine loop of HγS3 - HγS9 retains on average a similar overall structure to that of HγSWT.

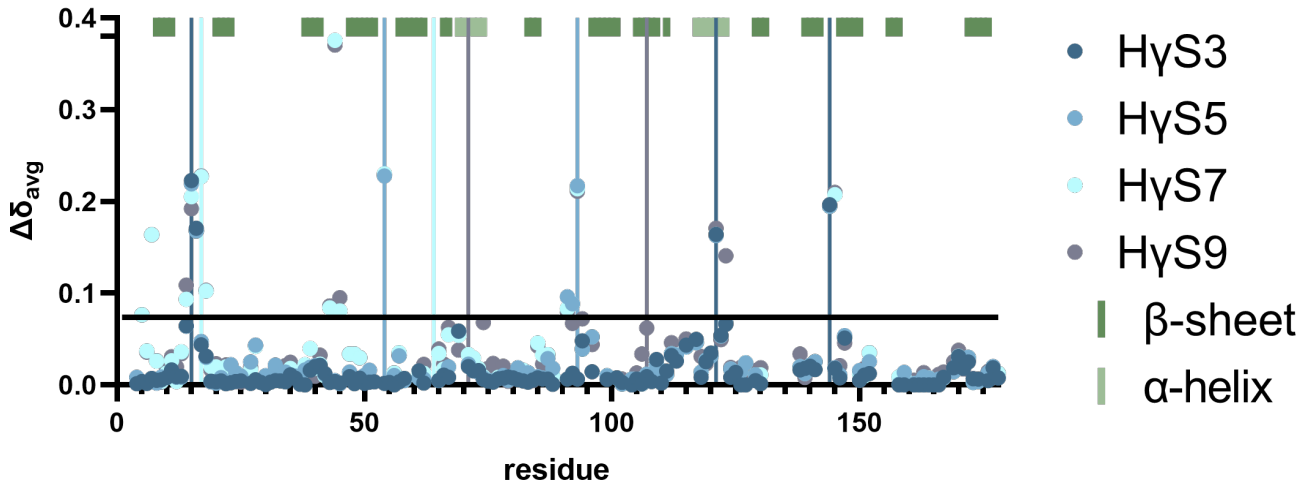

Figure 3.2: Chemical shift perturbations of each deamidation variant compared to HγSWT. Sites of deamidation are indicated with vertical lines. For reference, twice the RMS CSP of HγS3 to HγSWT is indicated by a horizontal black line. Dark and light green boxes indicate residues with β-sheet and α-helix secondary structure, respectively.

3.3.2 Hydrogen/deuterium exchange

We hypothesized that the increased propensity for oxidation in the deamidation variants was from altered dynamics. In this model, the crystallins would have increased flexibility allowing for increased opportunity for oxidative attack. To measure the dynamics of the variants we measured the hydrogen/deuterium exchange (HDX) using LC-MS/MS. At physiological pH, hydrogen/deuterium exchange at the backbone amide positions occurs primarily through the base catalyzed mechanism (Scheme 3.1). The rate of this exchange is, thus, dependent

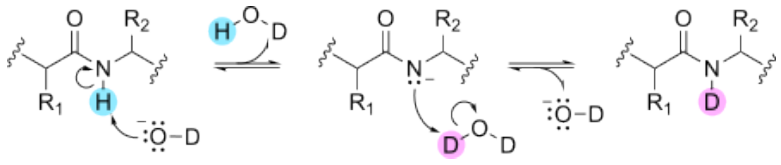

Scheme 3.1: Hydrogen/deuterium exchange base catalyzed mechanism

on the accessibility for an initial hydroxyl attack, which can be restricted by the presence of a hydrogen bond or solvent occlusion. If a protein is altered such that its dynamics are

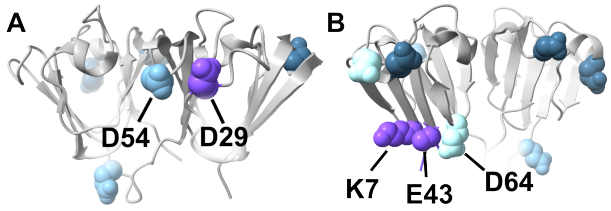

Figure 3.3: Site of perturbation in (A) HγS5 and (B) HγS7 highlighted on ribbon structures of their respective crystal structures (PDB: 7N38, 7N39).

increased, these restrictions will be weakened and isotope exchange will increase. The use of HDX-MS to probe protein dynamics has been thoroughly reviewed (370; 371; 372; 373).

Positions that are available for attack are defined as conformationally open and those unavailable as closed. Therefore, the hydrogen/deuterium exchange process is often described by the equation:

$$\mathrm{N{-}H_{cl}} \underset{k_{cl}}{\overset{k_{op}}{\rightleftharpoons}} \mathrm{N{-}H_{op}} \xrightarrow{k_{ch}} \mathrm{N{-}D_{op}} \underset{k_{op}}{\overset{k_{cl}}{\rightleftharpoons}} \mathrm{N{-}D_{cl}}$$

where the rates (k) of transitioning from closed to open conformations or vice-versa are indicated by 'cl' and 'op', respectively, and k_{ch} is referred to as the 'chemical exchange' rate (374). At high levels of deuterium (>90%), the conversion from protonated to deuterated is essentially irreversible. The difference in rates between k_{cl} and k_{ch} create two distinct kinetic regimes. The first is EX1 ($k_{ch} >> k_{cl}$), where the amide remains in the open conformation for much longer than the time it takes for isotope exchange to occur. This exchange regime is very uncommon and is often associated with allostery, where multiple events are required for the protein to move in and out of the confirmation. Proteins experiencing EX1 kinetics will have two distinct populations, open and closed, which will appear simultaneously on a mass spectrum as a heavier and lighter peak, respectively, and the intensity of these populations will shift over time. The second and more common kinetic regime is EX2 ($k_{ch} << k_{cl}$), where the amides are transiently in the open position and the rate at which they are deuterated is

a function of k_{op}, k_{cl}, and k_{ch}. Therefore, protein undergoing EX2 kinetics will appear as a 'single' population that gradually shifts in mass over time.

The observed rate of exchange for EX1 kinetics is:

$$k_{ex1} = k_{op}$$

and for EX2 kinetics is:

$$k_{ex2} = k_{op}/k_{cl} \cdot k_{ch}$$

If increased dynamics on this time-scale were the cause of increased oxidative attack, we would predict that the variants would have increased deuterium uptake with increasing deamidation. In order to test this hypothesis, the overall deuterium uptake of each deamidation variant was measured. My results show no significant difference between HγS3, HγS5, and HγS7, suggesting that the overall domain movements remain mostly unchanged between these deamidated variants (Figure **??**). The deconvoluted spectra of HγS3, HγS5, and HγS7 are shown in Figure B.1 and HγS9 and oxidized HγSWT in Figure B.2. The deuterium up-

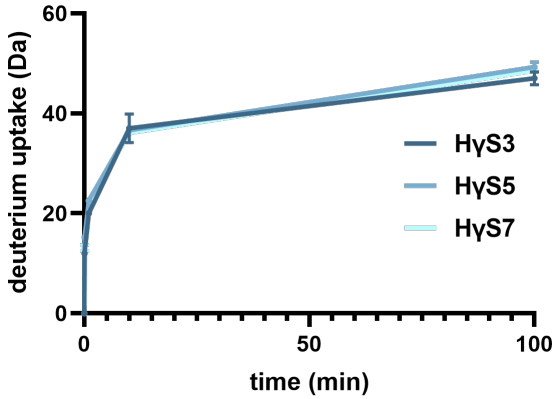

Figure 3.4: The mass average shift ofHγS3, HγS5, HγS7 as a function of time during hydrogen/deuterium exchange in 90% D_2O phosphate buffer at pD 7.4.

take of extensively oxidized HγSWT and non-oxidized HγS9 were also compared and showed

minimal change with a slight increase in the uptake of HγS9 (Figure 3.5). The deconvoluted mas Additionally, in all variants only a single mass envelope is present at each time point;

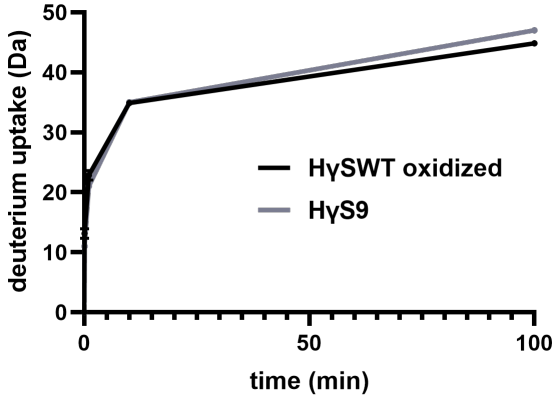

Figure 3.5: The mass average shift of HγS9 and oxidized HγSWT as a function of time during hydrogen/deuterium exchange in 90% D_2O phosphate buffer at pD 7.4.

therefore, there are unlikely to be distinct conformers present in each protein.

Previously, we showed the oxidation and dimerization increased with increasing deamidation on fresh samples. Without any significant differences between the slow dynamics of HγS3, HγS5, HγS7, the origins of these altered oxidation propensity does not appear to be from changes in slow dynamics. Furthermore, the highly similar slow dynamics of HγS9 and oxidized HγSWT suggests that this trend would not change with sample ageing. However, longer time points of HDX and assessment of HDX at the peptide level would be necessary to conclusive confirm these results.

3.3.3 Chemical Denaturation

To broaden our understanding of the effects of deamidation on HγS stability, I investigated the deamidation variants' unfolding as a function of two osmolytes – urea and guanidinium chloride (GdnHCl). Chemical denaturation has long been used as a tool for probing protein stability (375; 376; 377). It is well supported that GdnHCl is 2- 2.5 times more efficient at

denaturation than urea and their denaturation mechanisms differ.(368) It has been proposed that urea destabilizes proteins through the formation of hydrogen bonds with the backbone amides and that GdnHCl engages the protein through π-stacking and charge-charge interactions (378; 368). The differences of the unfolding mechanisms can be leveraged to determine the underlying factors of protein stability.(377; 379)

The degree of protein unfolding after exposure to each osmolyte was evaluated using fluorescence spectroscopy. HγS contain two tryptophans buried within each domain.When λ_{ex} 280 nm light the fluorescence spectra of HγSWT and variants have an λ_{max} peak maximum at ≈320 nm. As the protein unfolds and the tryptophans become exposed to the solvent and there is a redshift in the emission spectra that is indicative of tryptophans in a polar environment (Figure B.3) (297).

Samples (0.1 mg/mL) were incubated at room temperature overnight in GdnHCl concentrations that range from 0.1-5.4 M. Unfolding was evaluated at 30m, 1 h, 3 h, and overnight revealing no changes to the fluorescence spectra over this time span (data not shown). The midpoint of HγSWT of 2.5 and minimal perturbations as a function of deamidation is consistent with other literature results (380; 381; 150). For HγSWT and HγS3 the λ_{max} fluorescence intensity increases as the protein unfolds (Figure B.4). This is expected since quenching as a result of FRET between both pairs of tryptophans at the core of HγSWT reduces signal intensity (84). When the protein is unfolded the signal intensity increases. However, a loss of signal is observed for HγS5, HγS7, and HγS9. This could potentially be from aggregation of partially unfolded proteins.

Similarly, samples of each variant (0.1 mg/mL) were incubated at room temperature and measured at 2 h and 6 h in urea concentrations ranging from 1-8 M. Time points longer than this were not investigated because urea forms cyanate ions that can react with the protein and skew results at longer timepoints. After 2 h, the shift in λ_{max} increased with increasing deamidation, where HγSWT showed no signs of unfolding (Figure 3.6). After 6 h, HγSWT

remains only partially unfolded whereas HγS3 and HγS5 show near complete unfolding, and HγS7 and HγS9 are completely unfolded. Therefore, only HγS7 and HγS9 unfolding curves were analyzed (Figure 3.7).

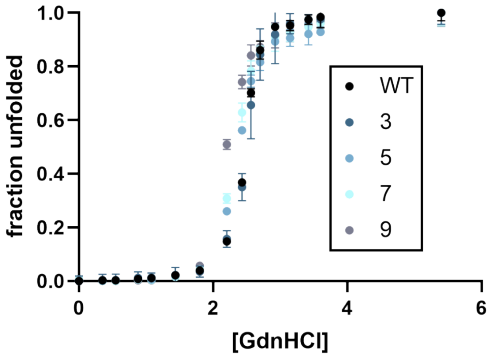

protein	midpoint (M GdnHCl)	m-value	R^2
HγSWT	2.473	0.1189	0.9978
HγS3	2.486	0.1303	0.9977
HγS5	2.363	0.1675	0.9979
HγS7	2.326	0.1698	0.9988
HγS9	2.198	0.1816	0.9981

Figure 3.6: Guanidinium chloride (GdnHCl) unfolding curves of HγSWT and deamidation variants.

We hypothesize that this pattern of unfolding – no change in response to GdnHCl but a change in urea response – suggests that the deamidated variants are destabilized by their electrostatic interactions to stabilize their folds. The rationale is that the high ionic strength of GdnHCl solutions masks the electrostatic intra- or intermolecular interactions, making them inconsequential to the stability.(382) However, urea denaturation would depend on the sum of the hydrophobic and electrostatic interactions(383). Therefore, the electrostatic interactions are slightly destabilizing to the protein.

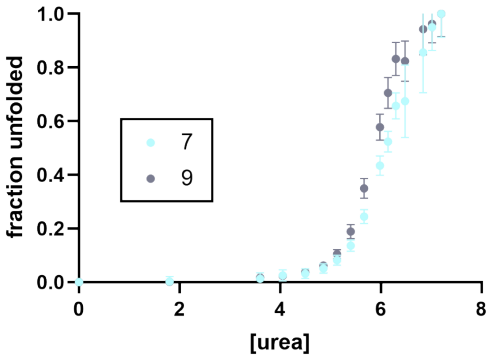

protein	midpoint (M urea)	m-value	R^2
HγS7	6.179	0.4293	0.9970
HγS9	5.875	0.3219	0.9980

Figure 3.7: Urea unfolding curves of HγSWT and deamidation variants.

3.4 Conclusion

Protein dynamics exist on several timescales ranging from ps- to hours. Dynamics on the ms to hours timescale are indicative of larger domain movements and these can be evaluated using HDX-MS (370; 371; 372; 373). We observed that the overall deuterium uptake of HγS deamidation variants remains highly similar suggesting there are unlikely significant differences in the slow dynamics of these variants. Deuterium uptake is highly dependent on both solvent accessibility and H-bonding structure. Therefore, even heavily solvent-exposed backbone amides can resist HDX if they are locked in secondary structures. All of the deamidation sites in HγS3 - HγS9 are on the surface of the protein. The lack of change in overall HDX patterns suggests that these variants are not weakening the surface secondary structure pattern. A 3-site variant that contained two of the same sites as HγS3 (N15D and N144D) and a buried mutation site in the N-terminal domain (N76D)(151) as well as a double mutant βB2-crystallin (384) also revealed minimal change in the global deuterium uptake. Collectively, these results suggest that it is unlikely that changes in slower motions are the cause of the increased aggregation propensity of these γ-crystallins.

All of the variants assessed here had similar unfolding midpoints when unfolded with GdnHCl, but were more susceptible to unfolding by urea. This suggests that the contributions to protein stability by hydrophobic properties are similar, but are destabilized by their electrostatic properties. Minimal perturbation in the unfolding midpoints of deamidation variants as a function of GdnHCl concentration has been frequently observed (380; 366; 151; 363). The N15D, N144D, N76D three site variant also showed minimal changes in the GdnHCl unfolding curve as compared to HγSWT, but revealed alternate unfolding intermediates when evaluated by HDX during denaturation (151). The inclusion of a buried residue may be the source of these altered intermediates since the single site N76D variant showed highly similar unfolding intermediates. A double mutant of HγSD with two residues buried in the interdomain interface shows a more dramatic appearance of alternate unfolding intermediates under GdnHCl conditions as the unfolding curves are best described as a three state transition rather than a two state unfolding model like the curves presented here (381).

Two γD variants (366), one which removed all the Asn residues in the N-terminal domain and the other all of the Asn residues in the C-terminal domain, as well as a HγS 2- and 4-site variant (380) revealed an increase in the attractiveness of their pairwise interactions. In contrast, Hγ3-9 previously revealed an increase in the repulsiveness of their pairwise interactions (361). I propose that this discrepancy comes from the inclusion of buried residues. The CSP values calculated here show that the residues most affected by the deamidation were charged residues and neighboring flexible residues which can potentially accommodate altered surface properties. We also showed the the electrostatic contribution to the protein may weaken the stability of the protein. Therefore, I propose that if deamidations at the surface HγSWT alter the biophysical properties through altered electrostatic interactions.

Bibliography

[1] S. Patel, J. Marshall, F. W. I. Fitzke **1995** *J. Cataract Refractive Surg. 11*, 100–105.

[2] W. Jagger **1992** *Vis. Res. 32*, 1271–1284.

[3] R. H. H. Kröger, M. C. W. Campbell, R. Munger, R. D. Fernald **1994** *Vis. Res. 34*, 1815–1822.

[4] L. F. Garner, G. T. Smith, S. Yao, R. C. Augusteyn **2001** *Vis. Res. 41*, 973–979.

[5] G. J. Wistow, J. Piatigorsky **1988** *Annu. Rev. Biochem. 57*, 479–504.

[6] C. Slingsby, G. J. Wistow, A. R. Clark **2013** *Protein Sci. 22*, 367–380.

[7] J. Horwitz, M. P. Bova, L.-L. Ding, D. A. Haley, P. L. Stewart **1999** *Eye 13*, 403–408.

[8] H. Bloemendal, W. de Jong, R. Jaenicke, N. H.Lubsen, C. Slingsby, A. Tardieu **2004** *Prog. Biophys. Mol. Biol. 86*, 407–485.

[9] World Health Organization **2020** "Priority Eye Diseases", can be found under https://www.who.int/blindness/causes/priority/en/index1.html.

[10] M. Delaye, A. Tardieu **1983** *Nature 302*, 415–417.

[11] A. Cvekl, R. McGreal, WeiLiu *Prog. Mol. Biol. Transl. Sci.*, vol. 134 **2015** Elsevier 129–167.

[12] A. Cvekl, Y. Zhao, R. McGreal, Q. Xie, X. Gu, D. Zheng **2017** *Genome Biol. Evol. 9*, 2075–2092.

[13] J. Piatigorsky **1984** *Cell 38*, 620.

[14] R. Jaenicke **1994** *Naturwissenschaften 81*, 423–429.

[15] J. Piatigorsky, G. Wistow **1991** *Science 252*, 1078–1079.

[16] T. Blundell, P. Lindley, L. Miller, D. Moss, C. Slingsby, I. Tickle, B. Turnell, G. Wistow **1981** *Nature 289*, 771–777.

[17] E. Pettersen, T. Goddard, C. Huang, G. Couch, D. Greenblatt, E. Meng, F. TE. **2004** *J. Comput. Chem. 25*, 1605–1612.

[18] G. Wistow **1993** *Trends Biochem. Sci. 18*, 301–306.

[19] G. D'Alessio **2002** *Eur. J. Biochem. 269*, 3122–3130.

[20] S. M. Shimeld, A. G. Purkiss, R. P. Dirks, O. A. Bateman, C. Slingsby, N. H. Lubsen **2005** *Curr. Biol. 15*, 1684–1689.

[21] S. K. Suman, A. Mishra, L. Yeramala, I. D. Rastogi, Y. Sharma **2013** *Biochemistry 52*, 9047–9058.

[22] N. Kozlyuk, S. Sengupta, J. C. Bierma, R. W. Martin **2016** *Biochemistry 55*, 6961–6968.

[23] D. Khago, J. C. Bierma, K. W. Roskamp, N. Kozlyuk, R. W. Martin **2018** *J. Phys.: Condens. Matter 30*, 435101.

[24] K. Riyahi, S. M. Shimeld **2007** *Comp. Biochem. Physiol., Part B: Biochem. Mol. Biol. 147*, 347–357.

[25] A. Mishra, B. Krishnan, S. S. Srivastava, Y. Sharma **2014** *Prog. Biophys. Mol. Biol. 115*, 42–51.

[26] A. Mishra, B. Krishnan, R. Raman, Y. Sharma **2016** *Biochim. Biophys. Acta, Gen. Subj. 1860*, 299–303.

[27] R. Jaenicke, C. Slingsby **2001** *Crit. Rev. Biochem. Mol. Biol. 36*, 435–499.

[28] C. N. Kingsley, W. D. Brubaker, S. Markovic, A. Diehl, A. J. Brindley, H. Oschkinat, R. W. Martin **2013** *Structure 21*, 2221–2227.

[29] M. A. Smith, O. A. Bateman, R. Jaenicke, C. Slingsby **2007** *Protein Sci. 16*, 615–625.

[30] Z. Wu, F. Delaglio, K. Wyatt, G. Wistow, A. Bax **2005** *Protein Sci. 14*, 3101–3114.

[31] V. Sagar, S. K. Chaturvedi, P. Schuck, G. Wistow **2017** *Structure 25*, 1068–1078.e2.

[32] B. Mahler, Y. Chen, J. Ford, C. Thiel, G. Wistow, Z. Wu **2013** *Biochemistry 52*, 3579–3587.

[33] H. Ebersbach, E. Fiedler, T. Scheuermann, M. Fiedler, M. T. Stubbs, C. Reimann, G. Proetzel, R. Rudolph, U. Fiedler **2007** *J. Mol. Biol. 372*, 172–185.

[34] K. Dixit, A. Pande, J. Pande, S. P. Sarma **2016** *Biochemistry 55*, 3136–3149.

[35] J. Wang, X. Zuo, P. Yu, I.-J. L. Byeon, J. Jung, X. Wang, M. Dyba, S. Seifert, C. D. Schwieters, J. Qin, A. M. Gronenborn, Y.-X. Wang **2009** *J. Am. Chem. Soc. 131*, 10507–10515.

[36] A. Basak, O. Bateman, C. Slingsby, A. Pande, N. Asherie, O. Ogun, G. B. Benedek, J. Pande **2003** *J. Mol. Biol. 328*, 1137–1147.

[37] Z. Xi, M. J. Whitley, A. M. Gronenborn **2017** *Structure 25*, 496–505.

[38] I. A. Mills-Henry, S. L. Thol, M. S. Kosinski-Collins, E. Serebryany, J. A. King **2019** *Biophys. J. 117*, 269–280.

[39] S. L. Flaugh, M. S. Kosinski-Collins, J. King **2005** *Protein Sci. 14*, 569–581.

[40] J. M. Hemmingsen, K. M. Gernert, J. S. Richardson, D. C. Richardson **1994** *Protein Sci. 3*, 1927–1937.

[41] F. Kong, J. King **2011** *Protein Sci. 20*, 513–528.

[42] E. Serebryany, J. A. King **2014** *Prog. Biophys. Mol. Biol. 115*, 32–41.

[43] K. Zhang, W.-J. Zhao, K. Yao, Y.-B. Yan **2019** *Biochemistry 58*, 2499–2508.

[44] P. Houston, N. Macro, M. Kang, L. Chen, J. Yang, L. Wang, Z. Wu, D. Zhong **2020** *J. Am. Chem. Soc. 142*, 3997–4007.

[45] K.-Y. Huang, C. N. Kingsley, R. Sheil, C.-Y. Cheng, J. C. Bierma, K. W. Roskamp, D. Khago, R. W. Martin, S. Han **2016** *J. Am. Chem. Soc. 138*, 5392–5402.

[46] R. W. Martin **2014** *eMagRes 3*, 139–152.

[47] S. Grutsch, S. Brüschweiler, M. Tollinger **2016** *PLoS Comput. Biol. 12*, e1004620.

[48] A. Sekhar, L. E. Kay **2019** *Annu. Rev. Biophys. 48*, 297–319.

[49] H. Arthanari, K. Takeuchi, A. Dubey, G. Wagner **2019** *Curr. Opin. Struct. Biol. 58*, 294–304.

[50] F. Ji, J. Jung, L. M. I. Koharudin, A. M. Gronenborn **2013** *J. Biol. Chem. 288*, 99–109.

[51] S. V. Bharat, A. Shekhtman, J. Pande **2014** *Biochem. Biophys. Res. Commun. 443*, 110–114.

[52] D. Khago, E. K. Wong, C. N. Kingsley, J. A. Freites, D. J. Tobias, R. W. Martin **2016** *Biochim. Biophys. Acta, Gen. Subj. 1860*, 325–332.

[53] M. A. Sprague-Piercy, E. Wong, K. W. Roskamp, J. N. Fakhoury, J. A. Freites, D. J. Tobias, R. W. Martin **2020** *Biochim. Biophys. Acta, Gen. Subj. 1864*, 129502.

[54] M. Sher, A. Hameed, S. Noreen, M. Fayyaz-ur-Rehman, M. A. Hussain, S. N. A. Bukhari **2015** *Analyst 140*, 6392–6397.

[55] L. Quintanar, J. A. Domínguez-Calva, E. Serebryany, L. Rivillas-Acevedo, C. Haase-Pettingell, C. Amero, J. A. King **2016** *ACS Chem. Biol. 11*, 263–272.

[56] J. C. Boatz, M. J. Whitley, M. Li, A. M. Gronenborn, P. C. van der Wel **2017** *Nat. Commun. 8*, 1–10.

[57] K. W. Roskamp, D. M. Montelongo, C. D. Anorma, D. N. Bandak, J. A. Chua, K. T. Malecha, R. W. Martin **2017** *Invest. Ophthalmol. Visual Sci. 58*, 2397–2405.

[58] K. W. Roskamp, S. Azim, G. Kassier, B. Norton-Baker, M. A. Sprague-Piercy, R. D. Miller, R. W. Martin **2020** *Biochemistry 59*, 2371–2385.

[59] T. O. Zhang, A. M. Alperstein, M. T. Zanni **2017** *J. Mol. Biol. 429*, 1705–1721.

[60] A. M. Alperstein, J. S. Ostrander, T. O. Zhang, M. T. Zanni **2019** *Proc. Natl. Acad. Sci. U. S. A. 116*, 6602–6607.

[61] A. R. Lam, S. Moran, N. K. Preketes, T. Zhang, M. T. Zanni, S. Mukamel **2013** *J. Phys. Chem. B 117*, 15436–15443.

[62] M. Chemerovski-Glikman, M. Mimouni, Y. Dagan, E. Haj, I. Vainer, R. Allon, E. Z. Blumenthal, L. Adler-Abramovich, D. Segal, E. Gazit, S. Zayit-Soudry **2018** *Sci. Rep. 8*, 9341.

[63] L. Zhao, X.-J. Chen, J. Zhu, Y.-B. Xi, X. Yang, L.-D. Hu, H. Ouyang, S. H. Patel, X. Jin, D. Lin, F. Wu, K. Flagg, H. Cai, G. Li, G. Cao, Y. Lin, D. Chen, C. Wen, C. Chung, Y. Wang, A. Qiu, E. Yeh, W. Wang, X. Hu, S. Grob, R. Abagyan, Z. Su, H. C. Tjondro, X.-J. Zhao, H. Luo, R. Hou, J. Jefferson, P. Perry, W. Gao, I. Kozak, D. Granet, Y. Li, X. Sun, J. Wang, L. Zhang, Y. Liu, Y.-B. Yan, K. Zhang **2015** *Nature 523*, 607–611.

[64] L. N. Makley, K. A. McMenimen, B. T. DeVree, J. W. Goldman, B. N. McGlasson, P. Rajagopal, B. M. Dunyak, T. J. McQuade, A. D. Thompson, R. Sunahara, R. E. Klevit, U. P. Andley, J. E. Gestwicki **2015** *Science 350*, 674–677.

[65] X.-J. Chen, L.-D. Hu, K. Yao, Y.-B. Yan **2018** *Biochem. Biophys. Res. Commun. 506*, 868–873.

[66] D. M. Daszynski, P. Santhoshkumar, A. S. Phadte, K. K. Sharma, H. A. Zhong, M. F. Lou, P. F. Kador **2019** *Sci. Rep. 9*, 8459.

[67] P. M. Shanmugam, A. Barigali, J. Kadaskar, S. Borgohain, D. K. C. Mishra, R. Ramanjulu, C. Minija **2015** *Indian J. Ophthalmol. 63*, 888–890.

[68] B. H. Meier, R. Riek, A. Böckmann **2017** *Trends Biochem. Sci. 42*, 777–787.

[69] P. C. van der Wel **2017** *Solid State Nucl. Magn. Reson. 88*, 1–14.

[70] C. P. Jaroniec **2019** *J. Magn. Reson. 306*, 42–47.

[71] R. W. Martin, J. E. Kelly, J. I. Kelz **2019** *J. Struct. Biol. 206*, 73–89.

[72] S. Jehle, P. Rajagopal, B. Bardiaux, S. Markovic, R. Kühne, J. R. Stout, V. A. Higman, R. E. Klevit, B.-J. van Rossum, H. Oschkinat **2010** *Nat. Struct. Mol. Biol. 17*, 1037–1042.

[73] T. L. S. Benzinger, D. M. Gregory, T. S. Burkoth, H. Miller-Auer, D. G. Lynn, R. E. Botto, S. C. Meredith **1998** *Proc. Natl. Acad. Sci. U. S. A. 95*, 13407–13412.

[74] B. Meier, R. Riek, A. Böckmann **2017** *Trends Biochem. Sci. 42*, 777–787.

[75] T. Lührs, C. Ritter, M. Adrian, D. Riek-Loher, B. Bohrmann, H. Döbeli, D. Schubert, R. Riek **2005** *Proc. Natl. Acad. Sci. U. S. A. 102*, 17342–17347.

[76] Y. Xiao, B. Ma, D. McElheny, S. Parthasarathy, F. Long, M. Hoshi, R. Nussinov, Y. Ishii **2015** *Nat. Struct. Mol. Biol. 22*, 499–505.

[77] M. T. Colvin, R. Silvers, Q. Z. Ni, T. V. Can, I. Sergeyev, M. Rosay, K. J. Donovan, B. Michael, J. Wall, S. Linse, *et al.* **2016** *J. Am. Chem. Soc. 138*, 9663–9674.

[78] A. Vandersteen, E. Hubin, R. Sarroukh, G. De Baets, J. Schymkowitz, F. Rousseau, V. Subramaniam, V. Raussens, H. Wenschuh, D. Wildemann, K. Broersen **2012** *FEBS Lett. 586*, 4088–4093.

[79] A. T. Petkova, W.-M. Yau, R. Tycko **2006** *Biochemistry 45*, 498–512.

[80] A. K. Paravastu, R. D. Leapman, W.-M. Yau, R. Tycko **2008** *Proc. Natl. Acad. Sci. U. S. A. 105*, 18349–18354.

[81] N. G. Sgourakis, W.-M. Yau, W. Qiang **2015** *Structure 23*, 216–227.

[82] R. Henderson **1995** *Q. Rev. Biophys. 28*, 171–193.

[83] N. Berova, K. Nakanishi, R. W. Woody. *Circ. Dichroism (2nd Ed.)*. John Wiley & Sons, Hoboken **2000**.

[84] J. Chen, P. R. Callis, J. King **2009** *Biochemistry 48*, 3708–3716.

[85] D. Some **2013** *Biophys. Rev. 5*, 147–158.

[86] E. Sahin, C. J. Roberts *Ther. Proteins* **2012** Springer 403–423.

[87] Y. Ma, D. M. Acosta, J. R. Whitney, R. Podgornik, N. F. Steinmetz, R. H. French, V. A. Parsegian **2015** *J. Biol. Phys. 41*, 85–97.

[88] D. Wu, H.-X. Zhou **2016** *Biophys. J. 110*, 43a.

[89] B. Neal, D. Asthagiri, A. Lenhoff **1998** *Biophys. J. 75*, 2469–2477.

[90] B. J. Berne, R. Pecora *Dynamic Light Scattering: With Applications to Chemistry, Biology, and Physics* **2000** Courier Corporation, Chelmsford.

[91] H. Naiki, K. Higuchi, M. Hosokawa, T. Takeda **1989** *Anal. Biochem. 177*, 244–249.

[92] R. Khurana, C. Coleman, C. Ionescu-Zanetti, S. A. Carter, V. Krishna, R. K. Grover, R. Roy, S. Singh **2005** *J. Struct. Biol. 151*, 229–238.

[93] C. Xue, T. Y. Lin, D. Chang, Z. Guo **2017** *R. Soc. Open Sci. 4*, 160696.

[94] M. Sebastiao, N. Quittot, S. Bourgault **2017** *Anal. Biochem. 532*, 83–86.

[95] Z. Qin, Y. Sun, B. Jia, D. Wang, Y. Ma, G. Ma **2017** *Langmuir 33*, 5398–5405.

[96] D. Matulis, R. Lovrien **1998** *Biophys. J. 74*, 422–429.

[97] A. Bothra, A. Bhattacharyya, C. Mukhopadhyay, K. Bhattacharyya, S. Roy **1998** *J. Biomol. Struct. Dyn. 15*, 959–966.

[98] W. N. Zagotta, M. T. Gordon, E. N. Senning, M. A. Munari, S. E. Gordon **2016** *J. Gen. Physiol. 147*, 201–216.

[99] J. W. Taraska, W. N. Zagotta **2010** *Neuron 66*, 170–189.

[100] V. P. R. Vendra, I. Khan, S. Chandani, A. Muniyandi, D. Balasubramanian **2016** *Biochim. Biophys. Acta, Gen. Subj 1860*, 333–343.

[101] J. Jung, I.-J. L. Byeon, Y. Wang, J. King, A. M. Gronenborn **2009** *Biochemistry 48*, 2597–2609.

[102] F. Ji, L. M. Koharudin, J. Jung, A. M. Gronenborn **2013** *Proteins: Struct., Funct., Bioinf. 81*, 1493–1498.

[103] F. Ji, J. Jung, A. M. Gronenborn **2012** *Biochemistry 51*, 2588–2596.

[104] M. J. Whitley, Z. Xi, J. C. Bartko, M. R. Jensen, M. Blackledge, A. M. Gronenborn **2017** *Biophys. J. 112*, 1135–1146.

[105] A. J. Guseman, M. J. Whitley, J. J. González, N. Rathi, M. Ambarian, A. M. Gronenborn **2020** *Structure* , 284–291.

[106] I. Khan, S. Chandani, D. Balasubramanian **2016** *Mol. Vision 22*, 771–782.

[107] K. J. Bari, S. Sharma, K. V. R. Chary **2019** *J. Struct. Biol. 205*, 72–78.

[108] H. M. Forsythe, C. J. Vetter, K. A. Jara, P. N. Reardon, L. L. David, E. J. Barbar, K. J. Lampi **2019** *Biochemistry 58*, 4112–4124.

[109] Z. Ma, G. Piszczek, P. T. Wingfield, Y. V. Sergeev, J. F. Hejtmancik **2009** *Biochemistry 48*, 7334–7341.

[110] W. D. Brubaker, J. A. Freites, K. J. Golchert, R. A. Shapiro, V. Morikis, D. J. Tobias, R. W. Martin **2011** *Biophys. J. 100*, 498–506.

[111] Y. He, J. Kang, J. Song **2020** *Biochem. Biophys. Res. Commun. 533*, 913–918.

[112] I. A. Mills, S. L. Flaugh, M. S. Kosinski-Collins, J. A. King **2007** *Protein Sci. 16*, 2427–2444.

[113] K. J. Bari, S. Sharma, K. V. R. Chary **2019** *Biochem. Biophys. Res. Commun. 517*, 499–506.

[114] K. J. Bari, S. Sharma, K. V. R. Chary **2019** *Biochem. Biophys. Res. Commun. 514*, 946–952.

[115] K. J. Bari, S. Sharma, K. V. R. Chary **2019** *Biochem. Biophys. Res. Commun. 511*, 679–684.

[116] S. Lee, B. Mahler, J. Toward, B. Jones, K. Wyatt, L. Dong, G. Wistow, Z. Wu **2010** *J. Mol. Biol. 399*, 320–330.

[117] T. Zhang, L. Yan, Y. Leng, C. Chen, L. Ma, Q. Wang, J. Zhang, L. Cao **2018** *Gene 675*, 9–14.

[118] K. J. Bari, S. Sharma, K. V. Chary **2018** *Biochem. Biophys. Res. Commun. 506*, 862–867.

[119] L. Acosta-Sampson, J. King **2010** *J. Mol. Biol. 401*, 134–152.

[120] K. L. Moreau, J. A. King **2012** *Trends Mol. Med. 18*, 273–282.

[121] W.-J. Zhao, J. Xu, X.-J. Chen, H.-H. Liu, K. Yao, Y.-B. Yan **2017** *Int. J. Biol. Macromol. 103*, 764–770.

[122] I.-K. Song, S. Na, E. Paek, K.-J. Lee **2020** *bioRxiv* , DOI: 10.1101/2020.05.26.116228.

[123] K. Zhang, W.-J. Zhao, X.-Y. Leng, S. Wang, K. Yao, Y.-B. Yan **2014** *Biochim. Biophys. Acta, Mol. Basis Dis. 1842*, 44–55.

[124] Y.-B. Xi, W.-J. Zhao, X.-T. Zuo, H. C. Tjondro, J. Li, A.-B. Dai, S. Wang, Y.-B. Yan **2014** *Biochim. Biophys. Acta, Mol. Basis Dis. 1842*, 2216–2229.

[125] X.-Y. Leng, H.-Y. Li, J. Wang, L.-B. Qi, Y.-B. Xi, Y.-B. Yan **2016** *Biochem. J. 473*, 2087–2096.

[126] M. P. Chan, M. Dolinska, Y. V. Sergeev, P. T. Wingfield, J. F. Hejtmancik **2008** *Biochemistry 47*, 11062–11069.

[127] Y. Sergeev, J. Hejtmancik, P. Wingfield **2004** *Biochemistry 43*, 415–424.

[128] C. Slingsby, O. Bateman **1990** *Biochemistry 29*, 6592–6599.

[129] L. Marín-Vinader, C. Onnekink, S. T. van Genesen, C. Slingsby, N. H. Lubsen **2006** *FEBS J. 273*, 3172–3182.

[130] K. Srivastava, R. Gupta, J. M. Chaves, O. P. Srivastava **2009** *Biochemistry 48*, 7179–7189.

[131] O. Bateman, R. Sarra, S. Van Genesen, G. Kappe, N. Lubsen, C. Slingsby **2003** *Exp. Eye Res. 77*, 409–422.

[132] W. Li, Q. Ji, Z. Wei, Y.-l. Chen, Z. Zhang, X. Yin, S. K. Aghmiuni, M. Liu, W. Chen, L. Shi, *et al.* **2019** *Exp. Eye Res. 186*, 107712.

[133] R. J. Truscott, M. G. Friedrich **2016** *Biochim. Biophys. Acta, Gen. Subj. 1860*, 192–198.

[134] O. P. Srivastava, K. Srivastava, J. M. Chaves, A. K. Gill **2017** *Biochem. Biophys. Rep. 10*, 94–131.

[135] T. Geiger, S. Clarke **1987** *J. Biol. Chem. 262*, 785–794.

[136] K. J. Reissner, D. W. Aswad **2003** *Cell. Mol. Life Sci. 60*, 1281–1295.

[137] M. M. Müller **2018** *Biochemistry 57*, 177–185.

[138] K. J. Lampi, Z. Ma, S. R. Hanson, M. Azuma, M. Shih, T. R. Shearer, D. L. Smith, J. B. Smith, L. L. David **1998** *Exp. Eye Res. 67*, 31–43.

[139] K. J. Lampi, P. A. Wilmarth, M. R. Murray, L. L. David **2014** *Prog. Biophys. Mol. Biol. 115*, 21–31.

[140] I. Kim, T. Saito, N. Fujii, T. Kanamoto, N. Fujii **2016** *Amino Acids 48*, 2855–2866.

[141] R. Warmack, H. Shawa, K. Liu, K. Lopez, J. Loo, J. Horwitz, S. Clarke **2019** *J. Biol. Chem. 294*, 12203–12219.

[142] Y. A. Lyon, M. P. Collier, D. L. Riggs, M. T. Degiacomi, J. L. P. Benesch, R. R. Julian **2019** *J. Biol. Chem. 294*, 7546–7555.

[143] A. J. Guseman, A. M. Gronenborn **2019** *J. Biol. Chem. 294*, 7556–7557.

[144] K. J. Lampi, J. T. Oxford, H. P. Bachinger, T. R. Shearer, L. L. David, D. M. Kapfer **2001** *Exp. Eye Res. 72*, 279–288.

[145] Y. H. Kim, D. M. Kapfer, J. Boekhorst, N. H. Lubsen, H. P. Bächinger, T. R. Shearer, L. L. David, J. B. Feix, K. J. Lampi **2002** *Biochemistry 41*, 14076–14084.

[146] K. J. Lampi, K. K. Amyx, P. Ahmann, E. A. Steel **2006** *Biochemistry 45*, 3146–3153.

[147] T. Takata, J. T. Oxford, B. Demeler, K. J. Lampi **2008** *Protein Sci. 17*, 1565–1575.

[148] K. J. Lampi, M. R. Murray, M. P. Peterson, B. S. Eng, E. Yue, A. R. Clark, E. Barbar, L. L. David **2016** *Biochim. Biophys. Acta, Gen. Subj 1860*, 304–314.

[149] A. Pande, N. Mokhor, J. Pande **2015** *Biochemistry 54*, 4890–4899.

[150] N. J. Ray, D. Hall, J. A. Carver **2016** *Biochimica et Biophysica Acta 1860*, 315–324.

[151] C. J. Vetter, D. C. Thorn, S. G. Wheeler, C. C. Mundorff, K. A. Halverson, T. E. Wales, U. P. Shinde, J. R. Engen, L. L. David, J. A. Carver **2020** *Protein Sci. 29*, 1945–1963.

[152] F. J. Giblin **2000** *J. Ocul. Pharmacol. Ther. 16*, 121–135.

[153] J. V. Fecondo, R. C. Augusteyn **1983** *Exp. Eye Res. 36*, 15–23.

[154] M. Wei, K.-Y. Xing, Y.-C. Fan, T. Libondi, M. F. Lou **2015** *Invest. Ophthalmol. Visual Sci. 56*, 598–605.

[155] P. G. Hains, R. J. Truscott **2007** *J. Proteome Res. 6*, 3935–3943.

[156] E. R. Stadtman **1992** *Science 257*, 1220–1224.

[157] R. J. Truscott **2005** *Exp. Eye Res. 80*, 709–725.

[158] I. Kim, T. Saito, N. Fujii, T. Kanamoto, T. Chatake, N. Fujii **2015** *Biochem. Biophys. Res. Commun. 466*, 622–628.

[159] S. Ramkumar, X. Fan, B. Wang, S. Yang, V. M. Monnier **2018** *Biochim. Biophys. Acta, Mol. Basis Dis. 1864*, 3595–3604.

[160] E. Serebryany, J. A. King **2015** *J. Biol. Chem. 290*, 11491–11503.

[161] J. Chen, S. L. Flaugh, P. R. Callis, J. King **2006** *Biochemistry 45*, 11552–11563.

[162] N. Schafheimer, J. King **2013** *Photochem. Photobiol. 89*, 1106–1115.

[163] B. Garner, K. Roberg, M. Qian, J. W. Eaton, R. J. Truscott **2000** *Exp. Eye Res. 71*, 599–607.

[164] S. Hajjari, R. Masoudi, S. Javadi, B. Hemmateenejad, R. Yousefi **2016** *Protein Pept. Lett. 23*, 78–86.

[165] W.-J. Zhao, Y.-B. Yan **2018** *Int. J. Biol. Macromol. 108*, 665–673.

[166] S. Cetinel, V. Semenchenko, J.-Y. Cho, M. G. Sharaf, K. F. Damji, L. D. Unsworth, C. Montemagno **2017** *PloS One 12*, e0177991.

[167] S. Chaudhury, I. Ghosh, G. Saha, S. Dasgupta **2015** *Int. J. Biol. Macromol. 77*, 287–292.

[168] S. Chaudhury, S. Bag, M. Bose, A. K. Das, A. K. Ghosh, S. Dasgupta **2016** *Mol. BioSyst. 12*, 2901–2909.

[169] S. Chaudhury, A. Dutta, S. Bag, P. Biswas, A. K. Das, S. Dasgupta **2018** *Spectrochim. Acta, Part A 192*, 318–327.

[170] S. Rana, K. S. Ghosh **2020** *Arch. Biochem. Biophys. 679*, 108204.

[171] S. Chaudhury, P. Roy, S. Dasgupta **2017** *Biochimie 137*, 46–55.

[172] K. K. Sharma, P. Santhoshkumar **2009** *Biochim. Biophys. Acta, Gen. Subj. 1790*, 1095–1108.

[173] P. Pereira, F. Shang, M. Hobbs, H. Girão, A. Taylor **2003** *Exp. Eye Res. 76*, 623–631.

[174] E. A. Whitcomb, F. Shang, A. Taylor **2013** *Invest. Ophthalmol. Visual Sci. 54*, ORSF31–ORSF36.

[175] M. H. J. Sweeney, R. J. W. Truscott **1998** *Exp. Eye Res. 67*, 587–595.

[176] A. Taylor, J. Jahngen-Hodge, L. L. Huang, P. Jacques **1991** *Age 14*, 65–71.

[177] B. A. Cobb, J. M. Petrash **2002** *Biochemistry 41*, 483–490.

[178] L. Mainali, W. J. O'Brien, R. Timsina **2020** *Curr. Eye Res.* , 185–194.

[179] S. Wang, W.-J. Zhao, H. Liu, H. Gong, Y.-B. Yan **2013** *Biochim. Biophys. Acta, Mol. Basis Dis. 1832*, 302–311.

[180] D. V. Wijerathne, S. Karabulut, J. W. Gauld **2024** *The Journal of Physical Chemistry B* .

[181] S. Catak, G. Monard, V. Aviyente, M. F. Ruiz-López **2008** *J. Phys. Chem. A 112*, 8752–8761.

[182] K. Aki, E. Okamura **2017** *J. Pept. Sci. 23*, 28–37.

[183] D. W. Aswad, M. V. Paranandi, B. T. Schurter **2000** *J. Pharm. Biomed. Anal. 21*, 1129–1136.

[184] J. L. Radkiewicz, H. Zipse, S. Clarke, K. N. Houk **2001** *J. Am. Chem. Soc. 123*, 3499 – 3506.

[185] S.-P. Su, B. Lyons, M. Friedrich, J. D. McArthur, X. Song, D. Xavier, R. J. W. Truscott, J. A. Aquilina **2012** *Aging Cell 11*, 1125–1127.

[186] B. Lyons, J. Jamie, T. R. W. **2014** *Amino Acids 46*, 199–207.

[187] M. G. Friedrich, Z. Wang, K. L. Schey, R. J. W. Truscott. **2019** *Biochem. J. 476*, 3817–3834.

[188] Z. Wang, M. G. Friedrich, R. J. W. Truscott, K. L. Schey **2019** *Biochim. Biophys. Acta, Proteins Proteomics 1867*, 831–839.

[189] H. J. Tweeddale, C. L. Hawkins, J. F. Janmie, R. J. Truscott, M. J. Davies **2016** *Free Radical Res. 50*, 1116–1130.

[190] A. M. Wood, R. J. Truscott **1993** *Exp. Eye Res. 56*, 317–325.

[191] L. M. Bova, M. H. Sweeney, J. F. Jamie, R. J. Truscott **2001** *Invest. Ophthalmol. Visual Sci. 42*, 200–205.

[192] H. Z. Malina, X. D. Martin **1996** *Graefe's Arch. Clin. Exp. Ophthalmol. 234*, 457–462.

[193] A. Chiarugi, E. Rapizzi, F. Moroni, F. Moroni **1999** *FEBS Lett. 453*, 197–200.

[194] N. R. Parker, J. F. Jamie, M. J. Davies, R. J. Truscott **2004** *Free Radic. Biol. Med. 37*, 1479–1489.

[195] J. Mizdrak, P. G. Hains, R. J. Truscott, J. F. Jamie, M. J. Davies **2008** *Free Radic. Biol. Med. 44*, 1108–1119.

[196] L. E. Goldstein, M. C. Leopold, X. Huang, C. S. Atwood, A. J. Saunders, M. Hartshorn, J. T. Lim, K. Y. Faget, J. A. Muffat, R. C. Scarpa, *et al.* **2000** *Biochemistry 39*, 7266–7275.

[197] Y. Chen, G. Reid, R. Simpson, R. Truscott **1997** *Exp. Eye Res. 65*, 835–840.

[198] A. D. Pawar, U. Kiran, R. Raman, S. Chandani, Y. Sharma **2019** *Biochem. Biophys. Res. Commun. 516*, 796e800.

[199] S. S. Srivastava, R. Raman, U. Kiran, R. Garg, S. Chadalawada, A. D. Pawar, R. Sankaranarayanan, Y. Sharma **2018** *Mol. Microbiol. 110*, 955–972.

[200] S. Ramakrishnan, K. Sulochana, T. Selvaraj, A. A. Rahim, M. Lakshmi, K. Arunagiri **1995** *Br. J. Ophthalmol. 79*, 202–206.

[201] O. Cekic **1998** *Br. J. Ophthalmol. 82*, 186–188.

[202] E. Aydin, T. Cumurcu, F. Özuĝurlu, H. Özyurt, S. Sahinoglu, D. Mendil, E. Hasdemir **2005** *Biol. Trace Elem. Res. 108*, 33–41.

[203] J. Dawczynski, M. Blum, K. Winnefeld, J. Strobel **2002** *Biol. Trace Elem. Res. 90*, 15–23.

[204] P. P. Fagerholm, B. T. Philipson, B. Lindström **1981** *Exp. Eye Res. 33*, 615–620.

[205] A. Langford-Smith, V. Tilakaratna, P. R. Lythgoe, S. J. Clark, P. N. Bishop, A. J. Day **2016** *PLoS One 11*, e0147576.

[206] J. A. Dominguez-Calva, C. Haase-Pettingell, E. Serebryany, J. A. King, L. Quintanar **2018** *Biochemistry 57*, 4959–4962.

[207] K. W. Roskamp, N. Kozlyuk, S. Sengupta, J. C. Bierma, R. W. Martin **2019** *Biochemistry 58*, 4505–4518.

[208] J. Dominguez-Calva, M. Perez-Vazquez, E. Serebryany, J. King, L. Quintanar **2018** *JBIC, J. Biol. Inorg. Chem. 23*, 1105–1118.

[209] R. Karunakaran, P. S. Srikumar **2018** *Mol. Cell. Biochem. 449*, 55–62.

[210] E. K. Wong, V. Prytkova, J. A. Freites, C. T. Butts, D. J. Tobias **2019** *Biochemistry 58*, 3691–3699.

[211] C. J. O'Brien, M. A. Blanco, J. A. Costanzo, M. Enterline, E. J. Fernandez, A. S. Robinson, C. J. Roberts **2016** *Protein Eng., Des. Sel. 29*, 231–243.

[212] C.-K. Chang, S. S.-S. Wang, C.-H. Lo, H.-C. Hsiao, J. W. Wu **2017** *J. Biomol. Struct. Dyn. 35*, 1042–1054.

[213] S. Zhu, X.-B. Xi, T.-L. Duan, Y. Zhai, J. Li, Y.-B. Yan, K. Yao **2018** *Int. J. Biol. Macromol. 117*, 807–814.

[214] C. W. Wahle, K. M. Martini, D. M. Hollenbeck, A. Langner, D. S. Ross, J. F. Hamilton, G. M. Thurston **2017** *Phys. Rev. E. 96*, 032415.

[215] S. D. Moran, T. O. Zhang, M. T. Zanni **2014** *Protein Sci. 23*, 321–331.

[216] V. Paviani, P. J. de Melo, A. Avakin, P. D. Mascio, G. E. Ronsein, O. Augusto **2020** *Free Radic. Biol. Med. 160*, 356–367.

[217] M. J. Bennett, M. P. Schlunegger, D. Eisenberg **1995** *Protein Sci. 4*, 2455–2468.

[218] N. M. Mascarenhas, S. Gosavi **2017** *Prog. Biophys. Mol. Biol. 128*, 113–120.

[219] S. Garcia-Manyes, D. Giganti, C. L. Badilla, A. Lezamiz, J. Perales-Calvo, A. E. Beedle, J. M. Fernández **2016** *J. Biol. Chem. 291*, 4226–4235.

[220] P. Das, J. A. King, R. Zhou **2011** *Proc. Natl. Acad. Sci. U. S. A. 108*, 10514–10519.

[221] E. Serebryany, T. Takata, E. Erickson, N. Schafheimer, Y. Wang, J. A. King **2016** *Protein Sci. 25*, 1115–1128.

[222] E. Serebryany, J. C. Woodard, B. V. Adkar, M. Shabab, J. A. King, E. I. Shakhnovich **2016** *J. Biol. Chem. 291*, 19172–19183.

[223] E. Serebryany, S. Yu, S. A. Trauger, B. Budnik, E. I. Shakhnovich **2018** *J. Biol. Chem. 293*, 17997–18009.

[224] O. B. Oka, H. Y. Yeoh, N. J. Bulleid **2015** *Biochem. J. 469*, 279–288.

[225] K. J. Woycechowsky, R. T. Raines **2003** *Biochemistry 42*, 5387–5394.

[226] E. Gross, C. S. Sevier, A. Vala, C. A. Kaiser, D. Fass **2002** *Nat. Struct. Biol. 9*, 61–67.

[227] U. Jakob, W. Muse, M. Eser, J. C. Bardwell **1999** *Cell 96*, 341–352.

[228] A. A. Hyman, C. A. Weber, F. Jülicher **2014** *Annu. Rev. Cell Dev. Biol. 30*, 39–58.

[229] S. Alberti, A. Gladfelter, T. Mittag **2019** *Cell 176*, 419–434.

[230] Z. Feng, X. Chen, X. Wu, M. Zhang **2019** *J. Biol. Chem. 294*, 14823–14835.

[231] G. L. Dignon, W. Zheng, Y. C. Kim, J. Mittal **2019** *ACS Cent. Sci. 5*, 821–830.

[232] G. B. Benedek, J. I. Clark, E. N. Serrallach, C. Y. Young, L. Mengel, T. Sauke, A. Bagg, K. Benedek **1979** *Philos. Trans. R. Soc., A 293*, 329–340.

[233] M. Delaye, J. I. Clark, G. B. Benedek **1982** *Biophys. J. 37*, 647–656.

[234] R. J. Siezen, M. R. Fisch, C. Slingsby, G. B. Benedek **1985** *Proc. Natl. Acad. Sci. U. S. A. 82*, 1701–1705.

[235] G. M. Thurston **2006** *J. Chem. Phys. 124*, 134909.

[236] A. J. Kiss, C.-H. C. Cheng **2008** *Comp. Biochem. Physiol., Part D: Genomics Proteomics 3*, 155–171.

[237] A. J. Kiss, A. Y. Mirarefi, S. Ramakrishnan, C. F. Zukoski, A. L. DeVries, C.-H. C. Cheng **2004** *J. Exp. Biol. 207*, 4633–4649.

[238] J. C. Bierma, K. W. Roskamp, A. P. Ledray, A. J. Kiss, C.-H. C. Cheng, R. W. Martin **2018** *J. Mol. Biol. 430*, 5151–5168.

[239] A. Mizuno, Y. Ozaki, K. Itoh, S. Matsushima, K. Iriyama **1984** *Biochem. Biophys. Res. Commun. 119*, 989–994.

[240] P. H. Yancey **2005** *J. Exp. Biol. 208*, 2819–2830.

[241] S. Cinar, H. Cinar, H. S. Chan, R. Winter **2019** *J. Am. Chem. Soc. 141*, 7347–7354.

[242] I. R. Kleckner, M. P. Foster **2011** *Biochimica et Biophysica Acta (BBA)-Proteins and Proteomics 1814*, 942–968.

[243] J. P. Lomont, J. S. Ostrander, J.-J. Ho, M. K. Petti, M. T. Zanni **2017** *J. Phys. Chem. B 121*, 8935–8945.

[244] L. E. Buchanan, M. Maj, E. B. Dunkelberger, P.-N. Cheng, J. S. Nowick, M. T. Zanni **2018** *Biochemistry 57*, 6470–6478.

[245] J. P. Lomont, K. L. Rich, M. Maj, J.-J. Ho, J. S. Ostrander, M. T. Zanni **2018** *J. Phys. Chem. B 122*, 144–153.

[246] G. Grazioli, Y. Yu, M. H. Unhelkar, R. W. Martin, C. T. Butts **2019** *The J. Phys. Chem. B 123*, 5452–5462.

[247] Y. Yu, G. Grazioli, M. H. Unhelkar, R. Martin, C. T. Butts **2020** *Sci. Rep. 10*, 15668.

[248] D. C. Thorn, A. B. Grosas, P. D. Mabbitt, N. J. Ray, C. J. Jackson, J. A. Carver **2019** *J. Mol. Biol. 431*, 483–497.

[249] D. Ben-Amotz **2015** *J. Phys. Chem. Lett. 6*, 1696–1701.

[250] J. Davis, K. Gierszal, P. Wang, D. Ben-Amotz **2012** *Nature 491*, 582–585.

[251] P. N. Perera, K. R. Fega, C. Lawrence, E. Sundstrom, J. Tomlinson-Phillips, D. Ben-Amotz **2009** *Proc. Natl. Acad. Sci. U. S. A. 106*, 12230–12234.

[252] K. Gierszal, J. Davis, M. Hands, W. D.S., L. Slipchenko, D. Ben-Amotz **2011** *J. Phys. Chem. Lett. 2*, 2930–2933.

[253] E. W. Knapp, I. Muegge **1993** *J. Phys. Chem. 97*, 11339–11343.

[254] R. Barnes, S. Sun, Y. Fichou, F. Dahlquist, M. Heyden, S. Han **2017** *J. Am. Chem. Soc. 139*, 17890–17901.

[255] D. P. Kharakoz, A. P. Sarvazyan **1993** *Biopolymers 33*, 11–26.

[256] P. Ball **2008** *Chem. Rev. 108*, 74–108.

[257] F. A. Tezcan, B. R. Crane, J. R. Winkler, H. B. Gray **2001** *Proc. Natl. Acad. Sci. U. S. A. 98*, 5002–5006.

[258] F. Hecker, J. Stubbe, M. Bennati **2021** *J. Am. Chem. Soc. 143*, 7237–7241.

[259] J. A. LaVerne **2000** *Radiat. Res. 153*, 196–200.

[260] D. Ghosal, M. Omelchenko, E. Gaidamakova, M. V.Y., A. Vasilenko, A. Venkateswaran, M. Zhai, H. Kostandarithes, H. Brim, K. Makarova **2005** *FEMS Microbiol. Rev. 29*, 361–375.

[261] J. Du, J. M. Gebicki **2004** *Int. J. Biochem. Cell Biol. 36*, 2334–2343.

[262] M. Davies, S. Fu, R. T. Dean **1995** *Biochem. J. 305*, 643–649.

[263] C. K. Robinson, K. Webb, A. Kaur, P. Jaruga, M. Dizdaroglu, N. S. Baliga, A. Place, J. Diruggiero **2011** *J. Bacteriol. 193*, 1653–1662.

[264] A.-C. Munteanu, V. Uivarosi, A. Andries **2015** *Extremophiles 9*, 707–719.

[265] S. K. Shukla, A. K. Sharma, S. Bajaj, M. Yashavarddhan **2021** *Drug Discovery Today 26*, 525–531.

[266] R. M. Lipman, B. J. Tripathi, R. C. Tripathi **1988** *Surv. Ophthalmol. 33*, 200–210.

[267] M.-O. Bernier, N. Journy, D. Villoing, M. M. Doody, B. H. Alexander, M. S. Linet, C. M. Kitahara **2018** *Radiology 286*, 592–601.

[268] L. T. Chylack Jr, L. E. Peterson, A. H. Feiveson, M. L. Wear, F. K. Manuel, W. H. Tung, D. S. Hardy, L. J. Marak, F. A. Cucinotta **2009** *Radiat. Res. 172*, 10–20.

[269] E. Nakashima, K. Neriishi, A. Minamoto **2006** *Health Phys. 90*, 154–160.

[270] K. Neriishi, E. Nakashima, A. Minamoto, S. Fujiwara, M. Akahoshi, H. K. Mishima, T. Kitaoka, R. E. Shore **2007** *Radiat. Res. 168*, 404–408.

[271] G. P. Hammer, U. Scheidemann-Wesp, F. Samkange-Zeeb, H. Wicke, K. Neriishi, M. Blettner **2013** *Radiat. Environ. Biophys. 52*, 303–319.

[272] N. Hamada, Y. Fujimichi, T. Iwasaki, N. Fujii, M. Furuhashi, E. Kubo, T. Minamino, T. Nomura, H. Sato **2014** *J. Radiat. Res. 55*, 831–846.

[273] S. Cornacchia, R. Errico, L. La Tegola, A. Maldera, G. Simeone, V. Fusco, A. Niccoli-Asabella, G. Rubini, G. Guglielmi **2019** *La Radiologia Medica 124*, 728–735.

[274] S. Ramkumar, N. Fujii, N. Fujii, B. Thankappan, H. Sakaue, K. Ingu, K. Natarajaseenivasan, K. Anbarasu **2014** *Mol. Vision 20*, 1002.

[275] W. M. Ross, M. O. Creighton, W. R. Inch, J. R. Trevithick **1983** *Exp. Eye Res. 36*, 645–653.

[276] W. M. Ross, M. O. Creighton, J. R. Trevithick **1990** *Scanning Microsc. 4*, 13.

[277] S. Taysi, R. Memisogullari, M. Koc, A. T. Yazici, M. Aslankurt, K. Gumustekin, B. Al, F. Ozabacigil, A. Yilmaz, H. Tahsin Ozder **2008** *Int. J. Radiat. Biol. 84*, 803–808.

[278] H. Morishita, T. Eguchi, S. Tsukamoto, Y. Sakamaki, S. Takahashi, C. Saito, I. Koyama-Honda, N. Mizushima **2021** *Nature 592*, 634–638.

[279] S. Bassnett **2009** *Exp. Eye Res. 88*, 133–139.

[280] P. Wilmarth, S. Tanner, S. Dasari, S. Nagalla, M. Riviere, V. Bafna, P. Pevzner, L. David **2006** *J. Proteome Res. 5*, 2554–2566.

[281] V. Harrington, S. McCall, S. Huynh, K. Srivastava, O. P. Srivastava **2004** *Mol. Vision 10*, 476–489.

[282] J. Chen, D. Toptygin, L. Brand, J. King **2008** *Biochemistry 47*, 10705–10721.

[283] F. W. Studier **2005** *Protein Expression Purif. 41*, 207–234.

[284] R. Ngelale, C. Lee, S. Bustillos, M. Nilsson **2019** *Solvent Extr. Ion Exch. 37*, 38–52.

[285] C. C. Perry, J. Ramos-Méndez, J. R. Milligan **2021** *Biomacromolecules 22*, 1675–1684.

[286] H. Fricke, S. Morse **1927** *Am. J. Roentgenol., Radium Ther. Nucl. Med. 18*, 430–432.

[287] R. Meesat, S. Sanguanmith, J. Meesungnoen, M. Lepage, A. Khalil, J.-P. Jay-Gerin **2012** *Radiat. Res. 177*, 813–826.

[288] G. L. Ellman **1959** *Arch. Biochem. Biophys. 82*, 70–77.

[289] P. W. Riddles, R. L. Blakeley, B. Zerner **1979** *Anal. Biochem. 94*, 75–81.

[290] A. Miles, R. W. Janes, B. A. Wallace **2021** *Chem. Soc. Rev. 50*, 8400–8413.

[291] A. Pande, J. Pande, N. Asherie, A. Lomakin, O. Ogun, J. King, G. B. Benedek **2001** *Proc. Natl. Acad. Sci. U. S. A. 98*, 6116–6120.

[292] K. Mandal, B. Chakrabarti, J. Thomson, R. Siezen **1987** *J. Biol. Chem. 262*, 8096–8102.

[293] S. S.-S. Wang, W.-S. Wen **2010** *Mol. Vision 16*, 2777.

[294] N. Fujii, T. Nakamura, Y. Sadakane, T. Saito, N. Fujii **2007** *Biochim. Biophys. Acta, Proteins Proteomics 1774*, 345–350.

[295] A. Vallée-Bélisle, S. W. Michnick **2012** *Nat. Struct. Mol. Biol. 19*, 731–736.

[296] Y. Fukunaga, Y. Katsuragi, T. Izumi, F. Sakiyama **1982** *J. Biochem. 92*, 129–141.

[297] M. S. Kosinski-Collins, S. L. Flaugh, J. King **2004** *Protein Sci. 13*, 2223–2235.

[298] M. Linetsky, B. Ortwerth **1997** *Photochem. Photobiol. 65*, 522–529.

[299] S. Zigman **1996** *Optom. and Vis. Sci. 3*, 182.

[300] J. M. Gutteridge, S. Wilkins **1983** *Biochim. Biophys. Acta, Gen. Subj. 759*, 38–41.

[301] B. Halliwell, J. M. Gutteridge **1990** *Arch. Biochem. Biophys. 280*, 1–8.

[302] M. R. Gunther, P. M. Hanna, R. P. Mason, M. S. Cohen **1995** *Arch. Biochem. Biophys. 316*, 515–522.

[303] K. J. Barnham, C. L. Masters, A. I. Bush **2004** *Nat. Rev. Drug Discovery 3*, 205–214.

[304] P. G. Hains, R. J. Truscott **2008** *Biochim. Biophys. Acta, Proteins and Proteomics 1784*, 1959–1964.

[305] L. J. Alcock, M. V. Perkins, J. M. Chalker **2018** *RIC Reviews 47*, 231–268.

[306] R. T. Dean, S. FU, R. Socker, M. J. Davies **1997** *Biochem. J. 324*, 1–18.

[307] M. J. Davies **2016** *Biochem. J. 473*, 805–825.

[308] K. Uchida **2003** *Amino Acids 25*, 249–257.

[309] S. H. Yong, M. Karel **1978** *Lipids 13*, 1–5.

[310] E. R. Stadtman, R. L. Levine. *Redox proteomics: from protein modifications to cellular dysfunction and diseases* vol. 9. John Wiley & Sons Hoboken NJ **2006**.

[311] G. Xu, M. R. Chance **2007** *Chemical reviews 107*, 3514–3543.

[312] G. Xu, K. Takamoto, M. R. Chance **2003** *Anal. Chem. 75*, 6995–7007.

[313] D. T. Johnson, L. H. Di Stefano, L. M. Jones **2019** *J. Biol. Chem. 294*, 11969–11979.

[314] H. Zhang, B. C. Gau, L. M. Jones, I. Vidavsky, M. L. Gross **2011** *Anal. Chem. 83*, 311–318.

[315] L. M. Jones, J. B. Sperry, J. A. Carroll, M. L. Gross **2011** *Anal. Chem. 83*, 7657–7661.

[316] A. S. Woods, H.-Y. J. Wang, S. N. Jackson **2007** *J. Proteome Res. 6*, 1176–1182.

[317] K. F. Medzihradszky, Z. Darula, E. Perlson, M. Fainzilber, R. J. Chalkley, H. Ball, D. Greenbaum, M. Bogyo, D. R. Tyson, R. A. Bradshaw, A. L. Burlingame **2004** *Mol. Cell. Proteomics 3*, 429–440.

[318] N. Fujii, H. Uchida, T. Saito **2004** *Mol. Vision 10*, 814–820.

[319] N. Fujii, K. Hiroki, S. Matsumoto, K. Masuda, M. Inoue, Y. Tanaka, M. Awakura, M. Akaboshi **2001** *Photochemistry and Photobiology 74*, 477–482.

[320] H.-J. Kim, S. Ha, H. Y. Lee, K.-J. Lee **2015** *Mass spectrometry reviews 34*, 184–208.

[321] S. Gebicki, J. M. .Gebicki **1993** *Biochem. J. 289*, 743–749.

[322] J. C. Lakbub, J. T. Shipman, H. Desaire **2018** *Anal. Bioanal. Chem. 410*, 2467–2484.

[323] J. R. Requena, C.-C. Chao, R. L. Levine, E. R. Stadtman **2001** *Proc. Natl. Acad. Sci. U. S. A. 98*, 69–74.

[324] X. Fan, J. Zhang, M. Theves, C. Strauch, I. Nemet, X. Liu, J. Qian, F. J. Giblin, V. M. Monnier **2009** *J. Biol. Chem. 284*, 34618–34627.

[325] J. S. Sharp, K. B. Tomer **2006** *Anal. Chem. 78*, 4885–4893.

[326] M. J. Davies, R. J. Truscott **2001** *J. Photochem. Photobiol., B 63*, 114–125.

[327] M. J. Davies **2003** *Biochem. Biophys. Res. Commun. 305*, 761–770.

[328] E. L. Finley, M. Busman, J. Dillon, R. K. Crouch, K. L. Schey **1997** *Photochem. Photobiol. 66*, 635–641.

[329] N. Schafheimer, Z. Wang, K. Schey, J. King **2014** *Biochemistry 53*, 979–990.

[330] A. E. Segneanu, I. Gozescu, A. Dabici, P. Sfirloaga, Z. Szabadai. *Organic compounds FT-IR spectroscopy* vol. 145. InTechOpen, Rijeka **2012**.

[331] A. Amici, R. Levine, L. Tsai, E. Stadtman **1989** *J. Biol. Chem. 264*, 3341–3346.

[332] J. Moskovitz, D. B. Oien **2010** *Antioxid. Redox Signaling 12*, 405–415.

[333] Y. Liu, T. Asset, Y. Chen, E. Murphy, E. O. Potma, I. Matanovic, D. A. Fishman, P. Atanassov **2020** *iScience 23*, 101757.

[334] D. Zhang, Y. Xie, M. F. Mrozek, C. Ortiz, V. J. Davisson, D. Ben-Amotz **2003** *Anal. Chem. 75*, 5703–5709.

[335] H. M. Zbikowska, P. Nowak, B. Wachowicz **2006** *Free Radical Biol. Med. 40*, 536–542.

[336] B. Sjöberg, S. Foley, B. Cardey, M. Fromm, M. Enescu **2018** *J. Photochem. Photobiol., B 188*, 95–99.

[337] K. L. Schey, Z. Wang, M. Friedrich, R. J. Truscott **2021** *Exp. Eye Res.* , 108679.

[338] M. G. Friedrich, Z. Wang, K. L. Schey, R. J. Truscott **2018** *Biochem. J. 475*, 3189–3200.

[339] C. Giulivi, N. Traaseth, K. Davies **2003** *Amino Acids 25*, 227–232.

[340] M. G. Friedrich, Z. Wang, K. L. Schey, R. J. Truscott **2021** *ACS Chem. Biol. 16*, 2244–2254.

[341] J. W. Heinecke, W. Li, G. A. Francis, J. A. Goldstein **1993** *J. Clin. Invest. 91*, 2866–2872.

[342] J. D. Steinmetz, R. R. Bourne, P. S. Briant, S. R. Flaxman, H. R. Taylor, J. B. Jonas, A. A. Abdoli, W. A. Abrha, A. Abualhasan, E. G. Abu-Gharbieh, *et al.* **2021** *The Lancet Global Health 9*, e144–e160.

[343] X. Fan, V. M. Monnier, J. Whitson **2017** *Experimental eye research 156*, 103–111.

[344] B. Kisic, D. Miric, L. Zoric, A. Ilic, I. Dragojevic **2012** *Oxidative medicine and cellular longevity 2012*, 467130.

[345] H. Abdelkader, R. G. Alany, B. Pierscionek **2015** *Journal of Pharmacy and Pharmacology 67*, 537–550.

[346] M. McFall-Ngai, L.-L. Ding, L. Takemoto, J. Horwitz **1985** *Experimental eye research 41*, 745–758.

[347] S. R. Hanson, A. Hasan, D. L. Smith, J. B. Smith **2000** *Exp. Eye Res. 71*, 195–207.

[348] K. Patel, R. T. Borchardt **1990** *Pharmaceutical research 7*, 703–711.

[349] D. L. Riggs, J. W. Silzel, Y. A. Lyon, A. S. Kang, R. R. Julian **2019** *Analytical chemistry 91*, 13032–13038.

[350] S. S. Adav, X. Gallart-Palau, K. H. Tan, S. K. Lim, J. P. Tam, S. K. Sze **2016** *Molecular brain 9*, 1–10.

[351] H. Lindner, W. Helliger **2001** *Experimental gerontology 36*, 1551–1563.

[352] M. G. Friedrich, S. E. Hancock, M. J. Raftery, R. J. Truscott **2016** *Acta neuropathologica communications 4*, 1–12.

[353] D. Gervais **2016** *Journal of Chemical Technology & Biotechnology 91*, 569–575.

[354] N. E. Robinson, A. B. Robinson **2001** *Proceedings of the National Academy of Sciences 98*, 944–949.

[355] L. S. Cantrell, K. L. Schey **2021** *Expert review of proteomics 18*, 119–135.

[356] Y. Ying, H. Li **2022** *Methods 200*, 42–57.

[357] M. Y. S. Hooi, M. J. Raftery, R. J. W. Truscott **2012** *Protein science 21*, 1074–1079.

[358] P. G. Hains, R. J. Truscott **2010** *Investigative ophthalmology & visual science 51*, 3107–3114.

[359] L. Takemoto, D. Boyle **2000** *Mol Vis 6*, 164–168.

[360] V. N. Lapko, A. G. Purkiss, D. L. Smith, J. B. Smith **2002** *Biochemistry 41*, 8638–8648.

[361] B. Norton-Baker, P. Mehrabi, A. O. Kwok, K. W. Roskamp, M. A. Rocha, M. A. Sprague-Piercy, D. von Stetten, R. D. Miller, R. W. Martin **2022** *Structure 30*, 763–776.

[362] J.-L. Velasco-Bolom, L. Domínguez **2023** *Proteins: Structure, Function, and Bioinformatics* .

[363] K. Kato, T. Nakayoshi, Y. Kitamura, E. Kurimoto, A. Oda, Y. Ishikawa **2023** *Biochemistry 62*, 1679–1688.

[364] J.-L. Velasco-Bolom, L. Dominguez **2023** *Biophysical Chemistry 296*, 106986.

[365] K. J. Lampi, Y. H. Kim, H. P. Bachinger, B. A. Boswell, R. A. Lindner, J. A. Carver, T. R. Shearer, L. L. David, D. M. Kapfer **2002** *Molecular Vision 8*, 359–366.

[366] A. J. Guseman, J. J. González, D. Yang, A. M. Gronenborn **2024** *Protein Science 33*, e5120.

[367] Y. Nozaki *Methods in enzymology*, vol. 26 **1972** Elsevier 43–50.

[368] C. N. Pace, G. R. Grimsley, J. M. Scholtz **2008** *Protein Science Encyclopedia: online* , 45–69.

[369] N. A. Morjana, B. J. McKeone, H. F. Gilbert **1993** *Proceedings of the National Academy of Sciences 90*, 2107–2111.

[370] E. I. James, T. A. Murphree, C. Vorauer, J. R. Engen, M. Guttman **2021** *Chemical reviews 122*, 7562–7623.

[371] T. E. Wales, J. R. Engen **2006** *Mass spectrometry reviews 25*, 158–170.

[372] E. A. Hodge, M. A. Benhaim, K. K. Lee **2020** *Protein Science 29*, 843–855.

[373] J. Zheng, T. Strutzenberg, B. D. Pascal, P. R. Griffin **2019** *Current opinion in structural biology 58*, 305–313.

[374] V. Vinciauskaite, G. R. Masson **2023** *Essays in Biochemistry 67*, 301–314.

[375] R. F. Greene, C. N. Pace **1974** *Journal of Biological Chemistry 249*, 5388–5393.

[376] D. Bolen, M. M. Santoro **1988** *Biochemistry 27*, 8069–8074.

[377] E. Freire, A. Schön, B. M. Hutchins, R. K. Brown **2013** *Drug discovery today 18*, 1007–1013.

[378] W. K. Lim, J. Rösgen, S. W. Englander **2009** *Proceedings of the National Academy of Sciences 106*, 2595–2600.

[379] R. Gupta, S. Yadav, F. Ahmad **1996** *Biochemistry 35*, 11925–11930.

[380] A. Pande, N. Mokhor, J. Pande **2015** *Biochemistry 54*, 4890–4899.

[381] S. L. Flaugh, I. A. Mills, J. King **2006** *Journal of Biological Chemistry 281*, 30782–30793.

[382] A. K. Bhuyan **2002** *Biochemistry 41*, 13386–13394.

[383] O. D. Monera, C. M. Kay, R. S. Hodges **1994** *Protein Science 3*, 1984–1991.

[384] T. Takata, J. P. Smith, B. Arbogast, L. L. David, K. J. Lampi **2010** *Experimental eye research 91*, 336–346.

Appendix A

Supplementary material for Human γS-crystallin resists unfolding despite extensive chemical modification from exposure to ionizing radiation

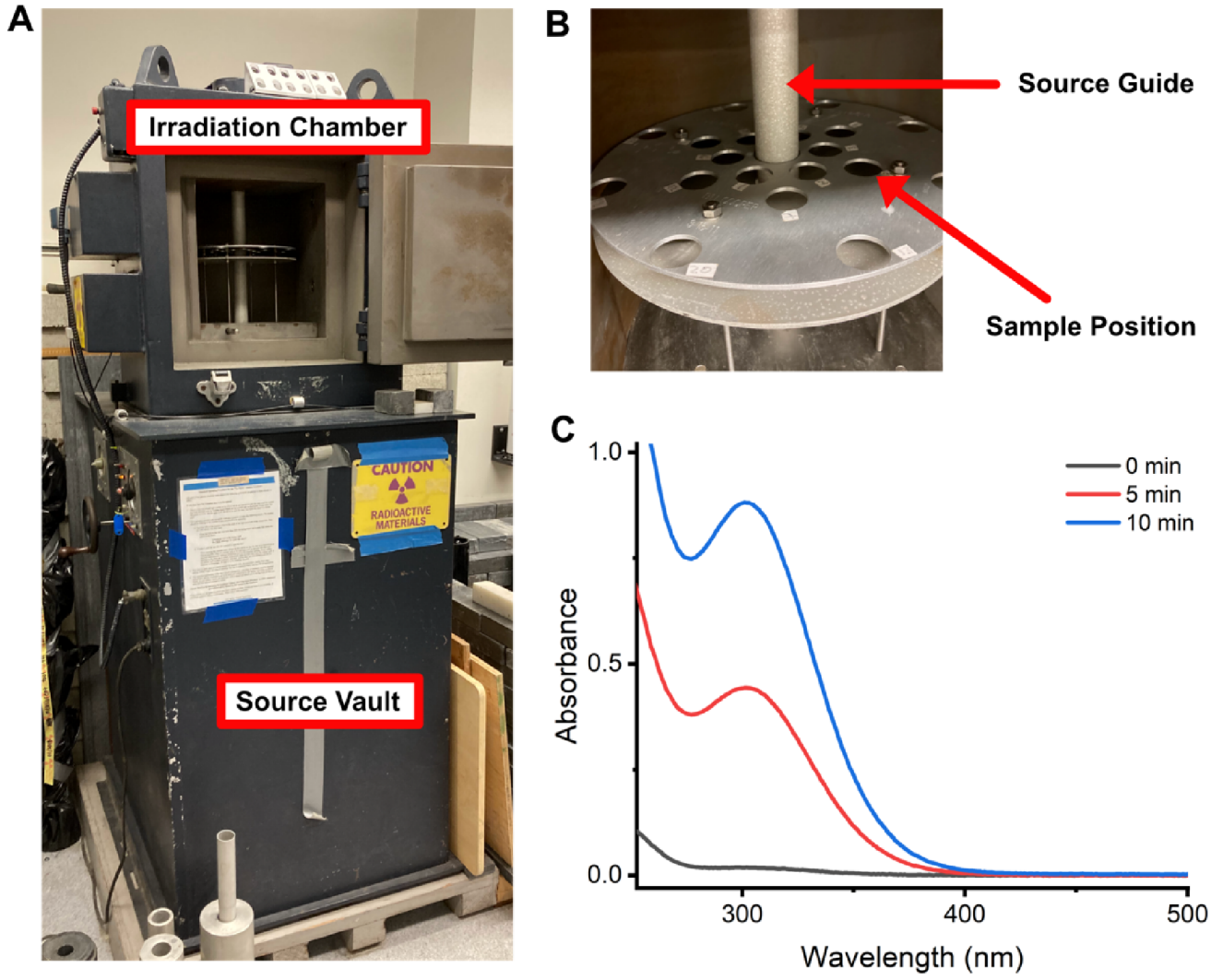

Figure A.1: (A) ^{137}Cs Irradiator Mark-I. The ^{137}Cs is raised into the source guide rod during irradiation. (B) The samples were held in the sample ring at a set distance from the source. (C) Fricke dosimetry was used to confirm the dose for our sample setup. The Fricke solution was irradiated for 5 and 10 minutes and the absorbance at 304 nm was measured as 0.442 after 5 minutes and 0.878 after 10 minutes. The calculated dose rate was 1.54 kGy/hr.

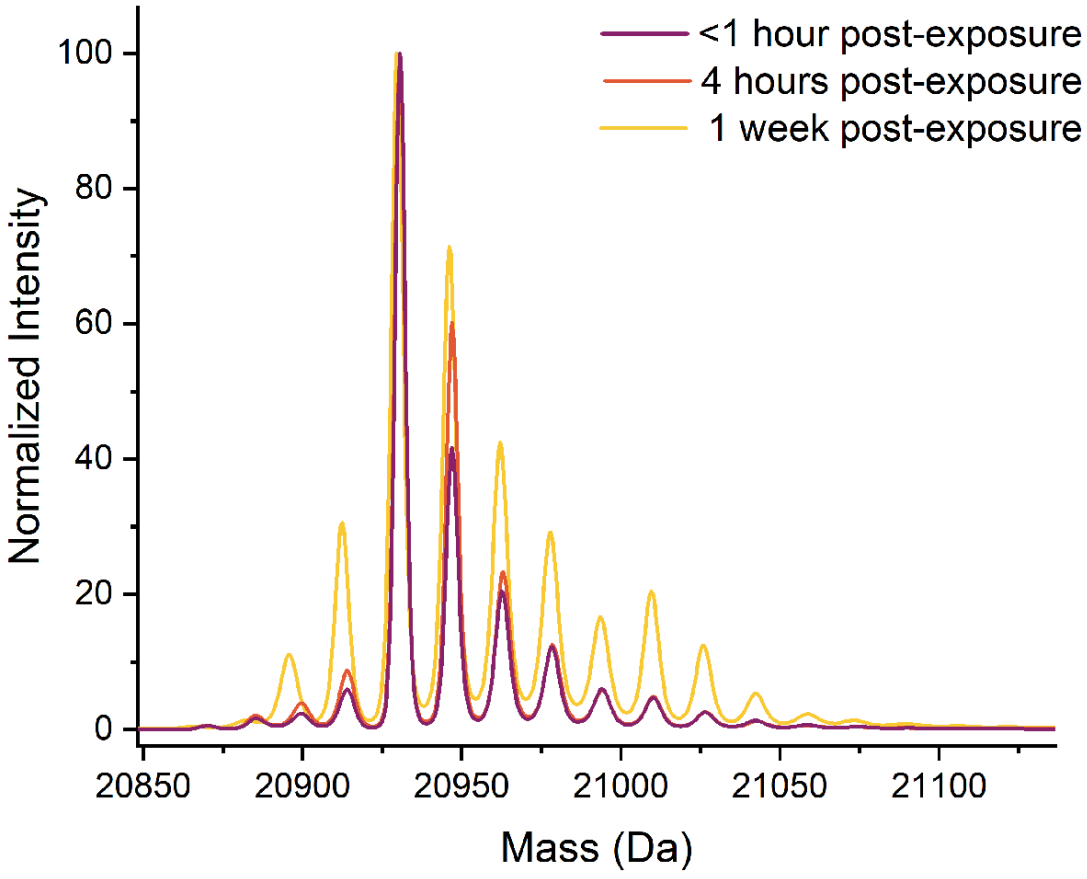

Figure A.2: Deconvoluted intact mass spectra of HγS irradiated for 1 hr/1.5 kGy immediately after removal from the source (purple), 4 hours after removal from the source (orange) and 1 week after removal from the source (yellow). These data indicate that HγS continues to be modified post-exposure.

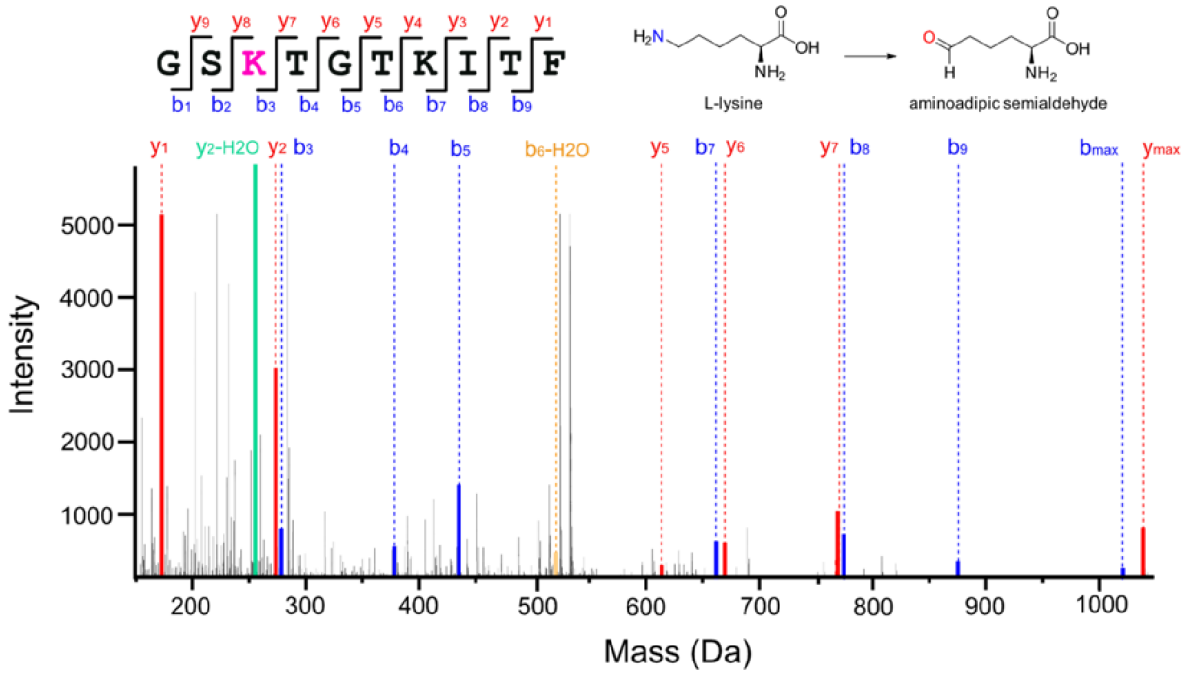

Assignment	Mass (Da)	Intensity (counts)	Modifiers
y1	166.08	5052	
y2-H2O	249.16	21340	
y2	267.13	3224	
b3	272.14	846	Oxidation K (1)
b4	373.17	481	Oxidation K (1)
b5	430.23	1523	Oxidation K (1)
b6-H2O	513.21	297	Oxidation K (1)
y5	609.36	164	
b7	659.34	654	Oxidation K (1)
y6	666.41	651	
y7	767.45	1147	
b8	772.44	741	Oxidation K (1)
b9	873.51	362	Oxidation K (1)

Figure A.3: Tandem mass spectrum and peak list for the pepsin digest peptide 1-GSKTGTKITF-10. The b3 ion and subsequent b ions show a -1 Da loss on one of the first three residues. Oxidation of lysine results in a -1 Da loss in the conversion to the aldehyde derivative, suggesting this peptide resulted from an oxidation of K3.

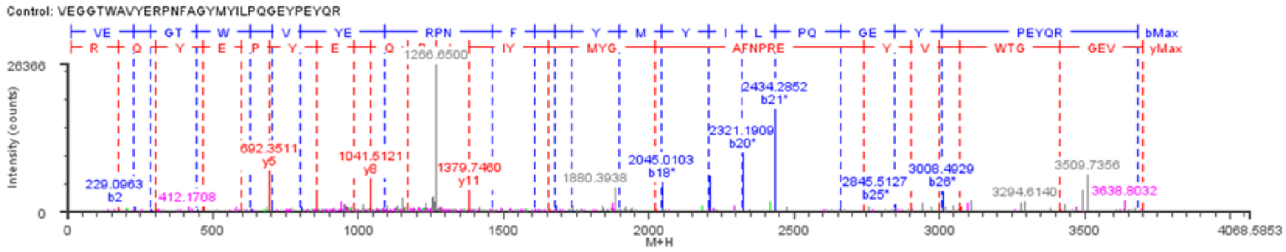

Assignment	Mass (Da)	Intensity (counts)	Modifiers	Assignment	Mass (Da)	Intensity (counts)	Modifiers
y1	175.0959	259		y11-H2O	1361.718	507	
a2	201.1006	787		y11	1379.746	3853	
b2	229.0963	831		b13	1459.5951	160	
a3	258.1041	108		a14	1578.8434	474	
b3	286.1269	219		b14	1606.8911	486	
y2	303.1582	219		y13	1655.9369	312	
b5	444.197	203		b15	1677.8593	1116	
y3	466.2321	943		b16	1734.9816	260	
y4	595.2849	488		a17	1870.0011	270	
a6	602.2539	146		b17	1898.0344	354	
b6	630.2852	266		y16*	2023.0513	223	Oxidation M (1)
a7	673.3377	323		b18*	2045.0103	5182	Oxidation M (1)
y5	692.3511	7252		a19*	2180.1023	1169	Oxidation M (1)
b7	701.3341	896		b19*	2208.0957	6344	Oxidation M (1)
b8	800.4171	934		b20*	2321.1909	10556	Oxidation M (1)
y6-NH3	838.412	162		b21*-H2O	2416.2446	1825	Oxidation M (1)
y6	855.4312	3544		b21*	2434.2852	18326	Oxidation M (1)
y7-H2O	966.4432	772		b23*	2659.4243	1141	Oxidation M (1)
y7	984.4826	1396		y22*	2737.4307	521	Oxidation M (1)
y8	1041.5121	5972		b25*	2845.5127	1316	Oxidation M (1)
b10-NH3	1075.5303	469		y23*	2900.5312	1408	Oxidation M (1)
b10	1092.5646	499		y24*	2999.5962	712	Oxidation M (1)
y9	1169.5917	1210		b26*	3008.4929	3712	Oxidation M (1)
a11	1220.6372	605		y25*	3070.6343	832	Oxidation M (1)
y10-NH3	1249.5657	645		y28*	3414.356	202	Oxidation M (1)
y10	1266.5886	16750					

Figure A.4: Tandem mass spectrum and peak list for the trypsin digest peptide 42-VEGGTWAVYERPNFAGYMYILPQGEYPEYQR-72. The lack of mass change on the b17 ion and the addition of +16 Da to the b18 ion and subsequent b ions demonstrates oxidation of M59.

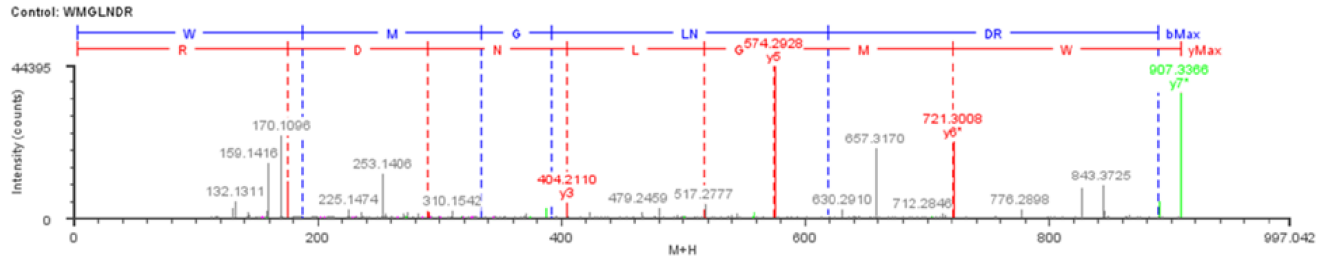

Assignment	Mass (Da)	Intensity (counts)	Modifiers
y1-H2O	157.1165	161	
y1-NH3	158.1063	509	
b1-H2O	169.1132	263	
y1	175.1681	10688	
b1	187.1351	370	
y2-H2O	272.1727	285	
y2	290.1894	1759	
a2*	306.159	154	Oxidation M (1)
b2*-NH3	317.132	644	Oxidation M (1)
b2*	334.1506	1936	Oxidation M (1)
a3*	363.1932	135	Oxidation M (1)
b3*-H2O	373.1554	181	Oxidation M (1)
b3*-NH3	374.1442	440	Oxidation M (1)
y3-H2O	386.2054	148	
y3-NH3	387.1898	3147	
b3*	391.1672	517	Oxidation M (1)
y3	404.211	4463	
a4*	476.2625	112	Oxidation M (1)
y4-NH3	500.2557	555	
y4	517.1648	361	
y5-H2O	556.2769	391	
y5-NH3	557.2661	1780	
y5	574.2928	44395	
b5*	618.2497	157	Oxidation M (1)
y6*-H2O	703.293	835	Oxidation M (1)
a6*	705.268	153	Oxidation M (1)
y6*	721.3008	22470	Oxidation M (1)
y7*-H2O	889.3745	135	Oxidation M (1)
y7*-NH3	890.4197	4937	Oxidation M (1)
y7*	907.3366	36780	Oxidation M (1)

Figure A.5: Tandem mass spectrum and peak list for the trypsin digest peptide 73-WMGLNDR-79. The lack of mass change on the y5 ion and the addition of +16 Da to the y6 ion and subsequent y ions, as well as lack of mass change on b1 and addition of +16 Da to the b2 ion and subsequent b ions demonstrates oxidation of M74.

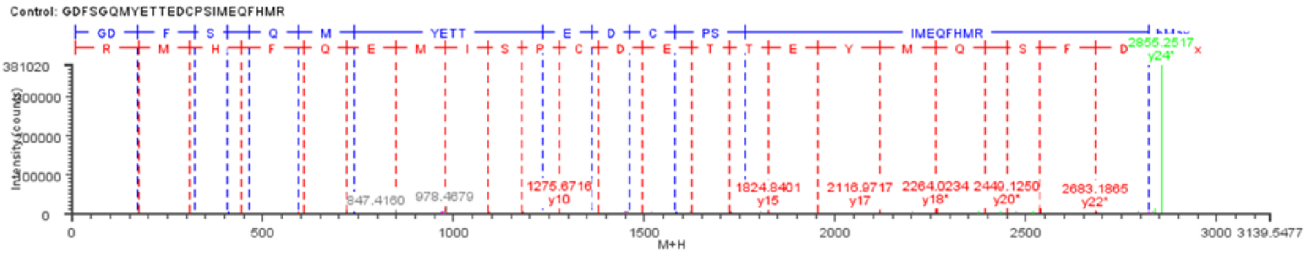

Assignment	Mass (Da)	Intensity (counts)	Modifiers	Assignment	Mass (Da)	Intensity (counts)	Modifiers
y1-H2O	157.1475	190		y6	847.6084	113	
b2	173.1071	197		a8*	874.3091	126	Oxidation M (1)
y1	175.1685	621		b8*	902.5993	304	Oxidation M (1)
a3	292.1702	205		y7	978.6574	171	
y2	306.1979	1088		b9-NH3	998.5712	154	
b3	320.1623	693		b9	1015.2303	173	
a4	379.1808	209		y8	1091.4393	901	
b4-H2O	389.1756	723		b10*	1132.2902	1413	Oxidation M (1)
b4	407.1785	1020		y9	1178.4476	743	
y3	443.2347	1150		b11*	1233.3702	304	Oxidation M (1)
b5-H2O	446.1916	206		y10	1275.5873	2134	
b5-NH3	447.1919	197		y11	1378.3569	254	
b5	464.203	237		y12	1493.3458	479	
b6-H2O	574.2232	221		y14	1723.6437	666	
b6-NH3	575.2215	378		y15	1824.5723	1109	
y4	590.2869	1464		y16	1953.7211	843	
b6	592.235	645		y17	2116.7334	2223	
y5-NH3	701.2923	410		y18*	2263.7605	824	Oxidation M (1)
y5	718.2914	1389		y20*	2449.6069	847	Oxidation M (1)
b7*-H2O	721.2454	224	Oxidation M (1)	y21*	2536.7844	631	Oxidation M (1)
b7*	739.2623	304	Oxidation M (1)	y24*-H2O	2836.8862	3208	Oxidation M (1)
y6-H2O	829.328	409		y24*	2854.9028	62097	Oxidation M (1)

Figure A.6: Tandem mass spectrum and peak list for the trypsin digest peptide 102-GDFSGQMYETTEDCPSIMEQFHMR-125. The lack of mass change on the y17 ion and the addition of +16 Da to the y18 ion and subsequent y ions, as well as lack of mass change on the b6 ion and the addition of +16 Da to the b7 ion and subsequent b ions demonstrates oxidation of M108.

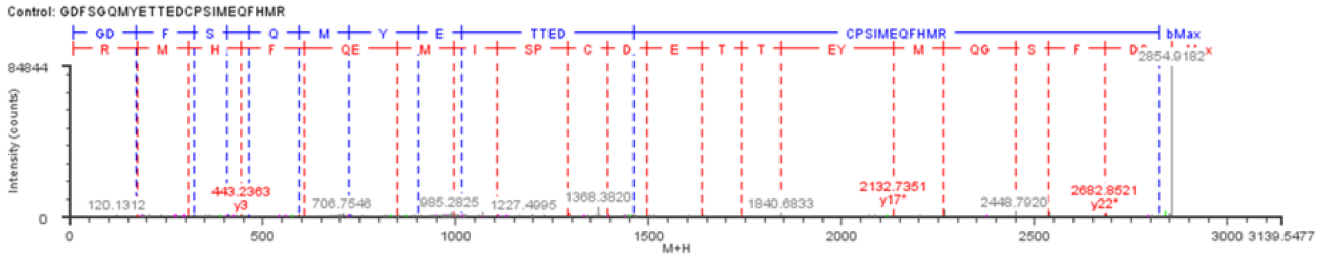

Assignment	Mass (Da)	Intensity (counts)	Modifiers	Assignment	Mass (Da)	Intensity (counts)	Modifiers
y1-H2O	157.148	181		b9-H2O	997.2227	332	
b2	173.1058	283		a9*	1003.5489	478	Oxidation M (1)
y1	175.1667	789		b9	1015.3193	353	
y2-H2O	288.1487	174		y8*	1107.4937	322	Oxidation M (1)
y2-NH3	289.1779	120		a11*	1205.4117	135	Oxidation M (1)
a3	292.1692	300		y10*	1291.5879	2083	Oxidation M (1)
b3-H2O	302.1481	208		y11*	1394.5739	922	Oxidation M (1)
y2	306.1983	1310		a13*	1449.9229	923	Oxidation M (1)
b3	320.1605	1214		b13	1461.7791	163	
a4	379.1925	245		b13*	1477.2343	249	Oxidation M (1)
b4-H2O	389.1752	927		y12	1493.8676	227	
b4	407.1804	1533		y12*	1509.4847	275	Oxidation M (1)
a5	436.2003	178		y13*	1638.4642	107	Oxidation M (1)
y3	443.2363	1537		y14*	1739.5192	1095	Oxidation M (1)
b5	464.1914	682		y15*	1840.5464	1483	Oxidation M (1)
a6	564.1924	114		y17*-H2O	2114.7209	551	Oxidation M (1)
y4-NH3	573.2664	189		y17*	2132.7351	4672	Oxidation M (1)
b6-H2O	574.2233	1063		y18*-H2O	2245.6943	247	Oxidation M (1)
y4	590.2895	1447		y18*	2263.5925	3580	Oxidation M (1)
b6	592.222	1222		y19*			
b7	723.2507	910		y20*-NH3	2432.6448	291	Oxidation M (1)
y6-H2O	829.2997	483		y20*	2449.6072	1860	Oxidation M (1)
y6	847.3151	1870		y21*-H2O	2518.5969	186	Oxidation M (1)
b8-H2O	868.2592	483		y21*	2535.6409	1676	Oxidation M (1)
b8-NH3	869.3275	143		y22*	2682.8521	2043	Oxidation M (1)
b8	886.3123	339		y24*-H2O	2836.9375	3376	Oxidation M (1)
y7*	994.3598	987	Oxidation M (1)	y24*	2854.6646	7479	Oxidation M (1)

Figure A.7: Tandem mass spectrum and peak list for the trypsin digest peptide 102-GDFSGQMYETTEDCPSIMEQFHMR-125. The lack of mass change on the y6 ion and the addition of +16 Da to the y7 ion and subsequent y ions demonstrates oxidation of M119.

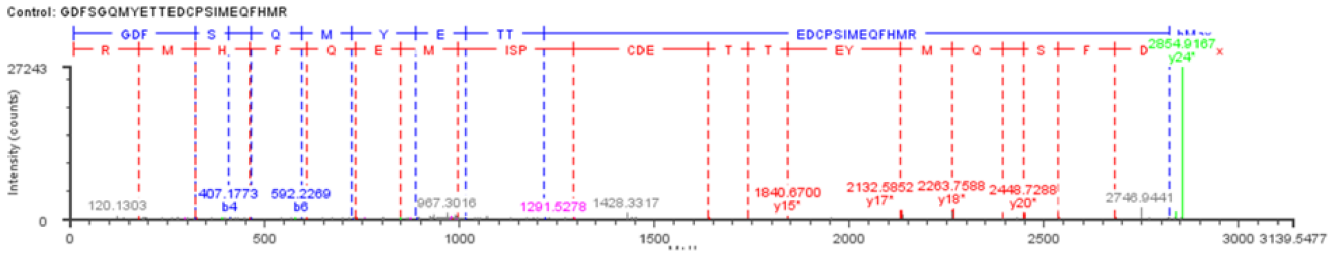

Assignment	Mass (Da)	Intensity (counts)	Modifiers
y1	175.1654	329	
b3	320.1557	278	
y2*	322.1915	122	Oxidation M (1)
b4-H2O	389.1705	297	
b4	407.1773	475	
y3*	459.2289	232	Oxidation M (1)
b5	464.1888	126	
b6-H2O	574.2421	177	
b6-NH3	575.219	329	
b6	592.2269	448	
y4*	606.2795	242	Oxidation M (1)
b7	723.2176	256	
y5*	734.2537	188	Oxidation M (1)
y6*-NH3	846.2582	223	Oxidation M (1)
y6*	863.2909	207	Oxidation M (1)
b8	886.3071	162	
y7*	994.3729	214	Oxidation M (1)
b9-H2O	997.3035	194	
b9	1015.2784	279	
b11	1217.3018	219	
y10*	1291.4392	176	Oxidation M (1)
y13*	1638.5977	268	Oxidation M (1)
y14*	1739.5386	479	Oxidation M (1)
y15*	1840.67	619	Oxidation M (1)
y17*	2132.5852	1728	Oxidation M (1)
y18*	2263.7588	1840	Oxidation M (1)
y19*	2391.7827	615	Oxidation M (1)
y20*	2448.7288	1236	Oxidation M (1)
y21*	2535.8076	474	Oxidation M (1)
y22*	2683.0017	558	Oxidation M (1)
y24*-H2O	2836.7964	1315	Oxidation M (1)
y24*	2854.9167	27243	Oxidation M (1)

Figure A.8: Tandem mass spectrum and peak list for the trypsin digest peptide 102-GDFSGQMYETTEDCPSIMEQFHMR-125. The lack of mass change on the y1 ion and the addition of +16 Da to the y2 ion and subsequent y ions demonstrates oxidation of M124.

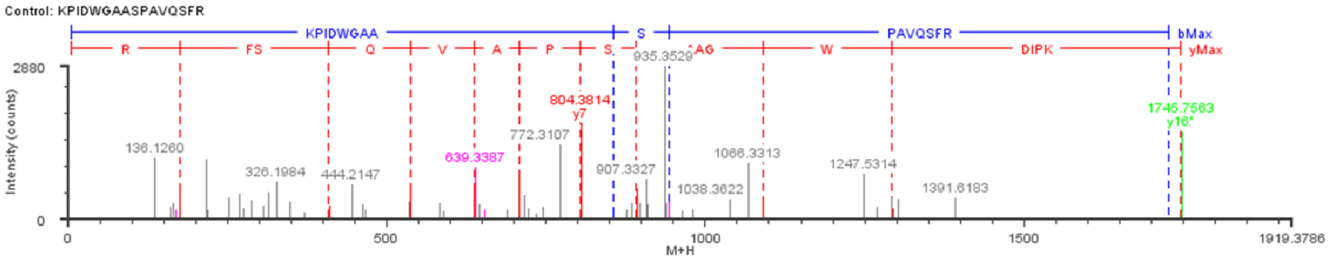

Assignment	Mass (Da)	Intensity (counts)	Modifiers
y1	175.1682	550	
y3	409.238	244	
y4	537.2903	646	
y5	636.3266	657	
y6	707.3299	850	
y7	804.3814	1814	
b8*	855.4062	208	Hydroxyl W (1)
y8	891.4169	587	
b9*	942.3573	310	Hydroxyl W (1)
y11	1090.4874	365	
y12*	1292.4341	209	Hydroxyl W (1)
y16*	1745.7563	1664	Hydroxyl W (1)

Figure A.9: Tandem mass spectrum and peak list for the trypsin digest peptide 159-KPIDWGAASPAVQSFR-174. The lack of mass change on the y11 ion and the addition of +16 Da to the y12 ion and subsequent y ions demonstrates oxidation of W163.

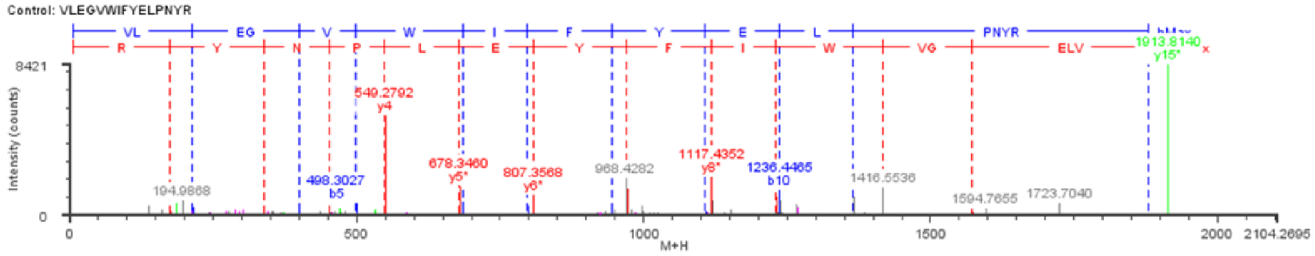

Assignment	Mass (Da)	Intensity (counts)	Modifiers
y1	175.1661	229	
a2	185.2138	667	
b2	213.2073	442	
y2	338.2161	238	
a4	371.2521	147	
b4	399.253	457	
y3	452.242	164	
a5	470.3103	380	
b5	498.3027	658	
y4-NH3	532.258	262	
y4	549.2792	5576	
y5*	678.346	1644	Oxidation L (1)
b6	684.348	705	
b7	797.4233	499	
y6*	807.3568	1127	Oxidation L (1)
b8	944.407	495	
y7*	970.3701	1461	Oxidation L (1)
b9	1107.4791	227	
y8*	1117.4352	2122	Oxidation L (1)
y9*	1230.5137	1042	Oxidation L (1)
b10	1236.4465	1367	
b11*	1365.4825	793	Oxidation L (1)
y10*	1416.4567	1164	Oxidation L (1)
y12*	1572.5155	126	Oxidation L (1)
y15*	1913.814	8421	Oxidation L (1)

Figure A.10: Tandem mass spectrum and peak list for the trypsin digest peptide 132-VLEGVWIFYELPNYR-146. The lack of mass change on the y4 ion and the addition of +16 Da to the y5 ion and subsequent y ions demonstrates oxidation of L142 .

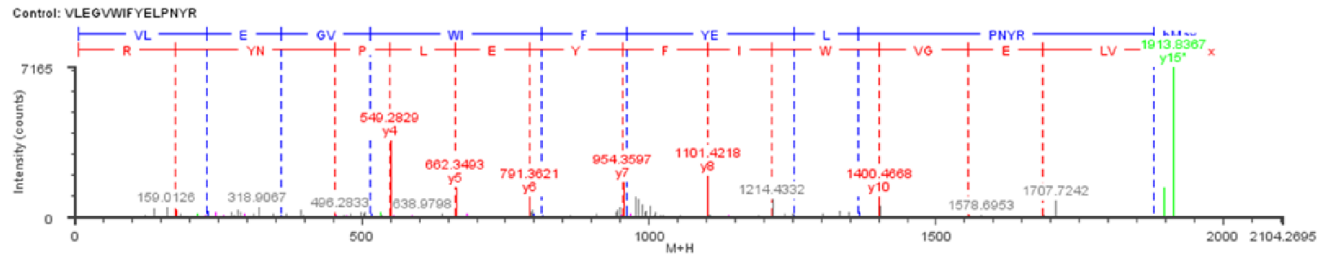

Assignment	Mass (Da)	Intensity (counts)	Modifiers
y1	175.1667	355	
b2*-H2O	211.1922	153	Oxidation L (1)
b2*-NH3	212.1445	167	Oxidation L (1)
b2*	229.1992	318	Oxidation L (1)
b3*	358.2214	100	Oxidation L (1)
y3	452.2447	174	
b5*	514.2862	165	Oxidation L (1)
y4-NH3	532.2471	259	
y4	549.2829	3677	
y5	662.3493	1447	
y6	791.3621	995	
b7	797.4	188	
b7*	813.4266	128	Oxidation L (1)
b8*-H2O	942.4509	188	Oxidation L (1)
y7	954.3597	1693	
b8*	960.3894	193	Oxidation L (1)
y8	1101.4218	1982	
y9	1214.5216	649	
b10*	1252.4352	130	Oxidation L (1)
b11*-H2O	1347.5851	151	Oxidation L (1)
b11*	1365.5822	276	Oxidation L (1)
y10	1400.4668	1003	
y12	1556.4976	104	
y13	1685.7007	414	
y15*-H2O	1895.8267	1405	Oxidation L (1)
y15*	1913.8367	7165	Oxidation L (1)

Figure A.11: Tandem mass spectrum and peak list for the trypsin digest peptide 132-VLEGVWIFYELPNYR-146. The +16 Da to the b2 ion and subsequent b ions as well as the lack of mass change on the y13 ion and the addition of +16 Da to the y15 ion suggests oxidation of one of the first two residues, V132 or L133.

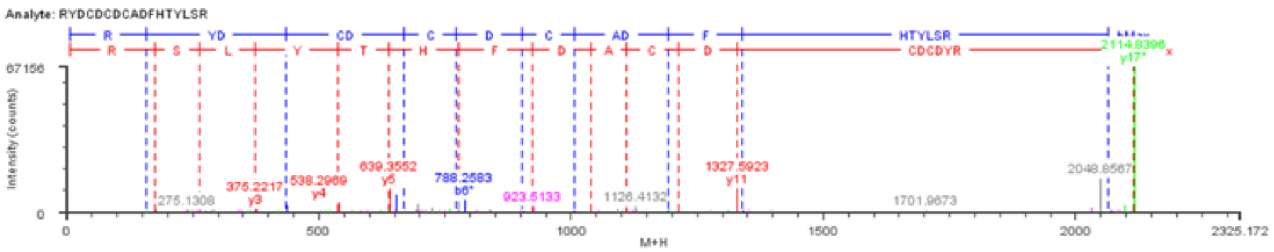

Assignment	Mass (Da)	Intensity (counts)	Modifiers
b1	157.0848	103	
y1-NH3	158.0684	177	
y1	175.0946	836	
y2-NH3	245.1042	448	
y2	262.1321	561	
a2	292.1598	270	
b2-H2O	301.8922	261	
b2-NH3	303.1271	139	
b2	320.1538	379	
y3-NH3	358.1931	264	
y3	375.2232	946	
b3-NH3	418.159	343	
b3	435.1883	1843	
y4-NH3	521.1841	147	
y4	538.298	2358	
y5-H2O	621.3363	605	
b5-H2O	635.2336	137	
b5-NH3	636.2181	621	
y5	639.3536	6649	
b5	653.2436	3430	
y6-H2O	758.421	249	
y6	776.3777	1156	
b6*	788.2567	2903	Oxidation x2 C (1)
b7*	903.297	181	Oxidation x2 C (1)
y7-H2O	905.4447	613	
y7	923.4589	1445	
y8	1038.4944	794	
y9-H2O	1091.4211	267	
y9	1109.5372	1088	
b10*	1192.3947	709	Oxidation x2 C (1)
y10-H2O	1194.543	174	
y10	1212.552	984	
y11	1327.5912	5136	
b11*	1339.4871	386	Oxidation x2 C (1)
y17*-H2O	2096.8257	1878	Oxidation x2 C (1)
y17*	2114.8364	34572	Oxidation x2 C (1)

Figure A.12: Tandem mass spectrum and peak list for the trypsin digest peptide 20-RYDCDCDCADFHTYLSR-36. The lack of mass change on the b5 ion and the addition of +32 Da to the b6 ion and subsequent b ions demonstrates oxidation of C25.

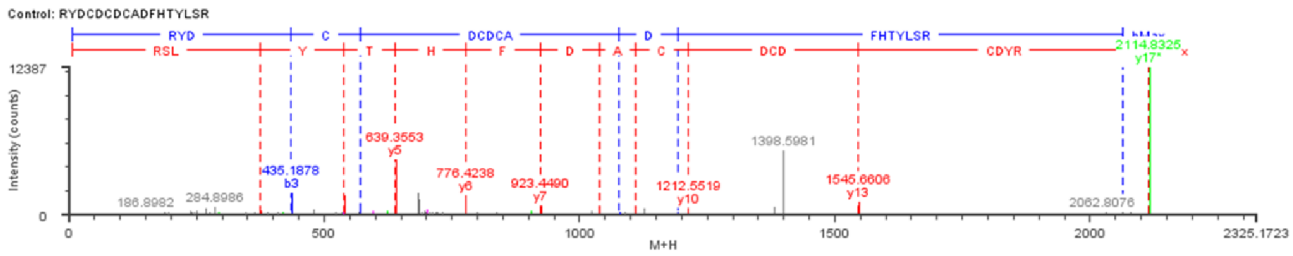

Assignment	Mass (Da)	Intensity (counts)	Modifiers
a2	292.1593	185	
y3	375.2163	305	
b3-NH3	418.1617	228	
b3	435.1878	1809	
y4	538.2961	1567	
b4*	570.1988	1021	Oxidation x2 C (1)
y5-H2O	621.341	375	
y5	639.3553	4632	
y6	776.4238	1632	
y7-H2O	905.4461	315	
y7	923.449	772	
y8	1038.5558	242	
b9*	1077.4355	134	Oxidation x2 C (1)
y9	1109.5822	332	
b10*	1192.3967	213	Oxidation x2 C (1)
y10	1212.5519	578	
y13	1545.6606	1046	
y17*	2114.8325	12387	Oxidation x2 C (1)

Figure A.13: Tandem mass spectrum and peak list for the trypsin digest peptide 20-RYDCDCDCADFHTYLSR-36. The lack of mass change on the b3 ion and the addition of +32 Da to the b4 ion and subsequent b ions demonstrates oxidation of C23.

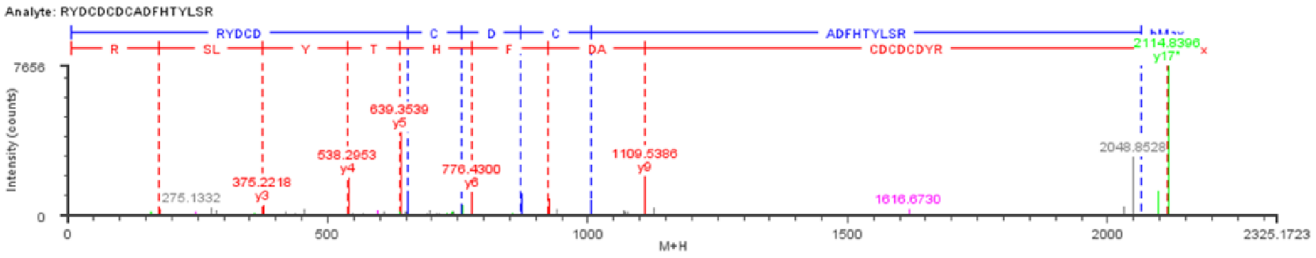

Assignment	Mass (Da)	Intensity (counts)	Modifiers
y1-NH3	158.0683	178	
y1	175.0944	359	
y3-NH3	358.1944	137	
y3	375.2218	547	
y4	538.2953	1935	
b5-NH3	636.2195	212	
y5	639.3539	4230	
b5	653.2458	905	
a6	727.9556	141	
b6-H2O	738.2752	220	
b6	756.2682	242	
y6-H2O	758.3664	507	
y6	776.43	1213	
b7-NH3	854.2782	132	
b7	871.304	1149	
y7	923.4628	835	
b8*	1006.313	801	Oxidation x2 C (1)
y9	1109.5386	1977	
y17*-H2O	2096.8279	1263	Oxidation x2 C (1)
y17*	2114.8396	7656	Oxidation x2 C (1)

Figure A.14: Tandem mass spectrum and peak list for the trypsin digest peptide 20-RYDCDCDCADFHTYLSR-36. The lack of mass change on the b7 ion and the addition of +32 Da to the b8 ion and subsequent b ions demonstrates oxidation of C27.

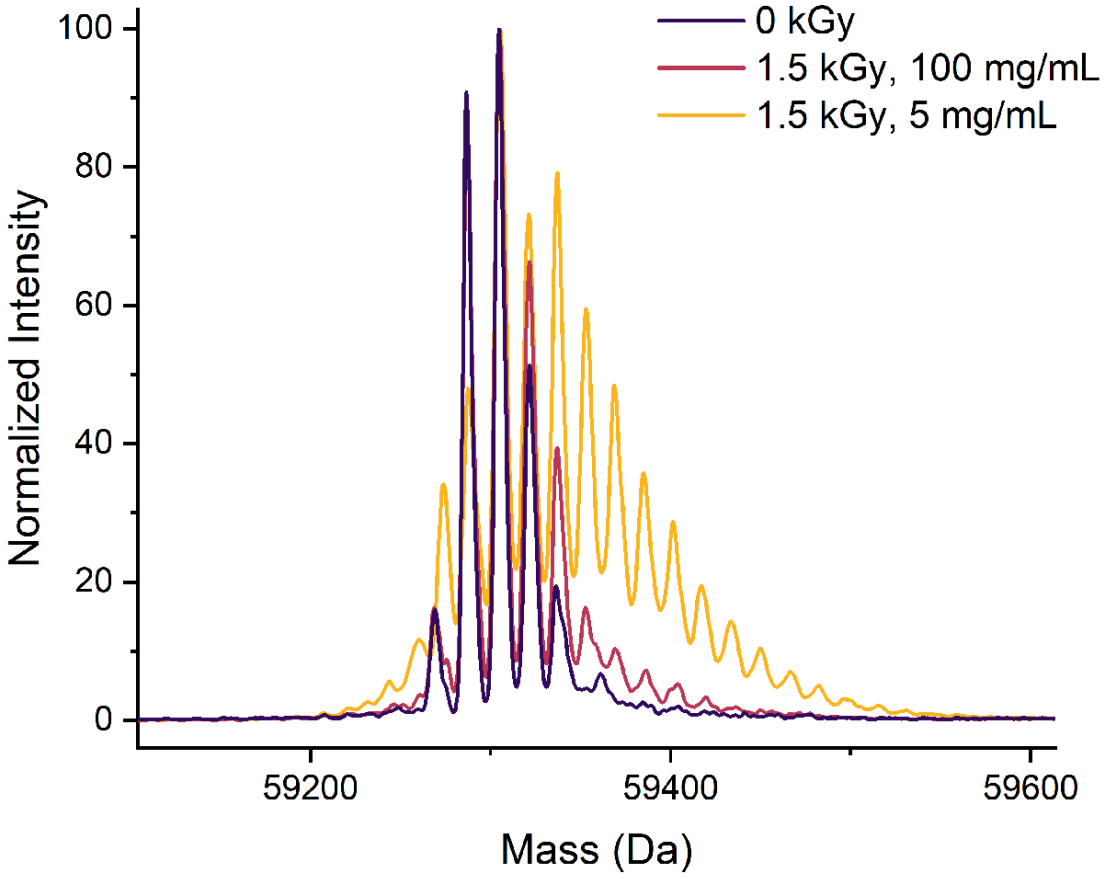

Figure A.15: Comparison of deconvoluted intact mass spectra of lysozyme non-irradiated (purple) and irradiated for 1 hr/1.5 kGy at 100 mg/mL (purple) and 5 mg/mL (yellow). Increased protein concentration appears to reduce the relative amount of modification upon γ irradiation.

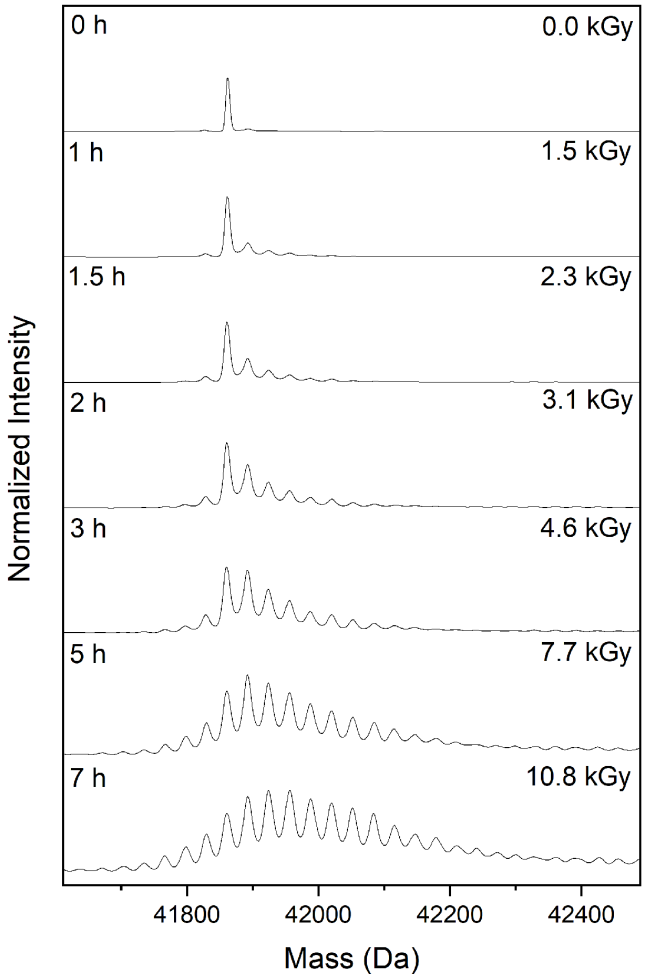

Figure A.16: Evidence of dimerization observed in mass spectra during the course of irradiation. Deconvoluted intact mass spectra of HγS samples irradiated with doses (0, 1.5, 2.3, 3.1, 4.6, 7.7, and 10.8 kGy) of γ radiation show the expected HγS dimer mass.

Appendix B

Supplementary material for Investigating the dynamics and stability of HγS crystallin deamidation variants

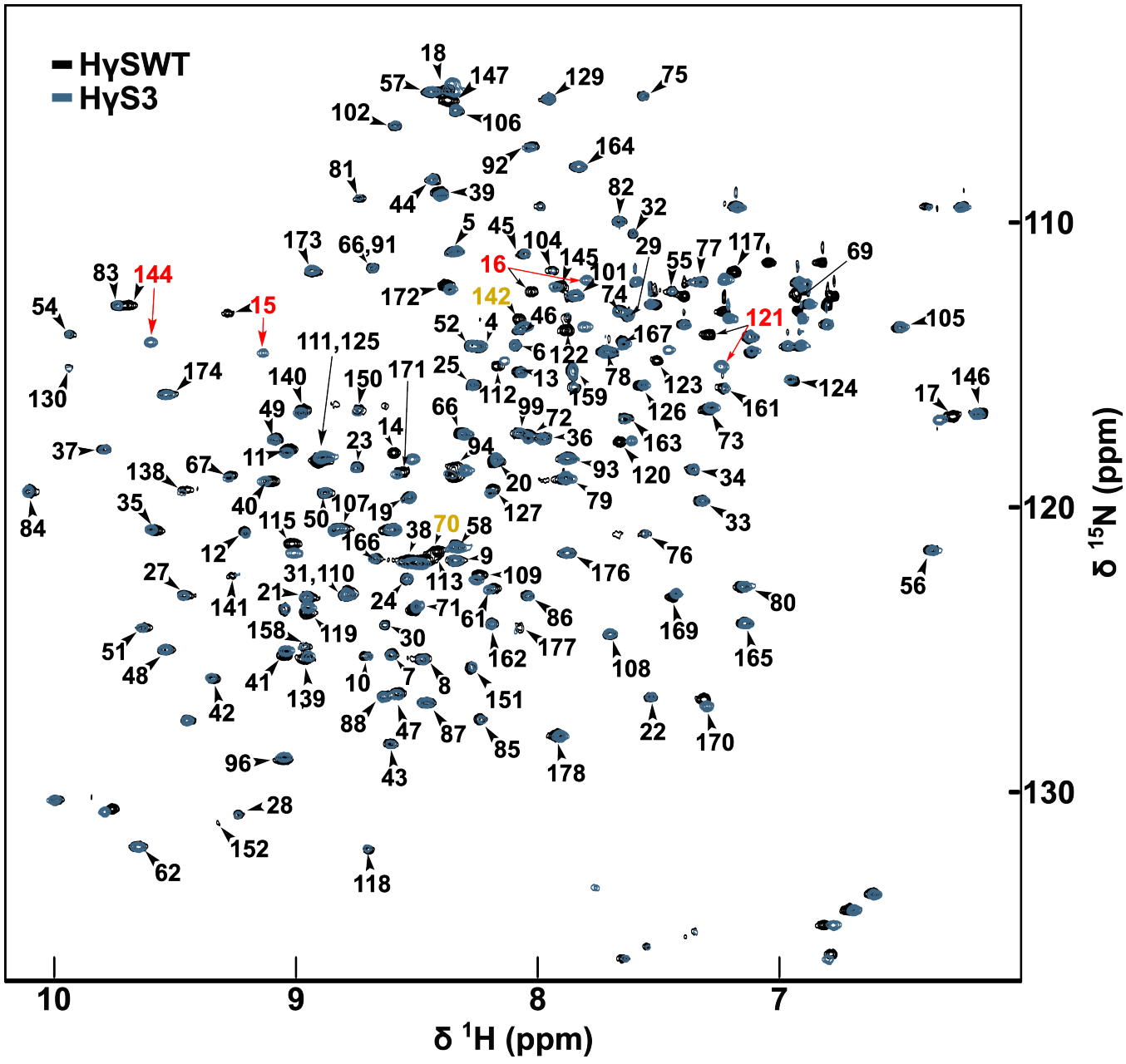
HγSWT
HγS3
δ ¹H (ppm)
δ ¹⁵N (ppm)
10
9
8
7
110
120
130

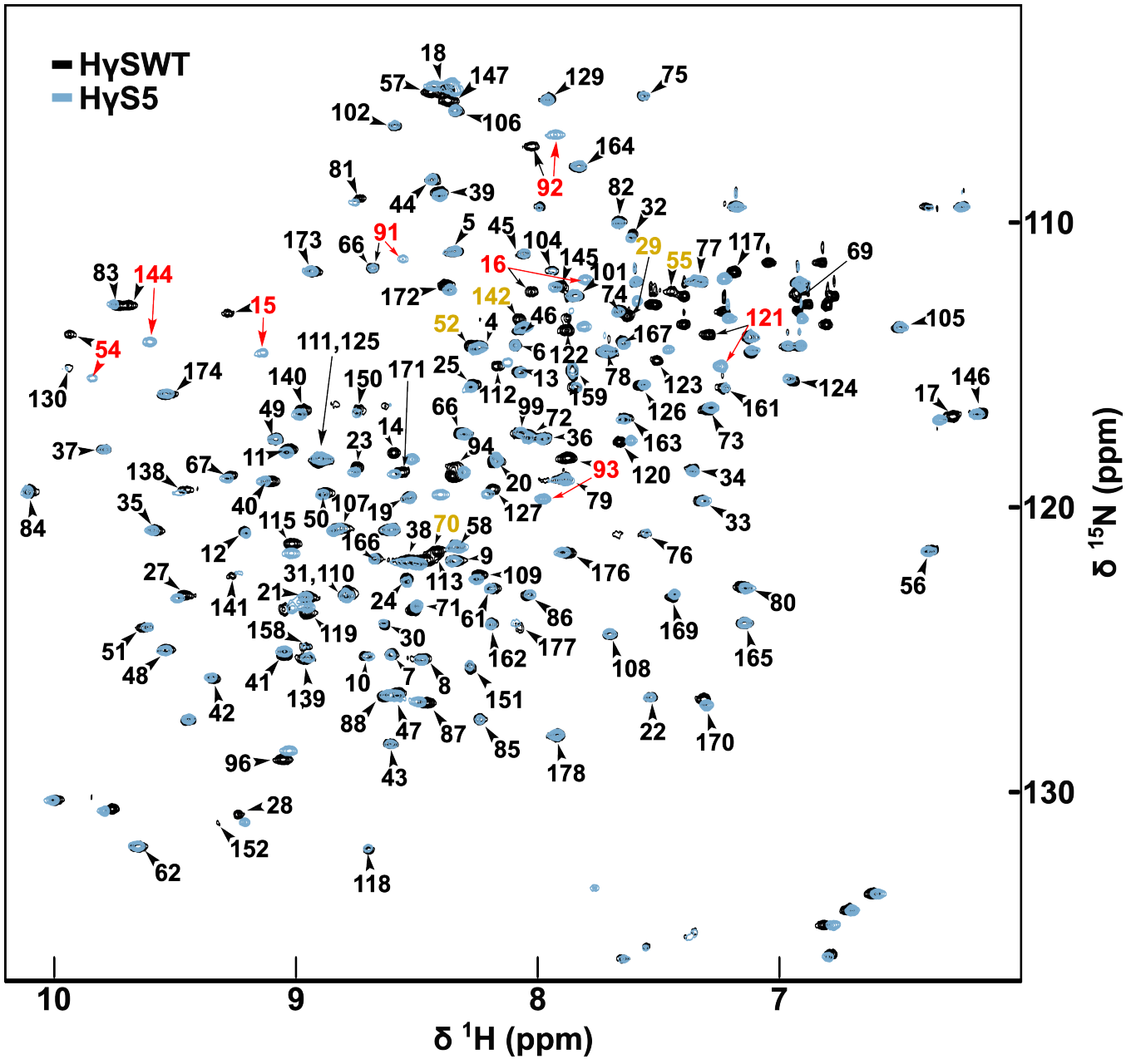
HγSWT
HγS5
δ ¹H (ppm)
δ ¹⁵N (ppm)
10
9
8
7
110
120
130

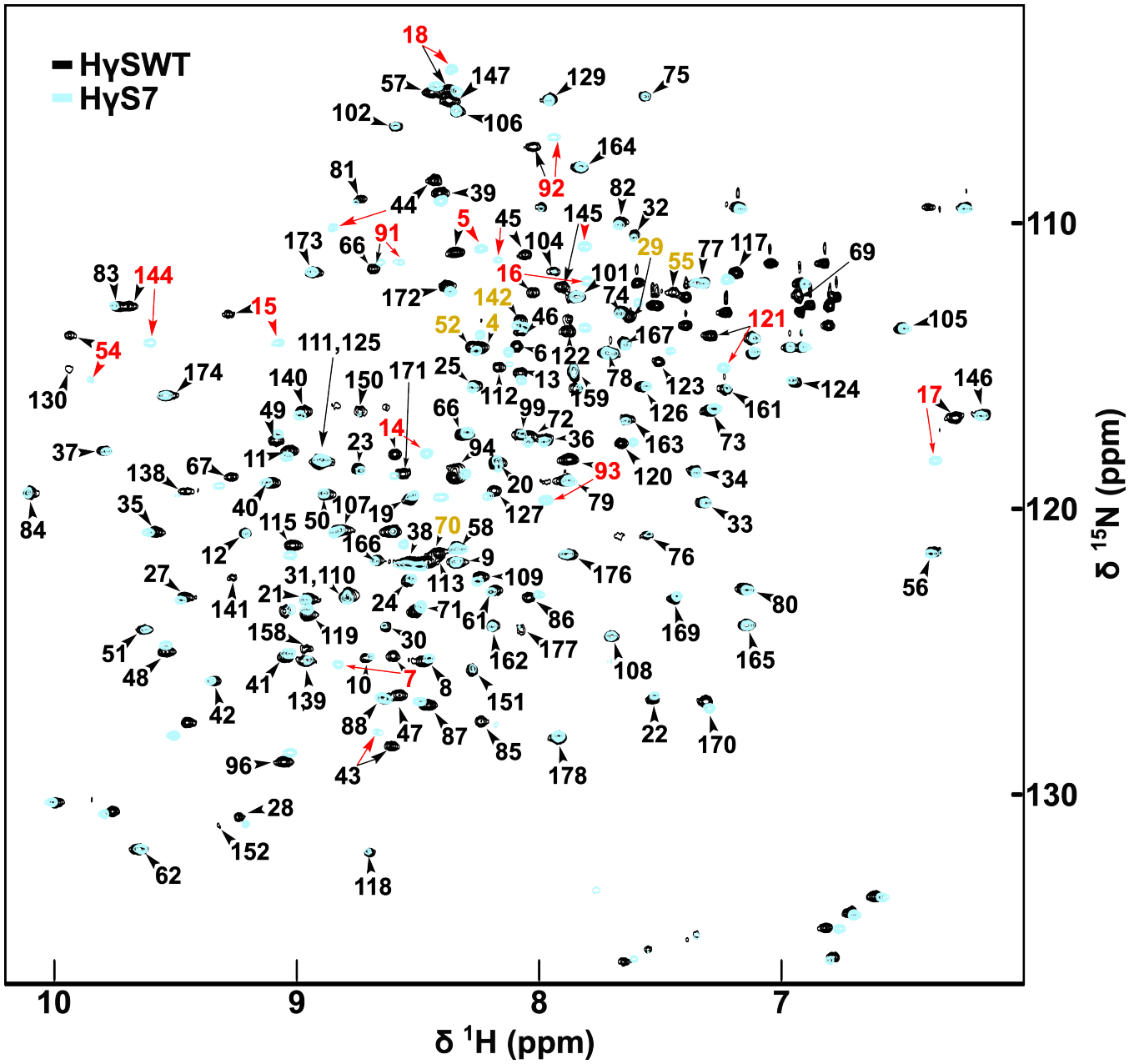
HγSWT
HγS7
δ ¹H (ppm)
δ ¹⁵N (ppm)
10
9
8
7
110
120
130

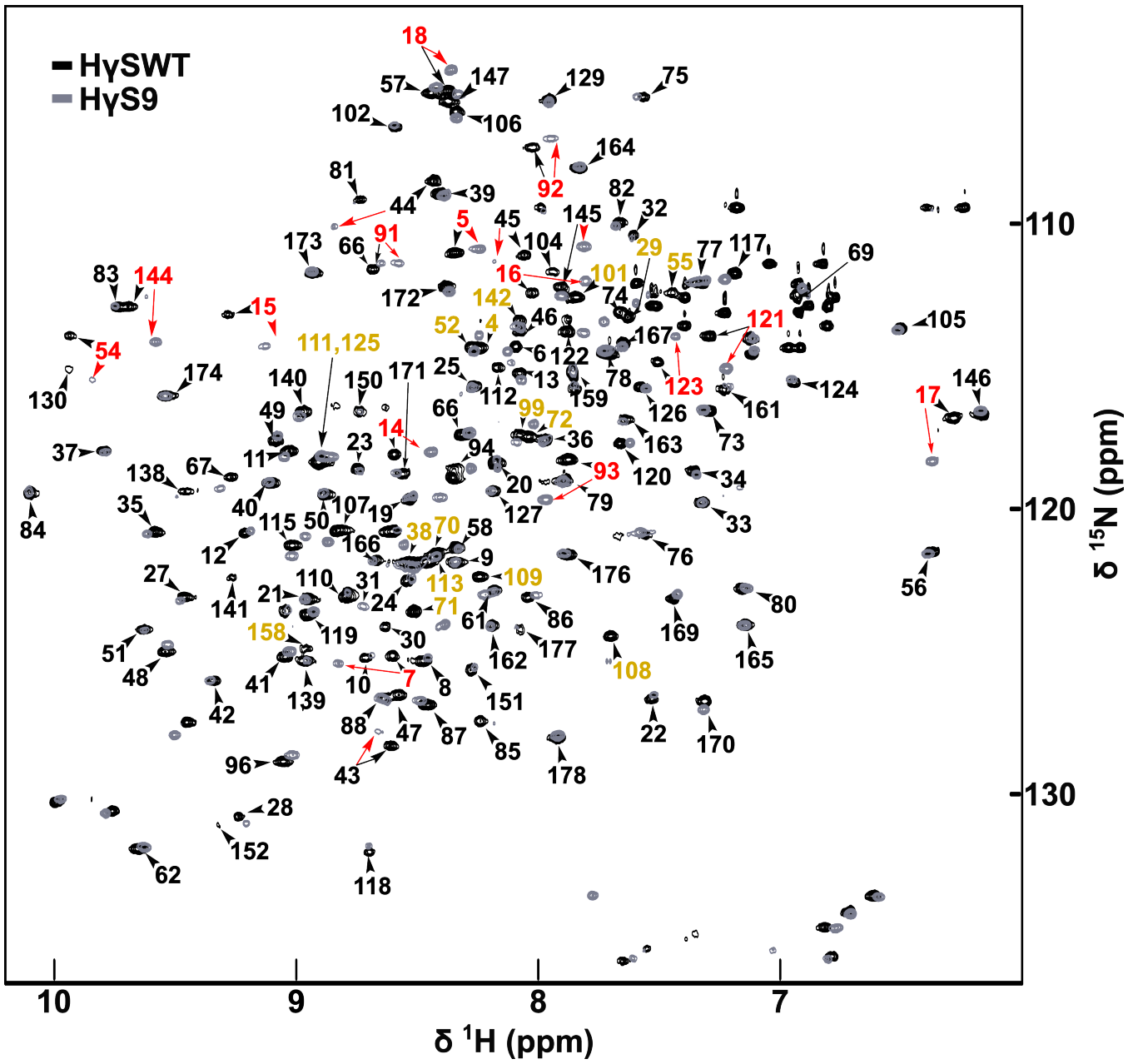

Figure B.0: HγSWT and each deamidation variant ^{1}H-^{15}N-HSQC overlay. Red labels indicate residues that shifted > 0.075 PPM. Yellow labels indicate residues that are not assigned in the variant.

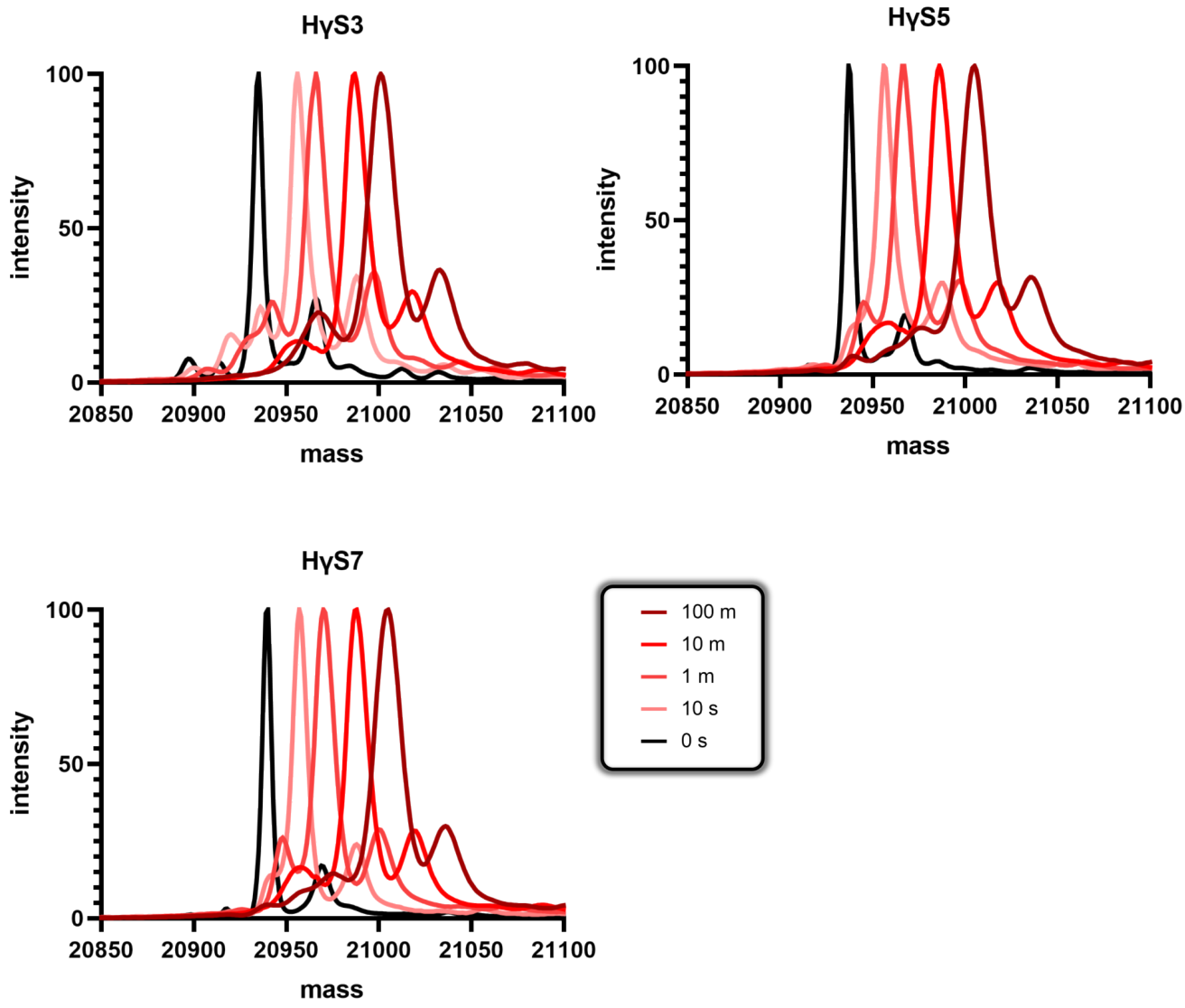

Figure B.1: Deconvoluted mass spectra of intact HγS3, HγS5, and HγS7 during hydrogen/deuterium exchange timecourse.

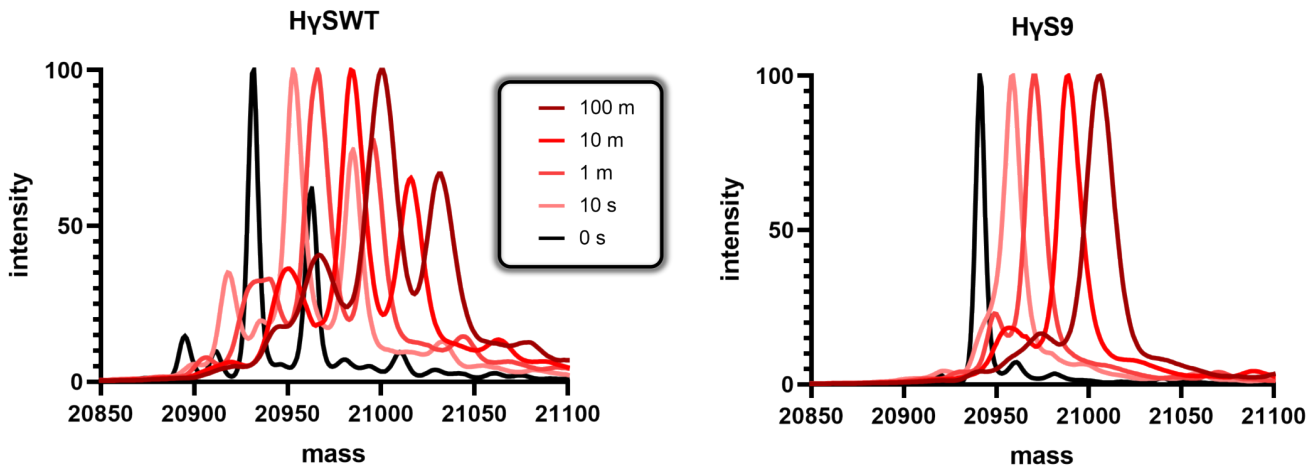

Figure B.2: Deconvoluted mass spectra of intact HγS9 and oxidized HγSWT during hydrogen/deuterium exchange timecourse.

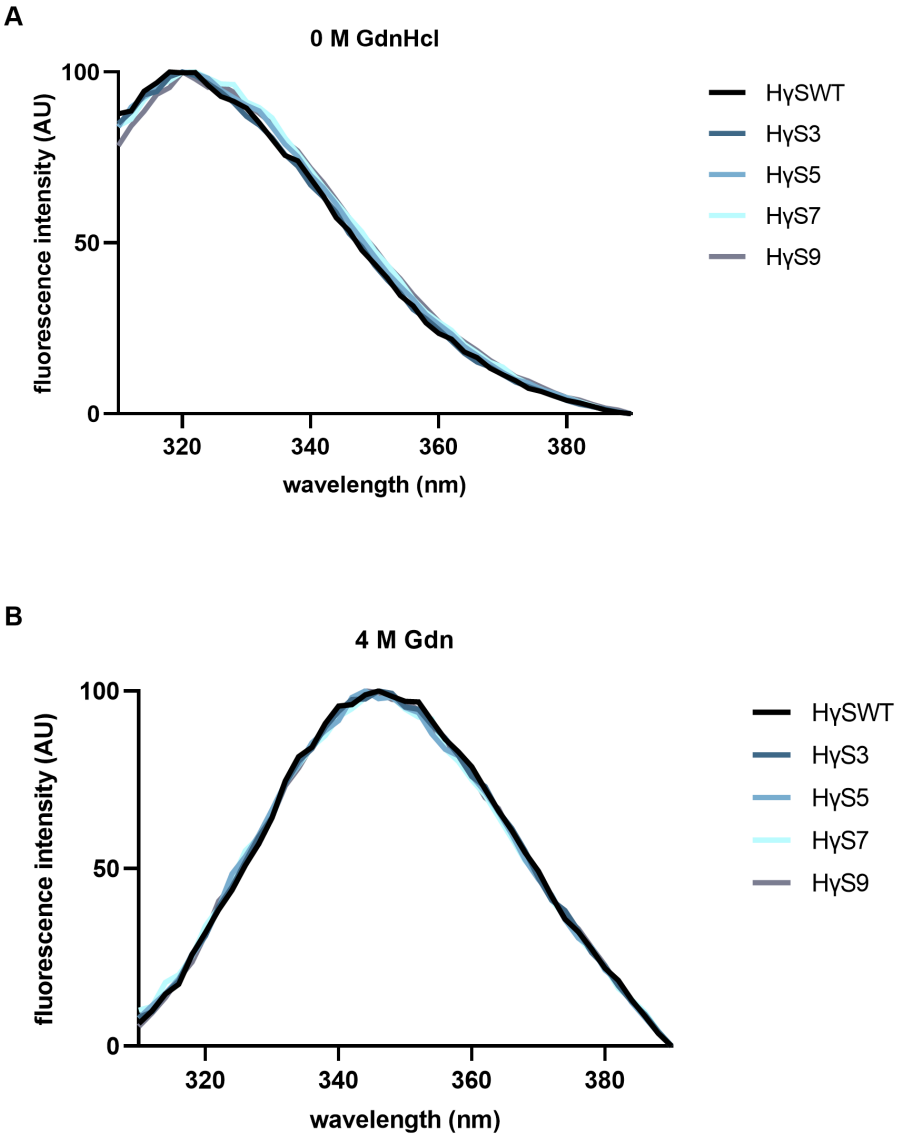

Figure B.3: Normalized fluorescence spectra of HγSWT and each deamidation variant at 0 and 4 M guanidinium chloride (GdnHCl). λ_{ex}=280 was used to excite tryptophan fluorescence which was measured from 310-390 nm.

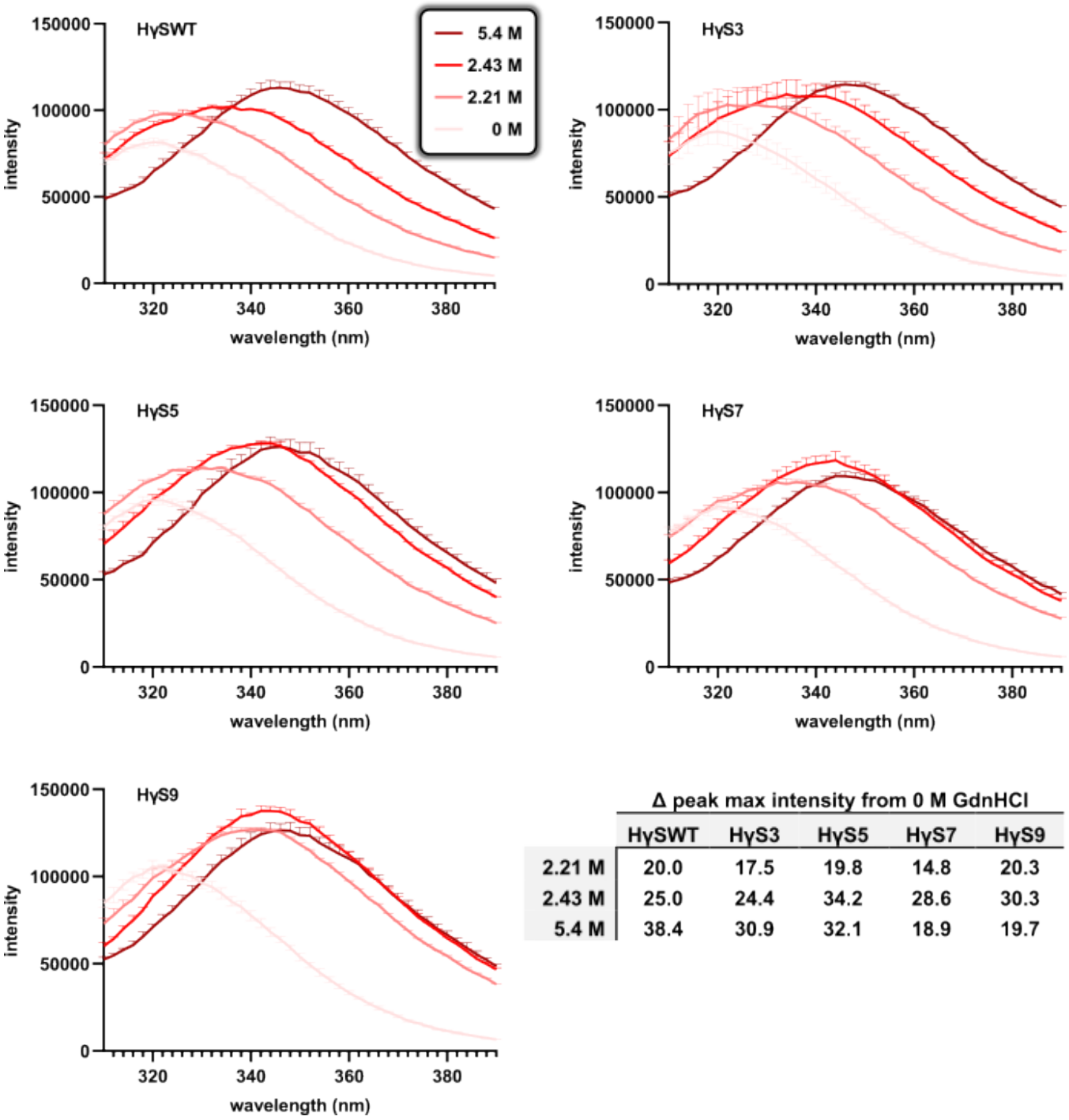

	Δ peak max intensity from 0 M GdnHCl				
	HγSWT	HγS3	HγS5	HγS7	HγS9
2.21 M	20.0	17.5	19.8	14.8	20.3
2.43 M	25.0	24.4	34.2	28.6	30.3
5.4 M	38.4	30.9	32.1	18.9	19.7

Figure B.4: Fluorescence spectra of HγSWT and each deamidation variant at 0, 2.21, 2.43, and 5.4 M guanidinium chloride (GdnHCl). λ_{ex}=280 was used to excite tryptophan fluorescence which was measured from 310-390 nm

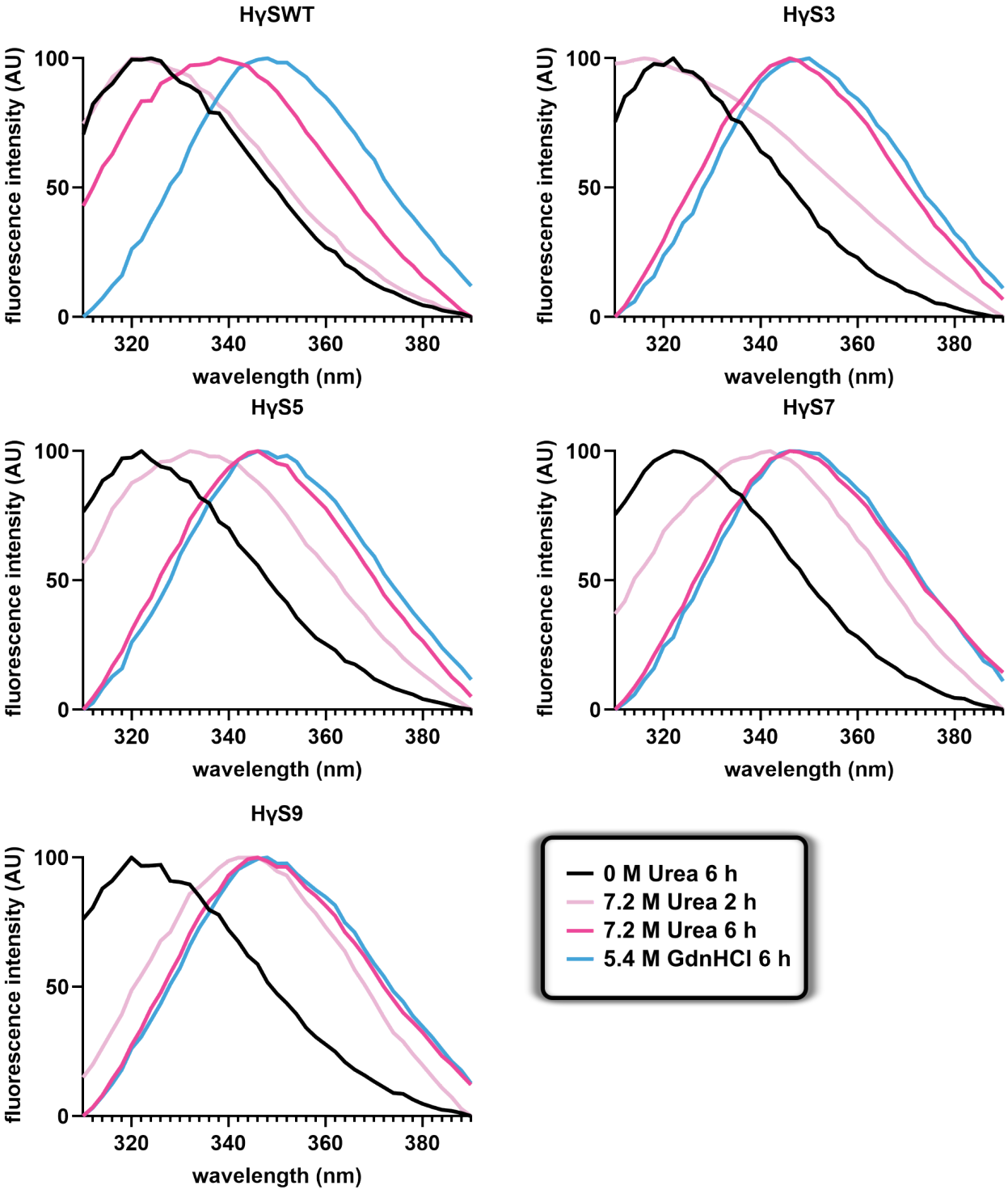

Figure B.5: Normalized fluorescence spectra of HγSWT and each deamidation variant at 0 M (black) and 7.2 M (pink) urea. Fluorescence spectra at 7.2 M urea is shown at both 2 h (light pink) and 6 h (dark pink). Fluorescence spectra of each variant is shown at 5.4 M guanidinium chloride (blue) after 1 h. λ_{ex}=280 was used to excite tryptophan fluorescence which was measured from 310-390 nm.